EXPERIMENTAL VALIDATION AND EVALUATION OF UNCERTAINTY IN THE MONTE CARLO MODELING OF ELECTRON IRRADIATION OF COMPLEX OBJECTS

A Dissertation

by

TERESA ELIZABETH TUTT

Submitted to the Office of Graduate Studies of
Texas A&M University
in partial fulfillment of the requirements for the degree of

DOCTOR OF PHILOSOPHY

December 2007

Major Subject: Nuclear Engineering

EXPERIMENTAL VALIDATION AND EVALUATION OF UNCERTAINTY IN THE MONTE CARLO MODELING OF ELECTRON IRRADIATION OF COMPLEX OBJECTS

A Dissertation

by

TERESA ELIZABETH TUTT

Submitted to the Office of Graduate Studies of
Texas A&M University
in partial fulfillment of the requirements for the degree of

DOCTOR OF PHILOSOPHY

Approved by:

Chair of Committee,	Leslie A. Braby
Committee Members,	John Ford
	John W. Poston, Sr.
	James T. White
Head of Department,	John W. Poston, Sr.

December 2007

Major Subject: Nuclear Engineering

ABSTRACT

Experimental Validation and Evaluation of Uncertainty in the Monte Carlo Modeling of Electron Irradiation of Complex Objects. (December 2007)

Teresa Elizabeth Tutt, B.S., Rensselaer Polytechnic Institute;

M.S., Massachusetts Institute of Technology

Chair of Advisory Committee: Dr. Leslie A. Braby

Monte Carlo method is an invaluable tool in the field of radiation protection, used to calculate shielding effectiveness, as well as dose for medical applications. With few exceptions, most of the objects currently simulated have been homogeneous materials that vary in density by a factor of 3 or less. In the irradiation of very heterogeneous objects, particularly layered or leafy food items, one will encounter air pockets within the bundle as a matter of course. These pockets will cause variations in density of up to three orders of magnitude. Air pockets in a tissue equivalent phantom were found to produce “hot spots” in the dose distribution, and introduced significant deviations between the calculated and measured distribution of dose to the phantom. To date, very little published work had been done in the area of Monte-Carlo simulation of objects of such disparate density. Before Monte Carlo methods can be used successfully in this regime, further code development and experimental validation will be necessary, of which this work is just a beginning. Phantoms were made of corrugated low-Z material similar in electron density to plant based material. These phantoms incorporated air gaps of comparable size to those found in the leafy objects of interest. Dimensions were chosen to bracket electron ranges in the material of the

objects modeled. Monte Carlo analysis will provide a reasonable qualitative picture of the dose distribution, but such a picture is not yet sufficiently accurate in a quantitative sense. Air gaps within the plant material produced large discrepancies between calculation and measurement. Smaller air gaps were observed to produce greater discrepancy between calculation and measurement.

DEDICATION

Dedicated to the loving memory of my sister Julie,

who always believed that I could do it.

ACKNOWLEDGEMENTS

I would like to thank the members of my doctoral committee: Dr. Leslie A. Braby, Dr. John Ford, Dr. John W. Poston Sr., and Dr. James White; as well as the students of Nuclear Engineering courses 604, 613, 615, and 673.

In addition, I would like to thank the following individuals at M.D. Anderson Cancer Center: Dr. Uwe Titt, Dr. Oleg Vassiliev, Dr. Isaac Rosen, and Karl Prado.

Finally I would like to thank Dr. Jongsoon Kim in Agricultural Engineering.

This work was partially funded by US Department of Agriculture IFSRI-CSREES: 2002-03935

TABLE OF CONTENTS

Page

CHAPTER Page

LIST OF FIGURES

FIGURE Page

FIGURE Page

FIGURE Page

FIGURE Page

FIGURE Page

FIGURE Page

FIGURE Page

LIST OF TABLES

CHAPTER I

INTRODUCTION

With recent outbreaks of bacterial diseases such as *Escherichia Coli* (E. Coli), as well as the threat of biological terrorism, there has been a renewed interest in the irradiation of consumable products. These products may include, but are not limited to, the following.

Food items such as:

- Leafy vegetables: spinach, scallions, cilantro, parsley, etc.
- Outer layers of fruit: skins, rinds, etc.
- Meat

Other plant based materials such as cotton and paper products are also under consideration for irradiation.

There is strong interest in irradiating food objects with moderate energy electrons ranging from 1 to 3 MeV. These electrons can produce doses in the kilogray (kGy) range at the surface while sparing the material inside. There is interest in using these same electrons to irradiate thin leafy vegetables as well.

As with any irradiation procedure, it is vital that the dose from irradiation be high enough to kill the unwanted pathogens, but not so high as to degrade the quality of the material being irradiated. Lettuce, for example, requires a very precise level of

---

This dissertation follows the style of *Radiation Research.*

irradiation. The dose necessary to kill unwanted pathogens is 90% of the dose that will effectively destroy it, turning it into a black mush (*1*). Hot spots in the dose distribution exceeding 10-11% of the target dose will produce blemishes; rendering the lettuce unappetizing at best, and inedible at worst.

There are two methods to determine the dose to an object irradiated by electron-beam: direct measurement or calculation. The latter is typically accomplished using Monte Carlo methods. Measurements and calculations typically agree to within 3%, for simple geometries involving homogeneous media, where densities vary by a factor of 3 at most.

When one encounters the more complex geometry of plant based objects, particularly leafy food items, one will encounter air pockets as a matter of course. These air pockets will produce density variations of up to three orders of magnitude. In this case the non-uniformities, as well as uncertainties in dose, are expected to increase dramatically. While the average doses may remain similar, the difference between maximum and minimum doses within the material will likely increase with increasing target complexity.

With the exception of work by Kim, Moreira, and Castell-Perez.(*2,3*), very few publications exist that describe Monte Carlo work in this regime of density variation. Current studies that do exist involve modeling the food object by way of Computerized Axial Tomography, calculating the dose, and then measuring the actual dose to the irradiated object by dosimetry media placed at locations of interest. Such studies are made from the viewpoint of food science, with primary interest in determining the biological effects of radiological dose on the quality of the object. This study, by contrast,

is made from the viewpoint of physics, and examines the physical effect of the object on the dose distribution, and how structural elements affect the accuracy of dose calculation.

For any irradiation scenario, it is imperative to develop an accurate dosimetry model, in order to understand and control the variation in dose. Due to the inherent uncertainties, experimental validation of any model will be required prior to the routine irradiation of any type of object.

Due to the recent increases in computer speed and capability, it has become generally easier to calculate than to measure the dose. However in food irradiation, the primary dosimetry has been by experiment, due to simple geometries so far encountered. Experimental validation will assist in developing accurate and practical methods of calculation for the more complex geometries that will be encountered in the future.

1.1 Objectives

The goals of this research are twofold:

1. To assess the effect of structural elements on the dose uniformity in heterogeneous materials such as leafy vegetables, etc.

2. To evaluate areas of uncertainty of calculation and measurement in the final result.

To accomplish these goals, it is necessary to understand, among other things:

- Dose vs. depth relationship.
- Effects of scattering.

- Radiation behavior at interfaces between materials of disparate density.

Monte Carlo simulations employ an array of volume elements (voxels), each with a uniform atomic composition and density, to represent the object simulated. With this in mind, there are only two possibilities for the evaluation of dose at each specific voxel in our model of an object: the standard deviations (error bars) for the measurement and the calculation either overlap or they do not. Where the standard deviations *do* overlap, what does this mean about the uncertainty in the true value? Where they *do not* overlap, what is the meaning? Objective two of the study is to develop a method for determining the uncertainty, independent of the values in the data.

This study compared measurement and calculation for complex repeatable geometric objects, irradiated by 1.3-1.5 MeV electrons readily available at the TAMU food irradiation facility. These electrons are also being used in experimental studies of surface pasteurization (*4*).

CHAPTER II

BACKGROUND

In this chapter the factors affecting the actual dose distribution and uniformity of dose are examined, as well as the factors affecting the accuracy of dose calculations and measurements.

2.1 Repeatable Geometry for Dose Calculation and Measurement

To provide a meaningful comparison between calculation and measurement, a repeatable geometry structure must be devised. It should be easily modeled by calculation, and re-used for many measurements. This structure, referred to as a *phantom*, is created from materials similar in density and composition to the irradiated material of interest. It also approximates geometric conditions which occur in the material, which is useful for examining factors affecting dose uniformity.

2.2 Factors Determining Dose Distribution and Uniformity

2.2.1 Attenuation and Buildup

As electrons pass through a medium they undergo elastic scattering collisions and will lose energy with each collision. Due to their low mass relative to the target atoms, a significant fraction of them are scattered. Electrons backscattered near the surface may escape the medium entirely, no longer contributing to the dose. Deeper into the medium however, more of the backscattered electrons are absorbed in the media and contribute to the dose. The result is a dose of a specific value, at the point of entry (the entrance dose). The dose rises with depth (due to buildup of the secondary electrons, backscatter, and

increasing stopping power as the electron loses energy), reaches a maximum, and then decreases (due to straggling), as illustrated in FIGURE 2.1.

The dose produced by electrons is directly proportional to the mass stopping power, which is the energy stopping power, divided by the density:

$$D_a = \Phi\left[\frac{1}{\rho_a}\left(\frac{dT}{dx}\right)_c\right] = \Phi\left[\left(\frac{dT}{\rho dx}\right)_{c,a}\right]_T \tag{2.1}$$

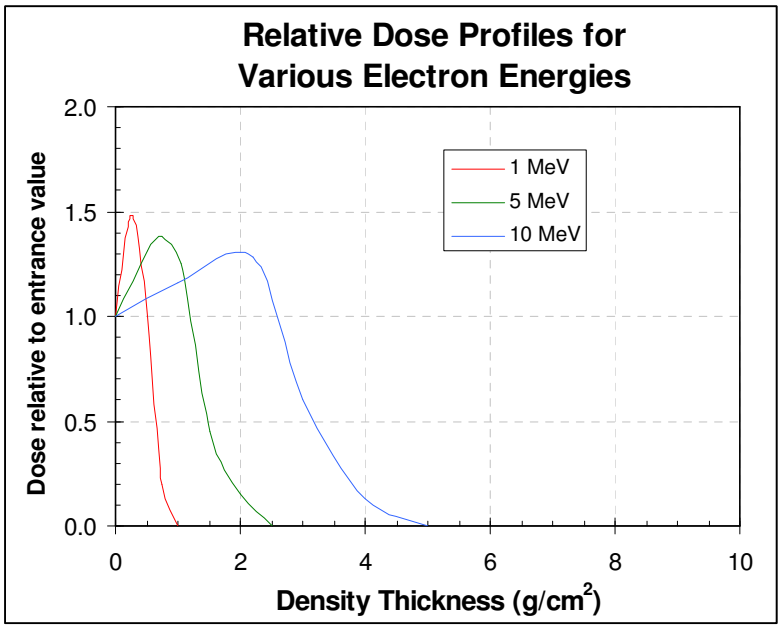

FIGURE 2.1. Dose vs. depth relationship for various electron energies (estimated broad beam data for water, after Attix). (5)

The mass stopping power for electrons is a complex relationship, derived by starting with the Bethe soft collision formula:

$$\left(\frac{dT}{\rho dx}\right)_c = \frac{2\pi\rho_e r_0^2 (m_e c^2) z^2}{\beta^2}\left[\ln\left(\frac{2(m_e c^2)\beta^2 H}{I^2(1-\beta^2)}\right) - \beta^2\right] \tag{2.2}$$

where ρ_e is the electron density per gram of the stopping medium, r_0 is the classic Bohr electron radius, z is the number of charge units of the incident particle (z = 1 for electrons), H is energy boundary between hard and soft collisions, I is the mean excitation potential of the target atom, and β is the relativistic parameter v/c.

This is combined with a hard collision term, $F^-(\tau)$:

$$F^-(\tau) = 1 - \beta^2 + \frac{\tau^2/8 - (2\tau - 1)\ln 2}{(\tau + 1)} \tag{2.3}$$

which is based on Møller electron cross sections, where $\tau = T/m_e c^2$. Letting $k = 2\pi\rho_e r_o^2 (m_e c^2) z^2/\beta^2$, yields.:

$$\left(\frac{dT}{\rho dx}\right)_c = k\left[\ln\left(\frac{\tau(\tau+2)}{2(I/m_e c^2)}\right) - F^-(\tau) - \delta - 2\frac{C}{Z}\right] \tag{2.4}$$

The last two terms, δ and C/Z are correction terms for polarization and shell correction, respectively (*6*).

2.2.2 Beam Geometry

The ratio of beam radius to electron range will have an effect on the dose vs. depth curve. Electrons scattered at oblique angles contribute to dose to the side of the original track and vice versa. Since electrons lose energy with each collision the width of the buildup will decrease with depth. For narrow beams there are fewer contributions to dose from electrons off the axis. For this reason, the dose drops off more rapidly for narrow beams than for broad beams (Figure 2.2)

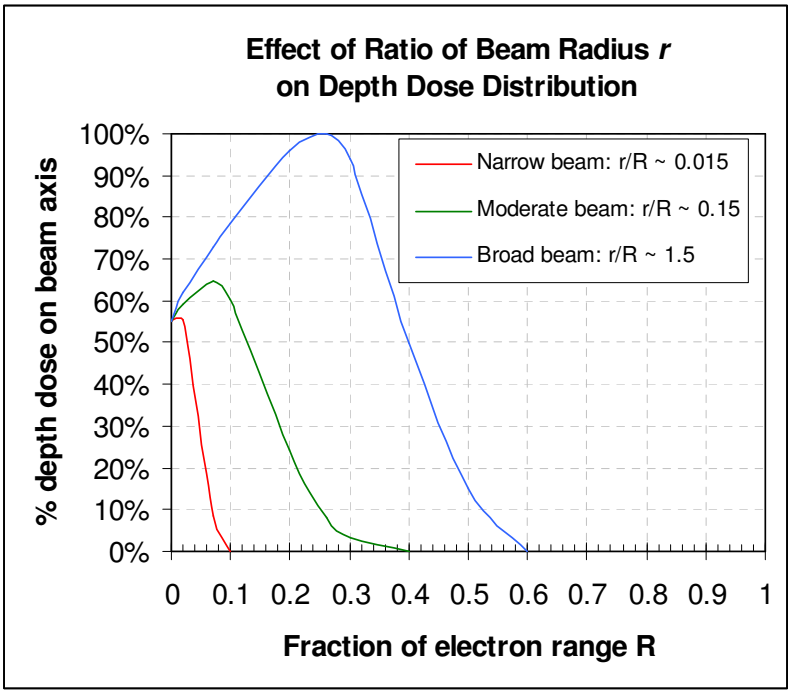

FIGURE 2.2. Effect of ratio of beam radius to electron range (CDSA), for circular beam of 10 MeV electrons incident on polyethylene (estimated from dose calculation, after Attix). (*7*)

2.2.3 Interfaces Between Media of Dissimilar Density

At the interface between two different media, electrons can be backscattered from the second medium back into the first. This can affect the dose vs. depth curve significantly depending upon the similarity in density of the two media, or lack thereof. If the media are of highly disparate density, the effect could be significant depending upon the direction of travel across the interface (Figure 2.3).

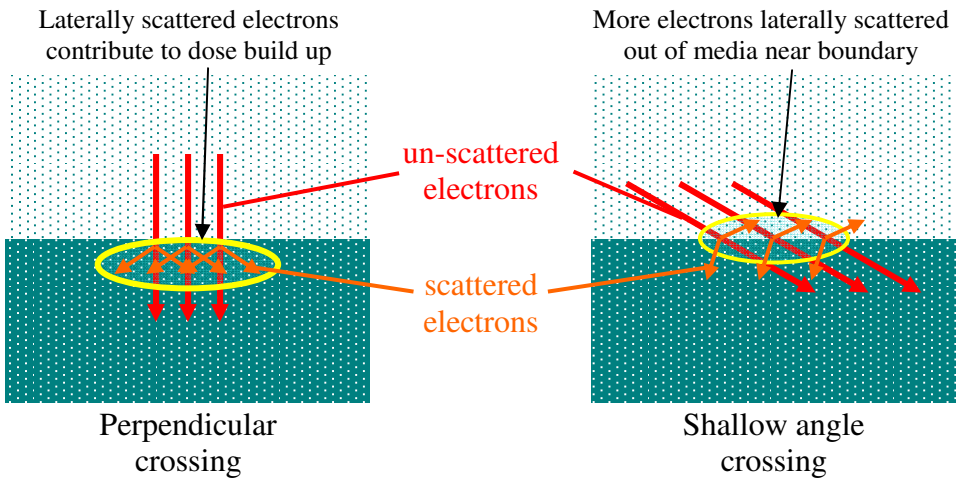

FIGURE 2.3. Effect of direction of electron travel across interfaces.

2.3 Factors Affecting Accuracy of Dose Calculation

The dose to the object is calculated via the Monte Carlo method, using condensed track histories, which are described in detail in Chapter III.

To account for discrepancies between the calculated and the measured dose values, it is necessary to understand the uncertainties in the:

1. Dose calculation (section 2.3)
2. Dose measurement (section 2.4)

2.3.1 Voxel Size and "Coarse Element" Effects

An essential element of Monte-Carlo simulation is to produce an accurate model of the object to be irradiated; in this case, our phantom (described in section 3.2). Ideally, a Computerized Axial Tomography (CAT) scan of the object would be used to the voxel map. However the available scanner provided insufficient resolution for our purposes. The minimum size of the voxel was a cube ~ 2 mm in width. Our smallest phantom

structures were on the order of 0.1 mm. Therefore, it was necessary to construct a voxel map for each phantom geometrically, and enter it into the code by hand.

Actual objects rarely lend themselves to exact geometric representation. The simple object shown in FIGURE 2.4 is not precisely modeled in Cartesian or curvilinear co-ordinates, since it has elements of both.

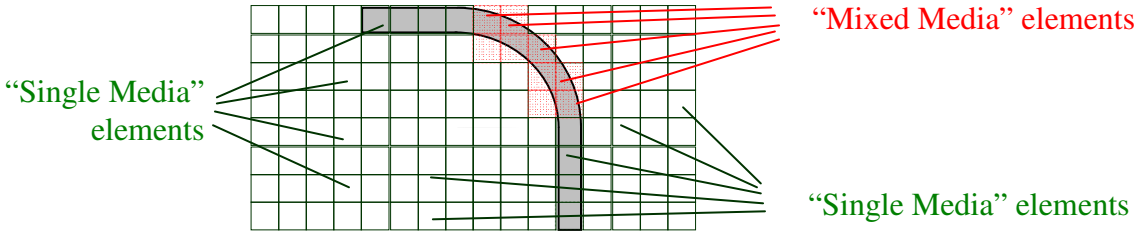

FIGURE 2.4. Two dimensional illustration of coarse element errors in simple structure.

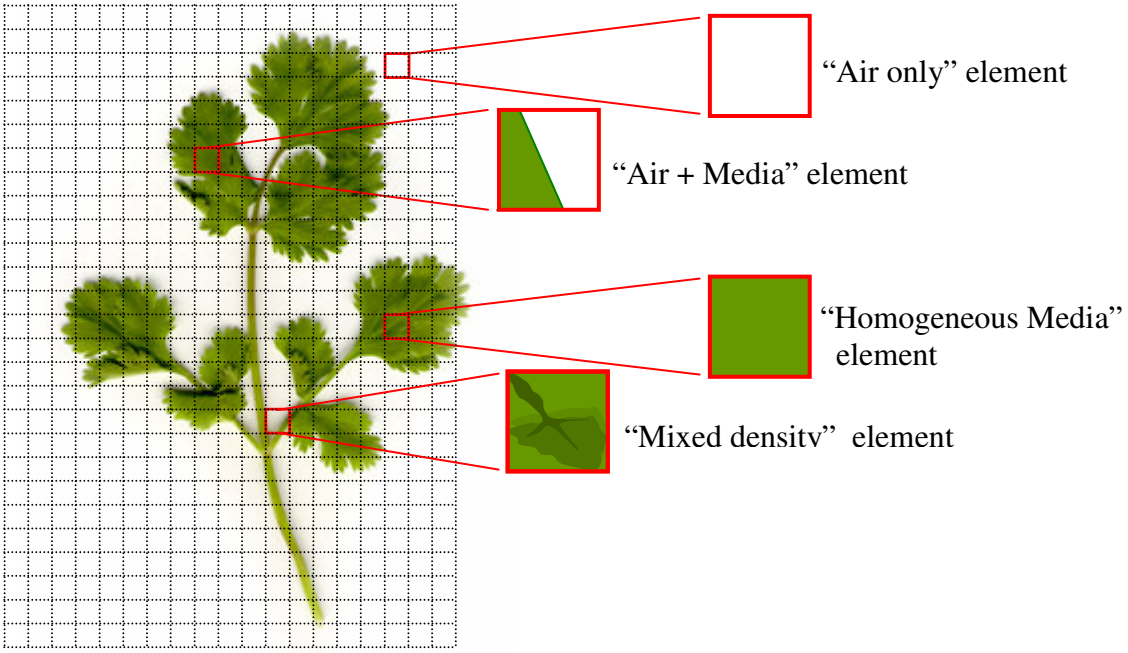

FIGURE 2.5. Two dimensional illustration of coarse element errors in cilantro leaf.

When one progresses to more complex shapes, the problem can be much more severe, as is observed in the example of a cilantro leaf illustrated in Figure 2.5. When the voxel does not precisely match the material, it is no longer an accurate representation of the material in its location.

Ideally each voxel would represent a specific homogeneous medium, either a specific organic material, or the intervening air. However this will not be the case at every voxel site. Voxel elements are in the form of a cube ($dx * dy * dz$)(*8*). So, regardless of how small one makes the voxel element, there will always be certain fraction of voxels which will be a blend of 2 or more materials. The density will be an average of the density of the two media. This can cause errors in the direction of electron travel. A fast electron can undergo multiple small angle coherent scattering events with the net result of the electron following a curving path. The radius of curvature will depend on the number of collisions along its path, which is directly proportional to the electron density of the medium. As once can observe from Figure 2.6, the error occurs in both the electron location and direction into the next voxel. As the electron passes through successive voxels, these errors will accumulate and alter the macroscopic dose distribution.

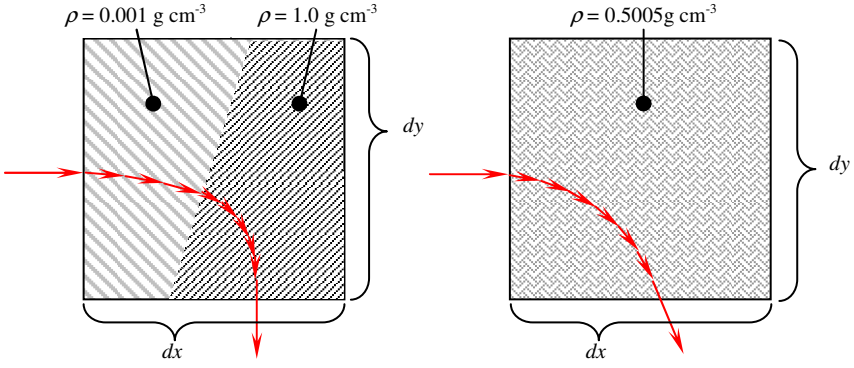

FIGURE 2.6. Coarse element error produced by averaging the densities in voxel.

2.3.2 Condensed Track Histories

A typical fast electron (~10 MeV) may undergo10^5-10^6 collisions with the surrounding atoms of the target. This can make detailed Monte-Carlo simulations impractical if not impossible when many electron histories are required. In the interest of optimizing computing time, most Monte Carlo calculations involving electrons utilize a *condensed history* approach. As the name suggests, a large number of interactions are "condensed" into a single step (*9*).

The reasoning behind this approach is that electrons will undergo very little change in energy or direction during a single interaction, and therefore combining many interactions into a single step is justified (*10*). There are three main parameters for the condensed step: S_{max}, the "step size" (*vt,* or *velocity * time)*, which is the maximum path length traveled per step; ESTEPE, the maximum fractional continuous energy loss per electron per step; and E_{cut}, the cutoff energy below which electrons are treated as continuously slowing down particles, with no further steps. Of these three parameters, S_{max} has the largest effect on the accuracy of calculation, while E_{cut} has a smallest effect (*11*). The larger the step size, the faster the computing time. The trade-off is that there is a greater probability for errors when the step size is larger, as there are fewer interactions modeled in the history. The result of these errors can result in artifacts in the dose distribution. The deviation from the actual path can become significant when the step size exceeds the linear dimension of the voxel. A major effect of a large S_{max} is electrons appearing to "channel" along the interior or boundaries of a homogeneous region of the irradiated object. (Figures 2.7 and 2.8).

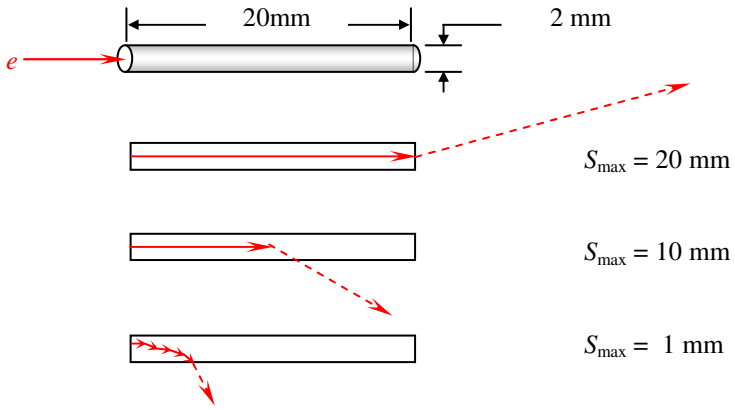

FIGURE 2.7. Electron step-size artifact for 20 mm cylinder surrounded by vacuum (rescaled approximation, after Bielajew) (*12*).

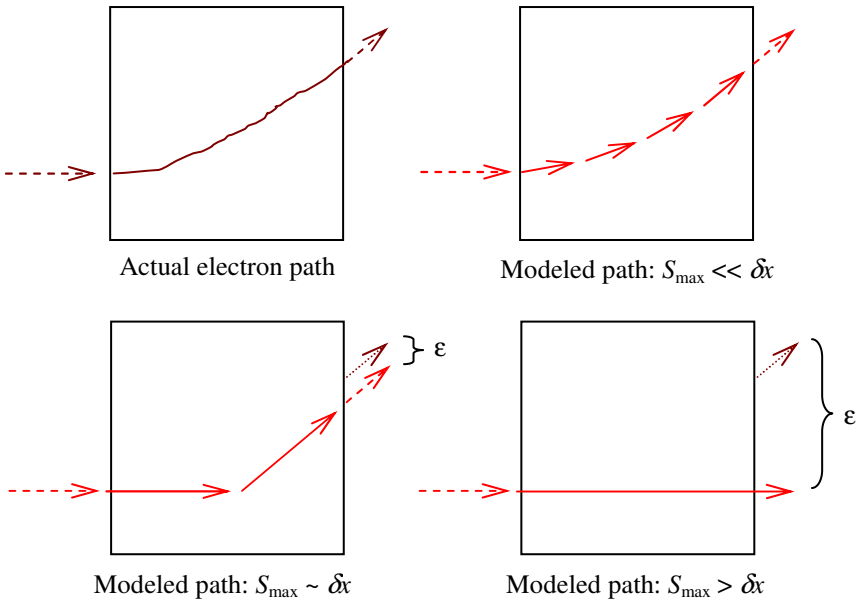

FIGURE 2.8. Electron step-size artifact for voxel cube.

The phantom was designed with these types of calculation errors in mind, as well as creating the types of geometry that would be encountered in the actual irradiated material. The specific parameters and rationale for their selection are described in the next chapter.

2.4 Factors Affecting Accuracy of Dose Measurement

2.4.1 Post Exposure Changes in Dosimetry Media

Since layered and leafy objects were being investigated, it was decided to use media in the form of a thin sheet to measure the dose. Thermo Luminescent Dosimetry (TLD) material, Methyl Yellow impregnated paraffin, and Alanine were unsuitable for use in this manner, due to their thermal and mechanical properties. The primary dosimetry media selected for this research was a radiochromic film with trade name GAFChromic HD810. Radiochromic film is transparent in its unirradiated state, and becomes less transparent when radiological dose is absorbed by it. This reduction in transparency is known as *optical density*, or *O.D*, which is a logarithm of the measurement of the absorption of light by the film:

$$O.D. = \log\left(\frac{\text{Intensity of Incident Light}}{\text{Intensity of Transmitted Light}}\right) \tag{2.5}$$

HD810 is a high dose rate medium, which responds linearly with dose, from zero to 250 Gy. The primary optical density growth occurs within the first 24 hours of exposure. Since relative dose measurement is the objective, it is important that the results not be skewed by differences in times between exposure and reading. By 30 hours post exposure, the density growth curve has become mostly flat, and less sensitive to error (Figure 2.9). For this reason, all films are read as closely to 48 hours post exposure as possible.

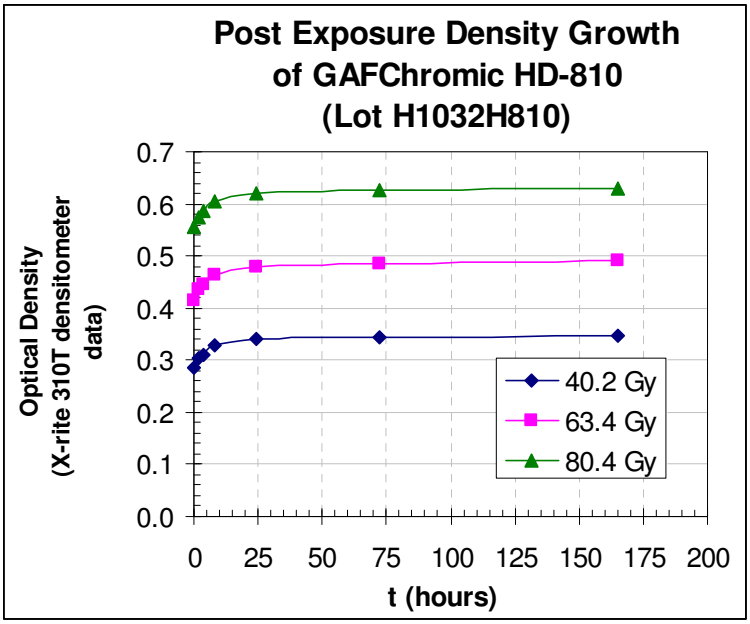

FIGURE 2.9. Post-exposure optical density growth as a function of time. (*13*)

2.4.2 White Light Sensitivity of Dosimetry Media

While sensitivity to white light is low, it is not zero (Figure 2.10). When not in use, the film is stored in a light-blocking container. While every effort is made to keep the film out of light prior to irradiation, it is unavoidable that a certain amount of film will undergo exposure during pre-processing. Sections of unexposed film were read periodically to determine if any drift in the optical density value of the unexposed film has occurred. If necessary, recalibration of the remaining film was performed.

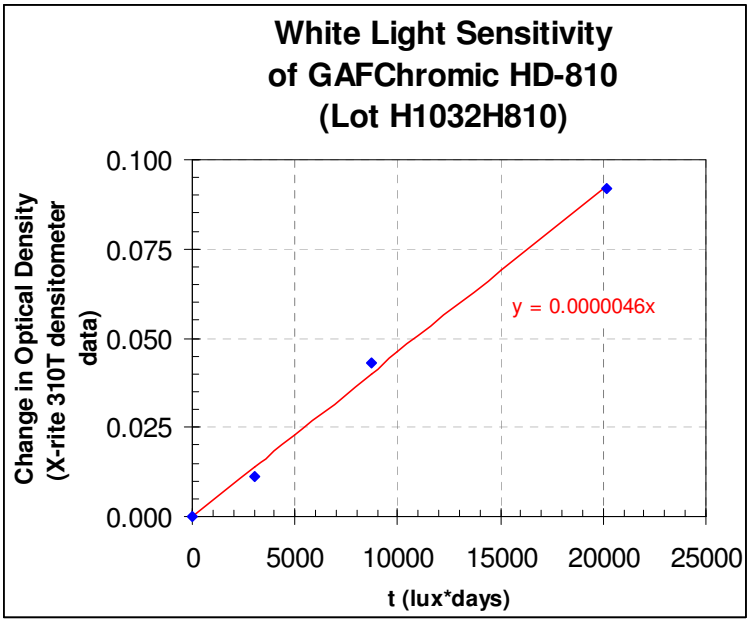

FIGURE 2.10. White light sensitivity of radiochromic film. (*14*)

2.4.3 Orientation of Dosimetry Media

The radiochromic film is not symmetric from front to back. The active layer of the film is surrounded by clear polyester layers of unequal thickness (Figure 2.11). In theory, the most sensitive "side" of the film will depend upon electron energy. In practice, there is no observable difference in response of flat film with respect to the direction of irradiation so long as the media are the same on both sides of the film. The orientation of the film *can* have an observable effect when there is a large difference in the density of the material contacting either side of the film. This is useful in exploring the effects of boundaries separating such dissimilar materials.

There is also a potential for error if the film is folded. The active layer will be stretched or compressed, depending upon the direction it is folded. There is a measurable increase in sensitivity where the media is compressed as opposed to when it is stretched.

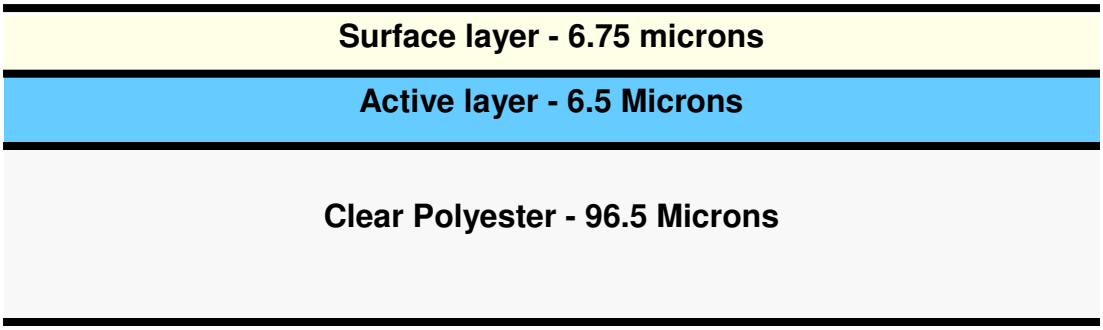

FIGURE 2.11. Configuration of radiochromic film (not to scale). (*15*)

2.4.4 Reading of Dosimetry Media

The Radiochromic film is read via a flatbed scanner, and the intensity value of the scan is converted to optical density (*16*). The optical density is a linear function of the dose (see Appendix A). The intensity may vary from scan to scan. For a single scan comprising of a group of several pixels, this is simply the standard deviation of the group. However for isodose and dose vs. depth plots, data points are often represented by single pixels. Therefore it was necessary to establish a standard deviation for each scanned pixel. A set of pixels was needed with the same absorbed dose. To accomplish this, a single pixel was scanned multiple times to obtain the set.

Figure 2.12 shows the standard deviation of the set in red light for an early calibration run. Twenty scans were made of films exposed to 60.4, 111.3, and 222.5 Gy, respectively. The value of a specific pixel was recorded, and the same pixel was recorded on successive scans. The scanned values were grouped in "sets" of 10, 15 or 20, taken at random from the entire groups. The *x* axis is the number of pixels in a specific set (10, 15, or 20) and the *y* axis is the standard deviation of the set.

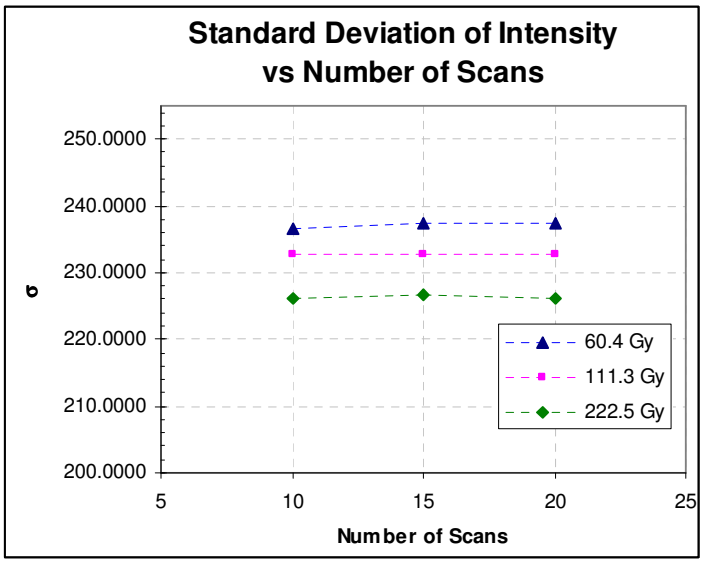

FIGURE 2.12. Standard deviation of film intensity value.

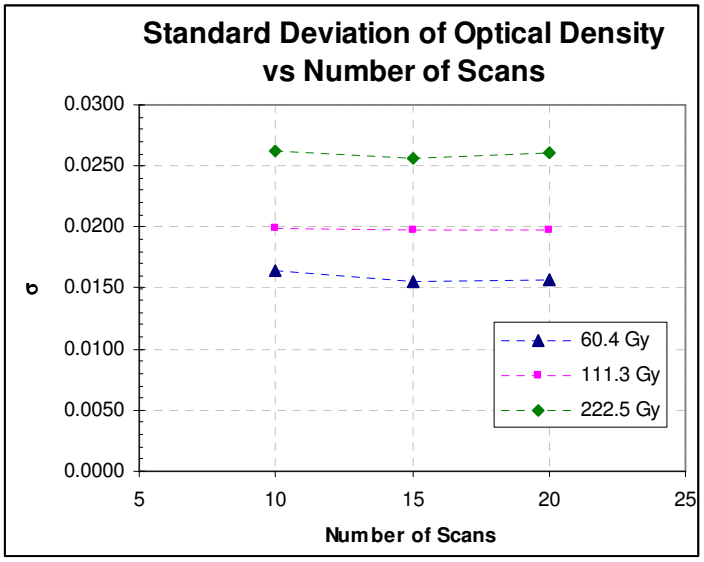

FIGURE 2.13. Standard deviation of optical density

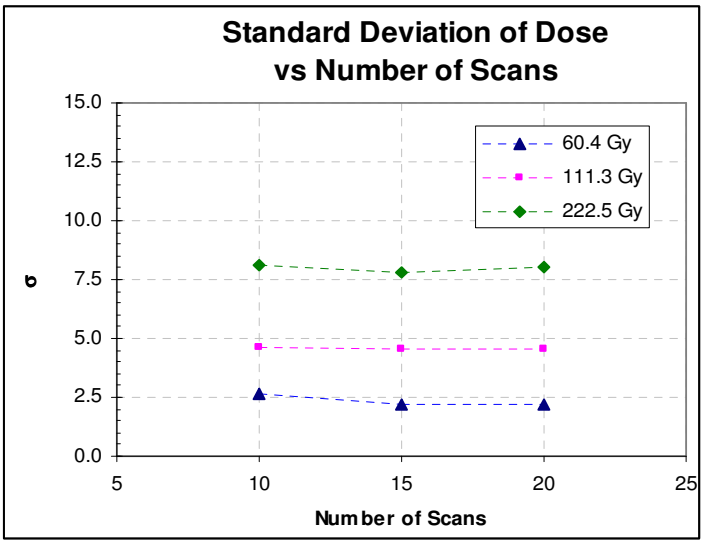

FIGURE 2.14. Standard deviation of Dose

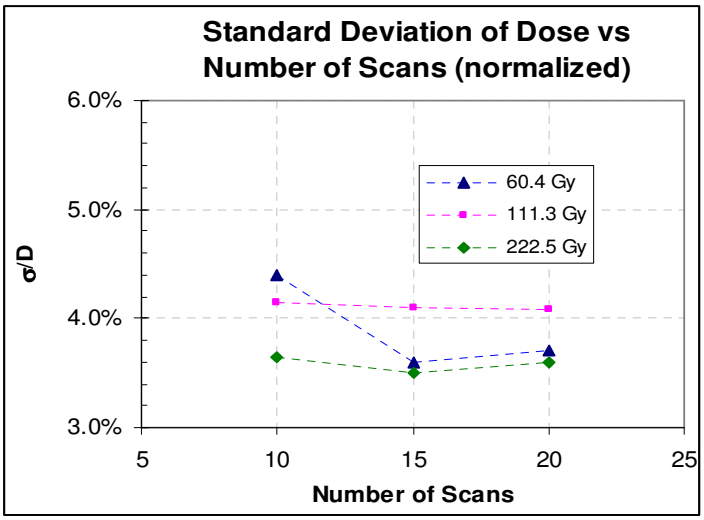

FIGURE 2.15. Normalized standard deviation of Dose.

The standard deviation in intensity was converted to that of optical density (Figure 2.13) and then to that of dose (Figure 2.14). From this, it becomes apparent that the standard deviation σ varies linearly with dose. These values were then normalized by dividing σ by dose D. These values level off at ~ 4% as the number of scans increase beyond 5-10 (Figure 2.15). Therefore, for this study, the error bars for measured values are chosen to be 4% of the measured dose.

CHAPTER III

MATERIALS AND METHODS

3.1 Outline of Research

To adequately assess dose uniformity, and to evaluate the uncertainty of the Monte-Carlo calculations relative to measurement; the research was divided into roughly eight steps as follows:

1. Develop a suitable phantom that represents conditions in the food items and allows measurement of areas of interest. Further, it should provide a strong challenge to the Monte Carlo code as to identify potential areas of error
2. Irradiate the phantom and measure the dose distribution where possible.
3. Produce a voxel map of the phantom for Monte Carlo calculations.
4. Calculate the dose to the phantom, and plot the dose distributions in the same areas where the dose is measured.
5. Compare calculated and measured dose distributions in the corresponding location.
6. Develop appropriate descriptions of differences between measured and calculated dose as relative to the topological features of the phantom.
7. From these descriptions, develop predictions of the errors and non-uniformity of dose that are applicable to other target configurations.
8. Finally, test these predictions on additional phantom configurations.

The first four steps are outlined in detail in this chapter. Step 5 is discussed in Chapter IV. Steps 6 through 8 are discussed in the final chapter.

3.2 Development of Phantom

3.2.1 Configuration and Arrangement of Irradiated Media

Of primary interest is the irradiation of leafy vegetables such as spinach, lettuce parsley cilantro etc. It was necessary to develop a suitable phantom to represent these items. At first glance, it would seem that the obvious approach would be to cut pieces of film into the shape of the leaves and pile them into an arrangement similar to that of the actual food items packed for shipping (Figure 3.1). The drawback to this approach lies in its lack of repeatability for calculation. Since the leaves will be packed in a random arrangement, (or semi-random if they are on stalks as is the case of parsley or cilantro), it is virtually impossible to duplicate this in a hand generated voxel map. Even if it were possible to CT scan the target immediately after irradiation, some shifting of the arrangement between irradiation and scanning is inevitable.

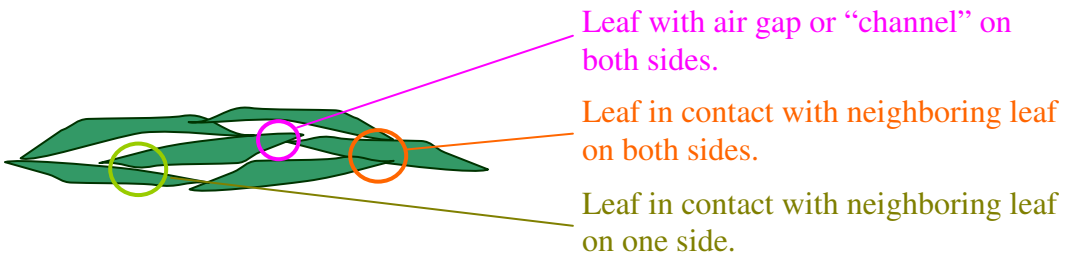

FIGURE 3.1. Arrangement of vegetable leaves, showing conditions of interest.

3.2.2 Layered Corrugated Styrene Phantom

As a compromise, several phantom designs were constructed of a complex, but quantifiable and repeatable structure. To model the effects of contact with neighboring leaves and the air gaps between them, the phantom consists of tiles of corrugated plastic with the radiochromic film sandwiched between them. The film represents the leaf being

irradiated while the tiles represent the effect of other leaves surrounding it. Styrene was chosen for the tile material, due to its simlar chemical composition and density to the film substrate. It had the additional advantage of being readily available in preformed shapes adaptable to the phantom.

The main parameter of the corrugated phantom geometry is the "pitch", defined here as the distance between the start of one fold and the next. The electron beam is incident on the z-axis, in the direction parallel to the "valleys" formed by the folds (Figure 3.2). Another important parameter is the fold "depth", which is the distance between the styrene and the film in the middle of the fold. The folds in the styrene will form channels through which the electrons can travel. An area of interest is the "entrance region": the segment of the channel from the incident surface to a depth approximately equal to the depth of the fold. Another topic of interest is the dose in the solid at a distance of several times the range of the electrons in film. This is significant because electrons are able to travel down the adjacent channel of air and then scatter into the film.

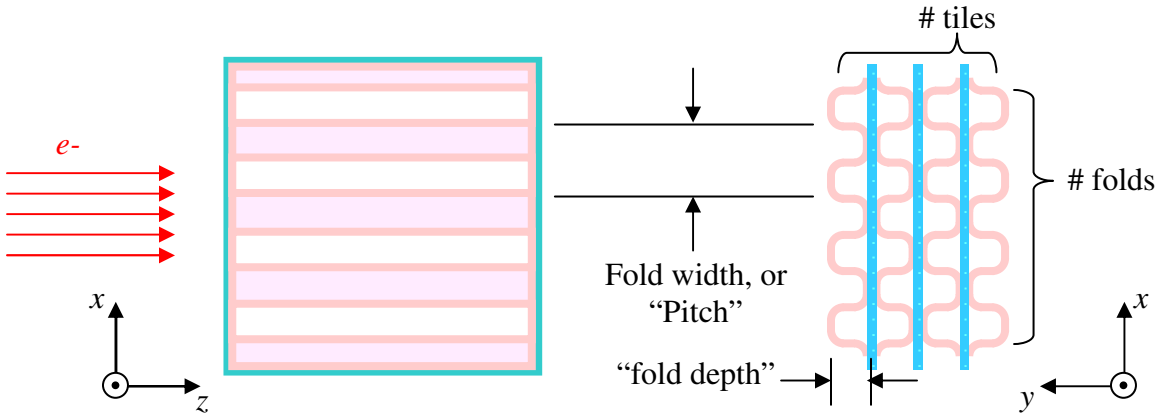

FIGURE 3.2. Flat film supported between corrugated styrene, with coordinate system.

An alternative arrangement is to have the folds offset, so that the plastic is in contact with the film on one side and not on the other (Figure 3.3). This arrangement is useful in

investigating the effects of asymmetry in the film, as the active layer is closer to one surface of the film than the other.

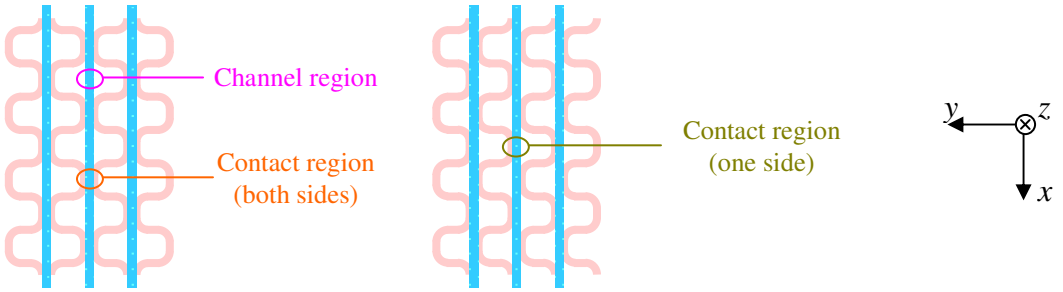

FIGURE 3.3. Folds "facing" (left) vs. offset "right".

The phantom relates specifically to the food object as follows (Figure 3.4). The so-called "channel" regions represent regions where there is an air gap on either side of the leaf or both sides. The contact region is representative of regions where one leaf of material comes into contact with another, either on one side or both. The channels are of particular interest as they represent air gaps that are certain to occur in this type of irradiation

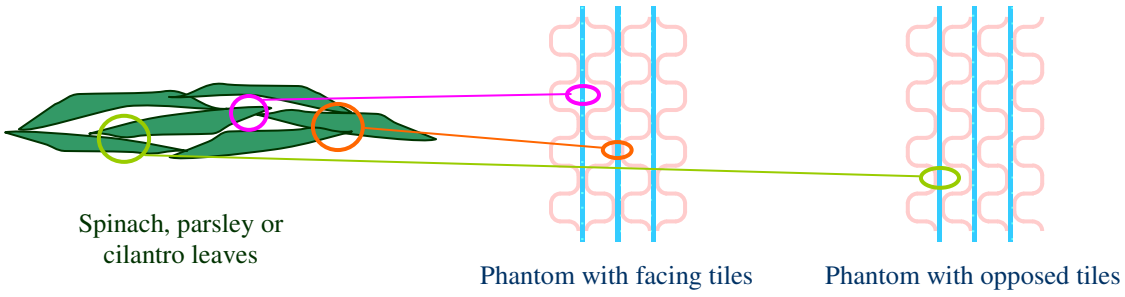

FIGURE 3.4. Relationship of phantom elements to food items (film represents leaf).

There are three different fold widths used in the phantom: 1 mm, 2 mm and 5.5 mm. These values were chosen to bracket the range of 1.5 MeV electrons in styrene

(0.1-0.5 cm). The target is 19.1 mm (0.75 in) in *x*, 6mm (0.235 in.) in *y*, and 19.1mm (0.75 in.) in *z*. Table 3.1 shows the parameters of the three phantom designs.

TABLE 3.1
Initial design parameters of the three phantoms used in the study

	Parameter			
Phantom	Pitch	Folds/cm	# folds	# tiles
A	1.0 mm	10.0	19.1	6
B	2.0 mm	5.0	9.5	4
C	5.5 mm	1.8	3.5	2

3.3 Irradiation and Measurement of Dose Distribution in Phantom

The electron beam irradiates the phantom containing the radiochromic film. The film is then removed and scanned. From the scans, one measures the distribution of intensity in the plane of the film (x-z). This intensity is converted to dose, which produces a two dimensional plot of the dose absorbed by the film. This distribution is plotted as a surface in the x-z plane, where the level curves represent areas of equal dose. Therefore this plot is known as an *isodose* plot.

3.3.1 Target Irradiation Geometry

The target is irradiated with incident radiation primarily along the *z*-axis of our coordinate system shown below (Figure 3.5). The beam direction is a vector described by three angles $\langle \theta_x, \theta_y, \theta_z \rangle$. These three angles correspond to the angle of the vector relative to the positive *x*-axis, positive *y*-axis, and negative *z*-axis respectively (*17*).

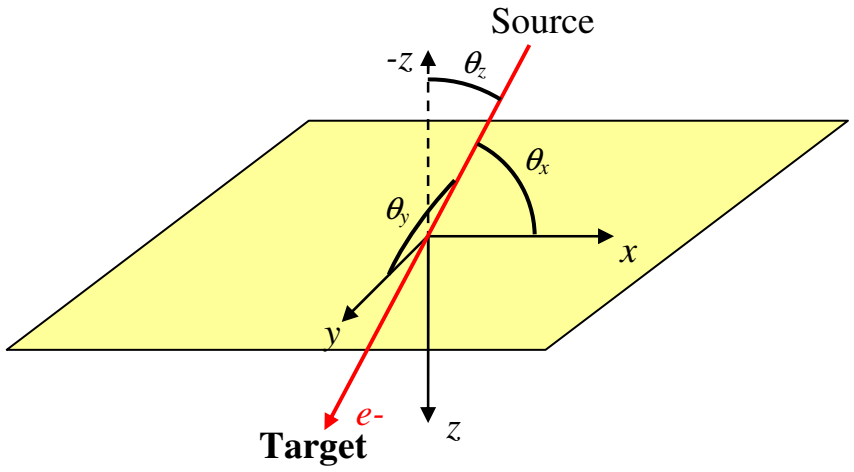

FIGURE 3.5. Beam-target coordinate system, showing directional angles.

The default beam direction is along the z-axis $\langle \pi/2, \pi/2, 0 \rangle$. For the layered, corrugated phantom of section 3.2.2, this defines an irradiation parallel to the direction of the folds in the phantom. This sends the majority of incident electrons directly down the channel formed by the folds (Figure 3.6).

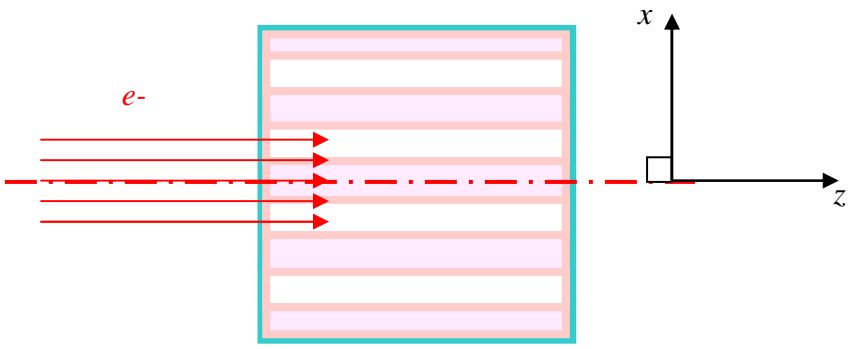

FIGURE 3.6. Default direction for irradiation of layered phantom $\langle \pi/2, \pi/2, 0 \rangle$.

If necessary, the target could be irradiated at different angles relative to the direction of the folds (Figure 3.7), while remaining in the plane of the radiochromic film. For so-called in-plane irradiation, the beam remains orthogonal to the y-axis. Since the sum of

the three directional cosines (cos θ) must equal 1, $\theta_x = \pi/2 - \theta_z$. for in-plane radiation. Therefore the beam direction depends only on θ_z . $\langle \theta_x, \pi/2, \theta_z \rangle = \langle \pi/2 - \theta_z, \pi/2, \theta_z \rangle$

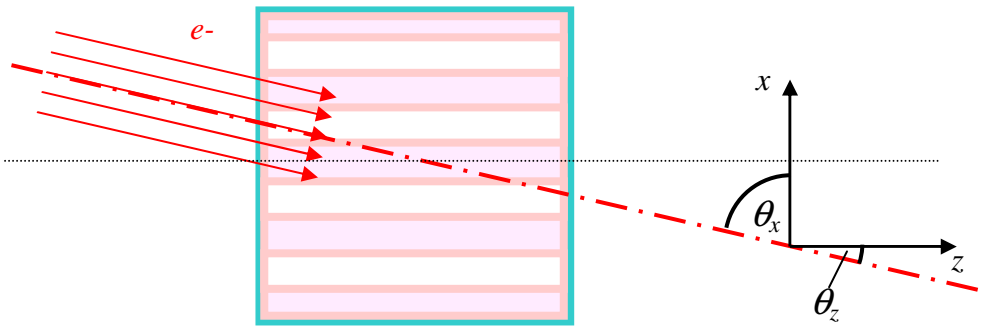

FIGURE 3.7. Angled in-plane (x-z) irradiation $\langle \pi/2 - \theta_z, \pi/2, \theta_z \rangle$.

Additional irradiation could be performed out of the x-z plane if desired. Figures 3.8 and 3.9 show the geometry for orthogonal (y-z plane) and arbitrary out of plane irradiation, respectively

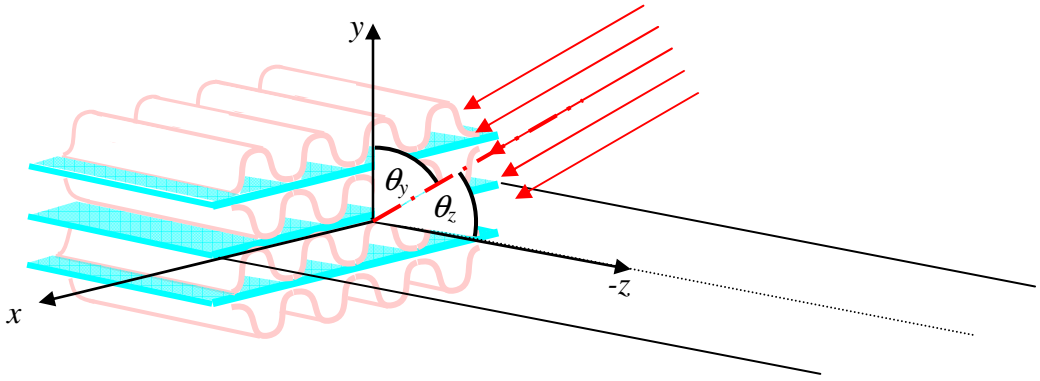

FIGURE 3.8. Orthogonal (y-z) out-of-plane irradiation $\langle \pi/2, \pi/2 - \theta_z, \theta_z \rangle$.

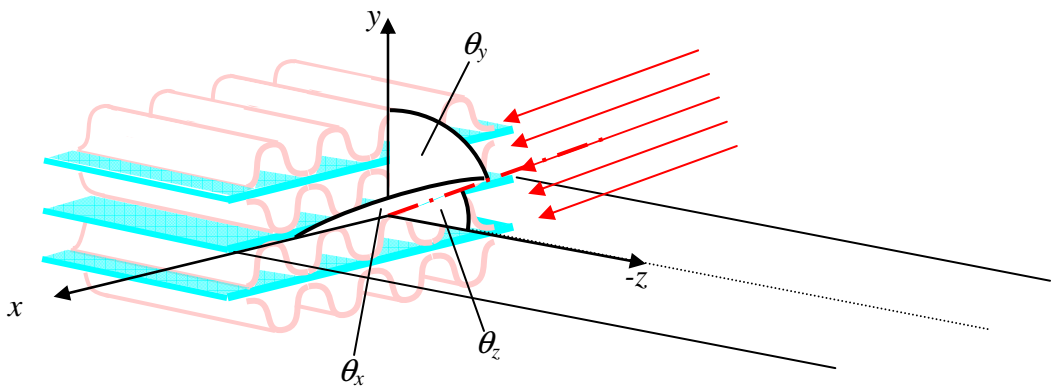

FIGURE 3.9. Arbitrary out-of-plane irradiation $\langle \theta_x, \theta_y, \theta_z \rangle$.

While the above irradiation geometries were possible, not all of them were considered of sufficient interest to investigate. The research focused mainly on irradiation parallel to the channels formed by the corrugation. This direction of irradiation was of primary interest as maximizing the possibility of errors was a major goal, in order to identify potential areas of trouble.

3.4 Development of Voxel Maps for Monte Carlo Dose Calculation

To calculate the dose to the phantom, it is necessary to construct a three-dimensional map of the phantom as close to the actual object as possible. To simplify the specific comparisons between measurement and calculation, the actual phantom and voxel map dimensions were matched as closely as possible.

3.4.1 Voxel Map Geometry

The voxel maps representing the target are based on a cartesian co-ordinate system as shown in Figure 3.10. The voxel dimemsions in each direction (δx, δy, δz) are defined either individually, or in groups. Not all voxels will necessarily be the same size, or even

have the same proportions. This allowed greater flexibility in that voxel size could be tailored to arbitrary target geometries. The voxels were made as small as possible to produce an accurate model without unduly affecting computing time. Voxel sizes were also set as uniformly in size as possible, in order to minimize computing errors due to binning and averaging (as discussed in section 5.2) without unduly affecting target model accuracy.

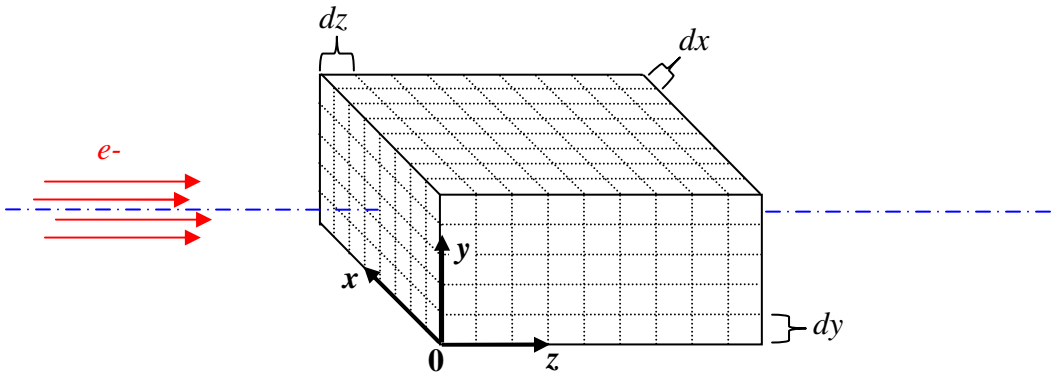

FIGURE 3.10. Voxel map geometry for 3-d phantom.

The media of the target was defined by assigning values for each voxel based on what material is present in the phantom at the corresponding location. Voxel dimensions were chosen to most accurately match the target media, while maintaining as regular a spacing as reasonable.

A sample voxel map is shown in Figure 3.11. It represents a segment of radiochromic film (turquoise) sandwiched between two corrugated sections of styrene (gray), with air filling the intervening spaces. The styrene is 0.5 mm thick, and is folded along the z-axis such that there is 5.5 mm between the start of one section of the fold and the next. In this simplified case there is one section of the fold in each sheet. All voxels are 0.25 mm wide

in the x direction (δx = 0.25 mm). and 0.35 mm long in the z direction (δz = 0.35 mm). The voxels with an index in y equal to 12 represent the sheet of film, and as such are only 0.1 mm high in the y direction (δy = 0.1 mm). All other voxels are 0.25 mm high (δy = 0.25 mm).

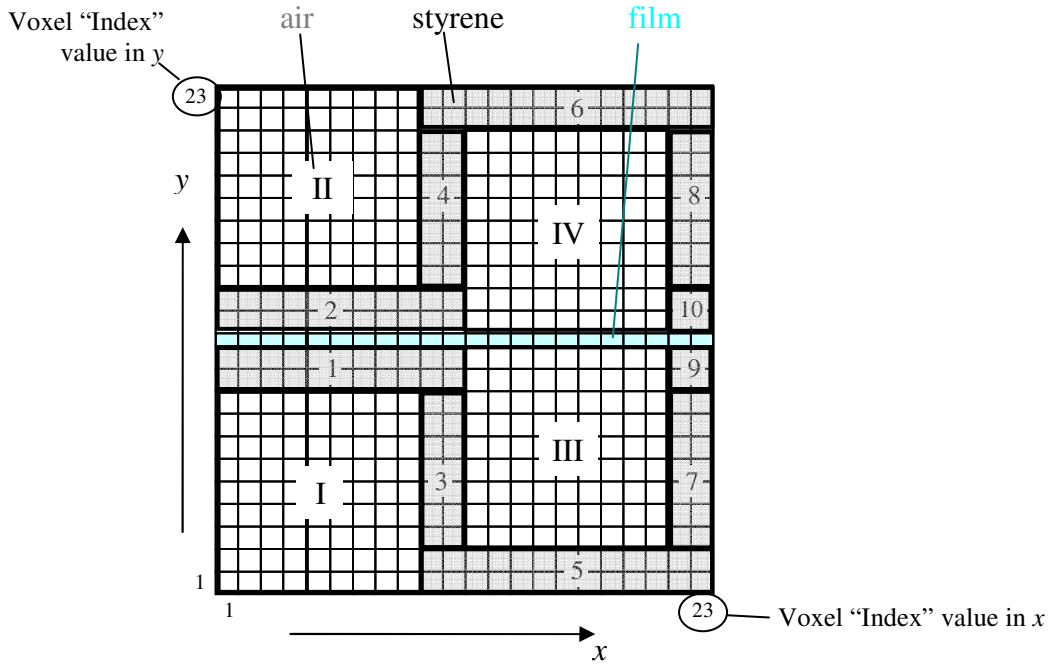

FIGURE 3.11. Sample voxel map, showing segments of film styrene, and air.

As with the dose measurement in section 3.3.1, the default beam is incident is along the z-axis: ⟨π/2, π/2, 0⟩. These parameters are set by the user to match the actual beam irradiation angles.

The voxels are arranged in segments defined by ranges of voxel indices. Table 3.2 shows the assignment of material to each group. Segments labeled 1 through 10 are given an assigned material value of "styrene". All voxels with a y index equal to 12 comprise the segment assigned as "film". Segments labeled with Roman numerals I through IV are assigned as "air"

TABLE 3.2
Indices of voxels defining the sample map of figure 3.9

	Voxel indices (start, end)		
segment	*x*	*y*	*z*
Styrene 1	(01, 11)	(10, 11)	(0, 36)
Styrene 2	(01, 11)	(13, 14)	(0, 36)
Styrene 3	(10, 11)	(03, 09)	(0, 36)
Styrene 4	(10, 11)	(15, 21)	(0, 36)
Styrene 5	(10, 22)	(01, 02)	(0, 36)
Styrene 6	(10, 22)	(22, 23)	(0, 36)
Styrene 7	(21, 22)	(21, 22)	(0, 36)
Styrene 8	(21, 22)	(15, 21)	(0, 36)
Styrene 9	(21, 22)	(10, 11)	(0, 36)
Styrene 10	(21, 22)	(13, 14)	(0, 36)
film	(01, 23)	(12, 12)	(0, 36)
air I	(01, 09)	(01, 09)	(0, 36)
air II	(01, 09)	(15, 23)	(0, 36)
air III	(12, 20)	(03, 11)	(0, 36)
air IV	(12, 20)	(03, 11)	(0, 36)

δx = 0.25mm
δy = 0.25 mm (y=1-11, y=13-22); 0.1 mm (y=12)
δz = 0.5 mm

3.5 EGSnrc Monte-Carlo Calculation of Dose Distribution

The radiation transport and dose distribution in this study is modeled by the EGSnrc (Electron Gamma Showers) Monte Carlo code. This code was chosen for its flexibility and particular suitability in modeling coupled electron/gamma transport and secondary interactions. EGS uses the condensed track history approach described in section 2.3.2.

3.5.1 Major Input Parameters

The three main EGS parameters of interest in this study were:

- SMAX, (Step-size MAXimum): This is the maximum path length distance (*vt* or velocity of particle multiplied by the time between interactions) traveled per electron per step.
- ESTEPE (maximum Energy STEP for Electrons): This is the maximum fractional continuous energy loss that the electron will undergo per step.
- ECUT (Electron CUToff energy): This is the minimum energy at which the electron is modeled. Once the electron energy falls below this value, its history is terminated, and its remaining energy is deposited in that region.

Of these parameters, SMAX was expected to have the most effect on calculation accuracy, while ECUT was expected to have the least (*18*). SMAX has a large effect on calculation time as well. The larger the step size, the faster the computing time. The tradeoff is that there is a greater probability for errors when the step size is larger, as there are fewer interactions modeled in the electron history. The result of these errors can result in artifacts in the dose distribution as illustrated in section 2.3.2. Recommended values of SMAX are ~ 5 cm for low density media such as air, but were on the order of 0.5-1.0 mm for the phantom used in this research.

By contrast, ECUT has a large effect on computing time, but a small effect on calculation accuracy, so it may be set to a relatively high value, on the order of 100 keV. In general ECUT is set to such an energy level at which the electron range is approximately 1/3 of the size of the smallest structure in the phantom.

3.5.2 Constructing the Voxel Map for Phantoms Used in This Study

The film and corrugated tiles comprising the phantom are squares 1.905 cm on a side (Figure 3.12). They are placed in a target holder and bound on either side by acrylic, 0.5842 cm in thickness. (See appendix B for detail.)

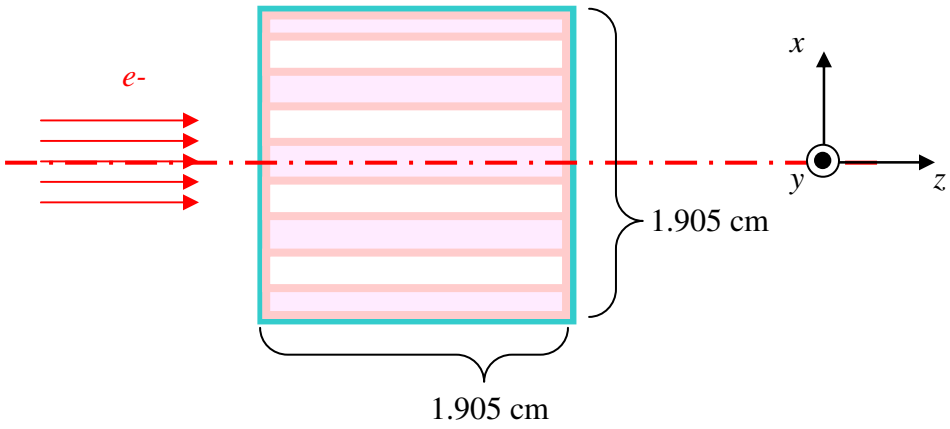

FIGURE 3.12. Dimensions of film and tiles.

The voxel maps were generated by overlaying a 2 dimensional grid over an image of the face of each phantom. The voxels were 0.025 cm wide in *x* and *y* and 0.035 cm in *z*. (The exception was the set if voxels used to model the film, which were .001 cm in y for the active layer and 0.009 cm in *y* for the base layer). All voxels were wider in z, since that the code limits the number of voxel layers to 56 in the *z* direction. This made it possible to span the 1.9 cm width in z in 54 voxels, leaving the first two layers available to model the intervening air between the beamline exit and the target face. Since the corrugations of the styrene tiles were regular, it was possible to generate one "fold" of the corrugation and then repeat it in the *x* and *y* directions. The total pattern was then extended from voxel *z*-indices from 3 to 56. The *z*-indices 0 and 1 were air. A layer of acrylic 0.5842 cm thick on either side of the tiles completed the map.

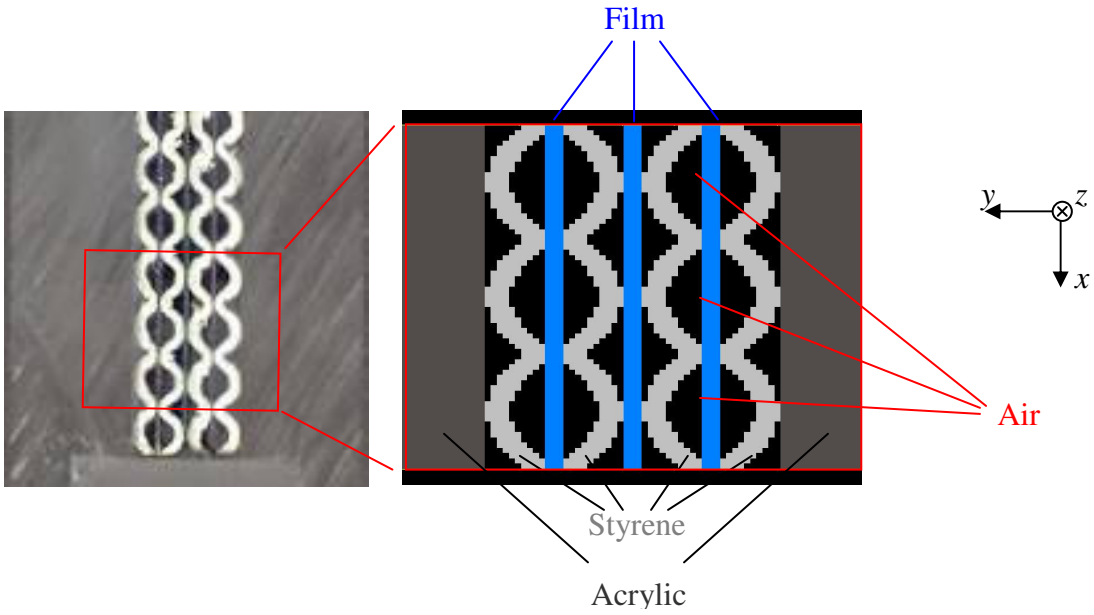

FIGURE 3.13. Face of 2 mm phantom and representative voxel map.

Figure 3.13 shows the 2 mm phantom and the voxel map used in the calculation. Due to the regularity of the dose distribution pattern, it was only necessary to model three folds of the phantom to get an accurate calculation. Simulations of phantoms with more folds were not any more accurate, but they did use considerably more computing time.

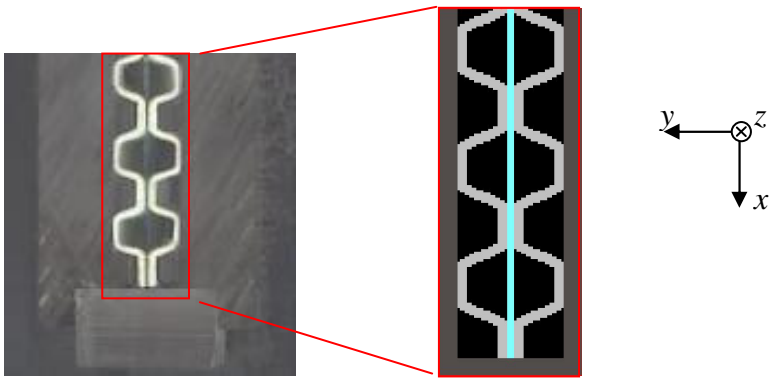

FIGURE 3.14. Face of 5.5 mm phantom and representative voxel map.

Figure 3.14 shows the 5.5 mm phantom and the voxel map used in the calculation. Due to its relative simplicity, it was practical and desirable to model it almost entirely. It should be noted that the tiles are compressed in *y* direction by the target holder. As a result, the corrugations assume a trapezoidal shape. The pitch is increased from 5.5 mm to 6 mm, and the maximum distance from the film to styrene is decreased from 2.25 mm to 2.125 mm.

CHAPTER IV

EXPERIMENTAL RESULTS

4.1 Radiochromic Film Images

The measured dose is determined using radiochromic film located in the plane of interest. It was placed between the layers of corrugated film, as shown in Figures 4.1 and 4.2. In the 2 mm phantom (Figure 4.1) there are four tiles with seven corrugations each. Three films were placed between the tiles. The films were labeled from left to right, with the center film labeled as the "zero" tile. The left and right outer tiles are labeled -1 and +1 respectively. The outer film is closer to the phantom edge in *y* and the polymethylmethacrelate (acrylic) of the target holder than the center film. There are eight "channel" regions in the outer film and seven in the center film.

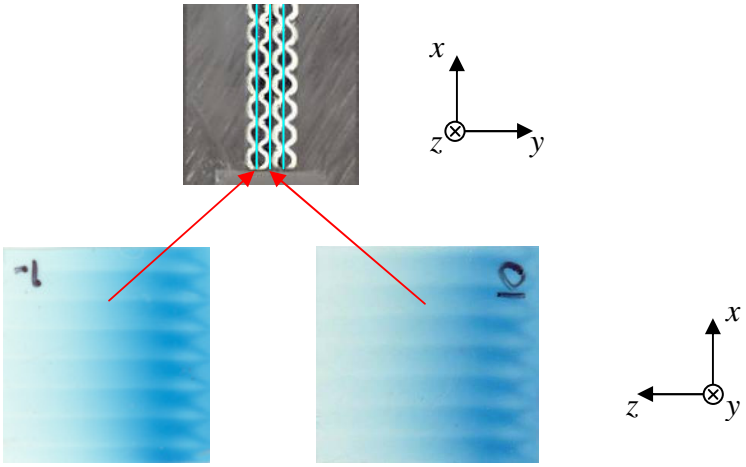

FIGURE 4.1. 2mm phantom and radiochromic film images.

It should be noted that the 2 mm corrugations have a slight cycloid pattern as opposed to a rectangular shape. As a result, the styrene is concave toward the film in the channel region, while it is convex in the center film (Figure 4.2).

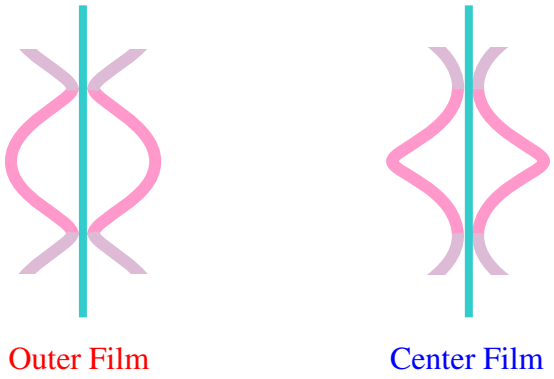

FIGURE 4.2. Channel regions for outer film (left) and center film (right).

In the 5.5 mm phantom (Figure 4.3) there are two tiles with three corrugations each. A single film is placed between the two tiles in this phantom.

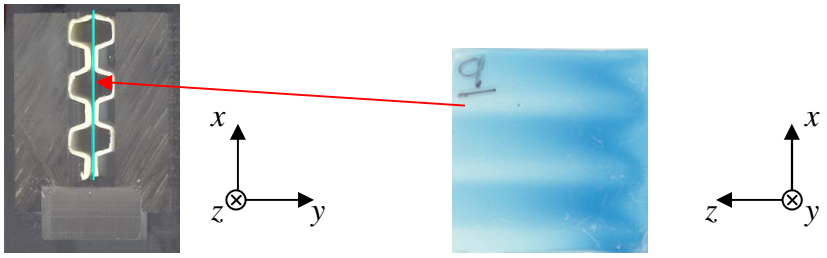

FIGURE 4.3. 5.5 mm phantom and radiochromic film image.

4.2 Comparison of Measured and Calculated Dose

Monte Carlo simulation was performed for each phantom using the EGSnrc Monte Carlo code. In the interest of conserving computing time, the simulations were made using 10^7 histories for 2 mm phantom, and 10^8 histories for 5.5 mm phantom. Also the modeled layer of air between source and target was reduced from 20 cm (actual value) to 4 cm. This was done to allow sufficient dose to the phantom (~ 10^{-10} Gy or 1 MeV/g) and did not noticeably affect the energy dependence of the dose vs. depth curves. (i.e. the

peak of the dose distribution did not shift noticeably in z when the air layer thickness was decreased

In all isodose distributions and comparative plots, the dose value at *z*-indices i and *x*-indices j, or D_{ij}; is expressed relative to the average or mean dose ($\overline{D}$) to the film. $\overline{D}$ is the total dose *D* delivered to the region of interest divided by the number of voxel elements *n* comprising the region.

D is determined by summation of dose values in the region:

$$D = \sum_{i,j}^{n} D_{ij} \tag{4.1}$$

Therefore, $\overline{D}$ is:

$$\overline{D} = D_{mean} = \frac{D}{n} = \frac{1}{n}\sum_{i,j}^{n} D_{ij} \tag{4.2}$$

The *y* axis value of the depth dose plots is the relative dose $d_{i,j}$ for each voxel:

$$d_{ij} = \frac{D_{i,j}}{\overline{D}} \tag{4.3}$$

Thus the dose per voxel, D_{ij}, is expressed as a multiple of $\overline{D}$. This allows meaningful comparisons to be made between the measured and calculated dose values at each corresponding location within the phantom. The region of interest, a subset of the plane of interest, was one complete section of corrugation, taken from the middle of one contact region to the next (Figure 4.4).

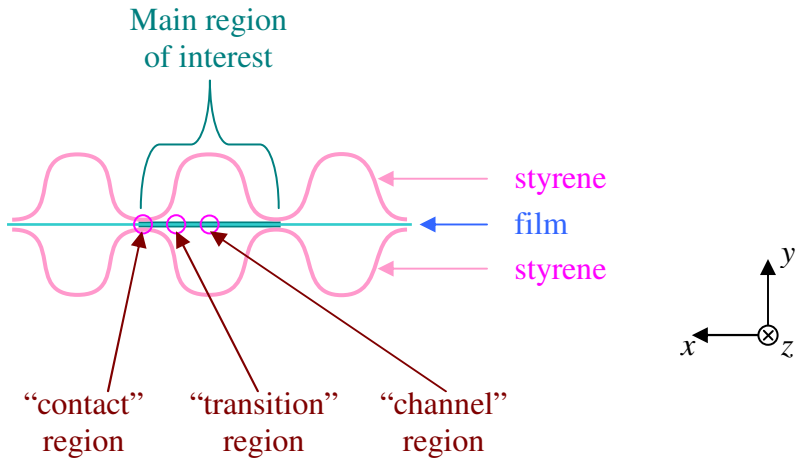

FIGURE 4.4. Defining the regions of interest in the radiochromic film.

Within the region of interest there are three specific sub regions. The first is the channel region, the area along the *z* axis of the film where the styrene is furthest away from the film. The second "contact" region is the film along z where the styrene is in direct contact. The third region is the "transition" region, the boundary between the channel and contact regions.

4.1.1 2 mm Phantom

In the 2 mm phantom, films from two locations were examined: the center film and one of the outer films. The choice of the left (-1) vs. the right (+1) film was purely arbitrary, as the target is symmetrical in the *y* direction (from left to right).

Outer Film

The outer film (-1 position) is shown in Figure 4.5 with the region of interest chosen near the center fold. The region of interest spans the width of a single fold, from the middle of one contact region to the next. D_{ij} was determined by measuring the intensity value (determined by scanning) of the pixel at each location. The intensity value was converted to optical density, and then to dose, by the method described in Appendix A.

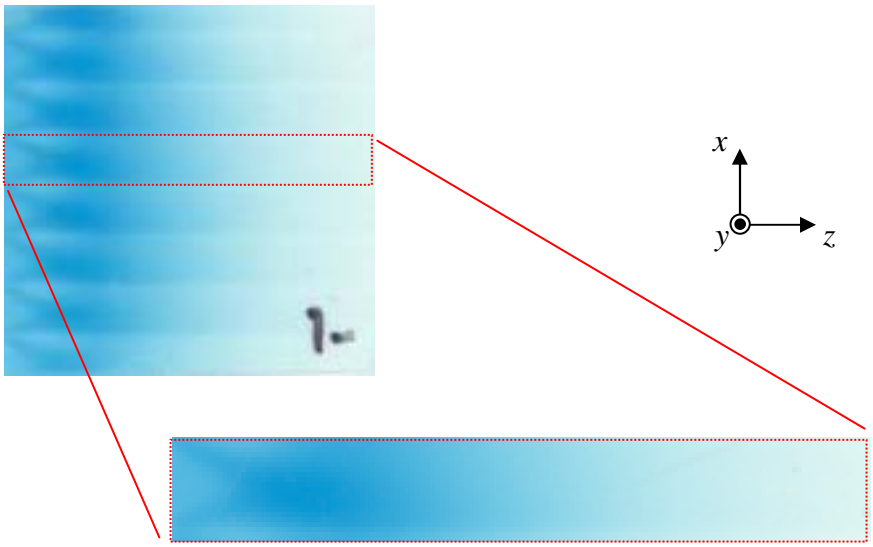

FIGURE 4.5. Outer (-1 position) film image from 2 mm phantom, showing region of interest (highlighted).

The isodose distribution shown in Figure 4.6 is the measured dose to the region of interest shown in figure 4.5. The center of the channel is at x = 0, and the mid-contact regions are at approximately ± 0.1 cm. The transition regions occur at ~ ± 0.08 cm. The region of highest dose appears in the middle of the channel. The maximum dose, D_{max}, occurs along the midline ($x = 0$) at $z = 0.30$ cm.

The calculated isodose distribution is shown in Figure 4.7 The channel, transition and contact regions are the same as that for the measured distribution. The region of high dose is smaller in general for the calculated distribution. D_{max} also occurs in approximately the same place: x = 0.025 cm, z = 0.315 cm.

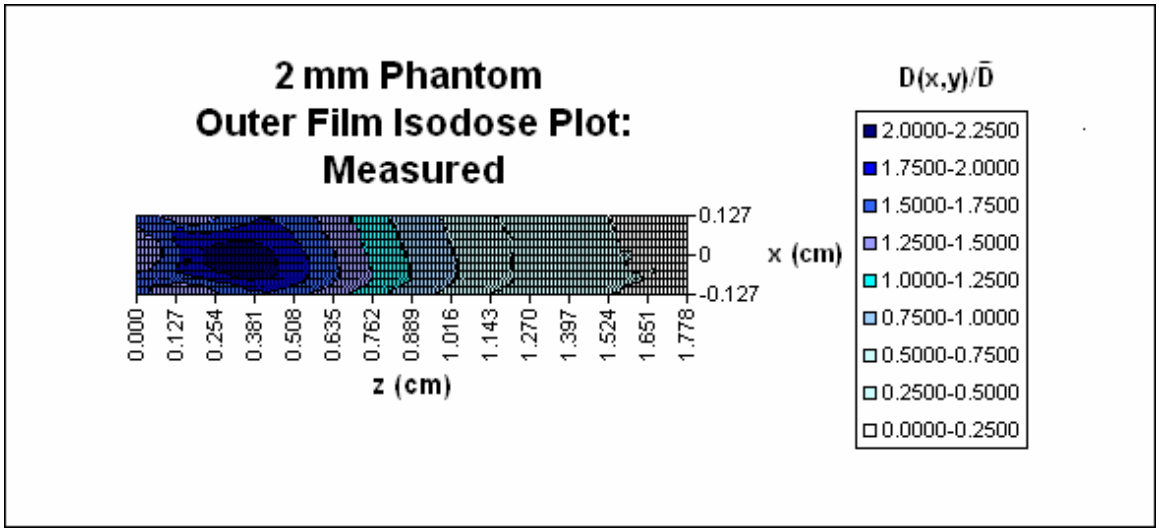

FIGURE 4.6. Measured isodose plot taken from region of interest in Figure 4.1.

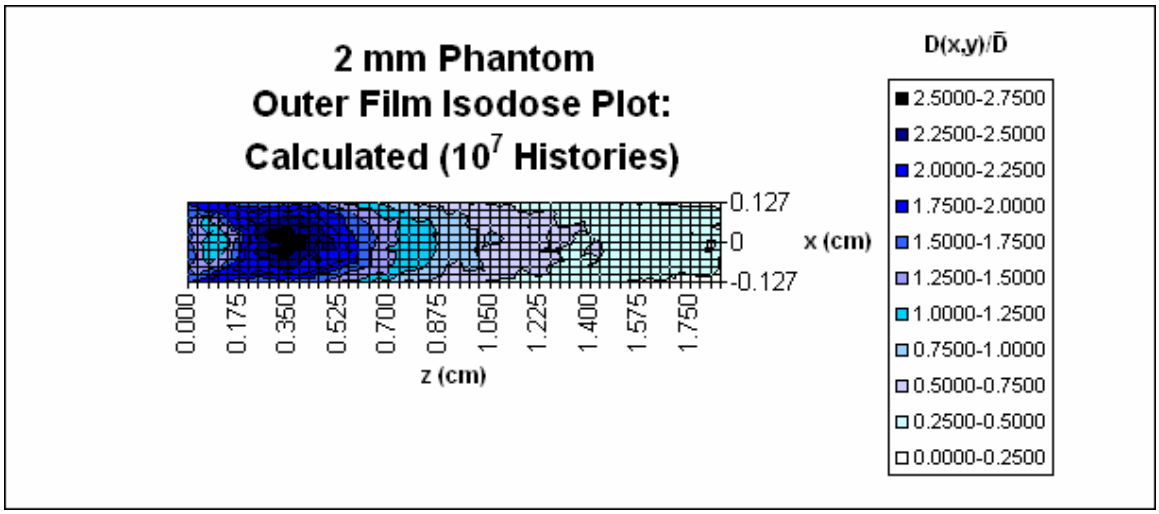

FIGURE 4.7. Calculated isodose plot for region of interest in Figure 4.1.

Figure 4.8 shows the dose vs. depth plot along the midline of the channel. The entrance dose is 1.41 $\overline{D}$ for measured and 1.57 $\overline{D}$ for calculated. The maximum measured dose is 2.11 $\overline{D}$, which occurs in a broad peak from z = 0.2604 cm to z = 0.4005 cm. The maximum calculated dose is much greater, 2.70 $\overline{D}$, and occurs at a narrow peak around z = 0.4025 cm. The peak is narrower partly because the calculated dose initially drops with depth to ~ 1.09 $\overline{D}$ at z = 0.1225 cm, before building up to the maximum, while the measured dose builds up monotonically to the maximum value. The peak is also narrower because the calculated dose decreases more rapidly with depth than does the measured dose.

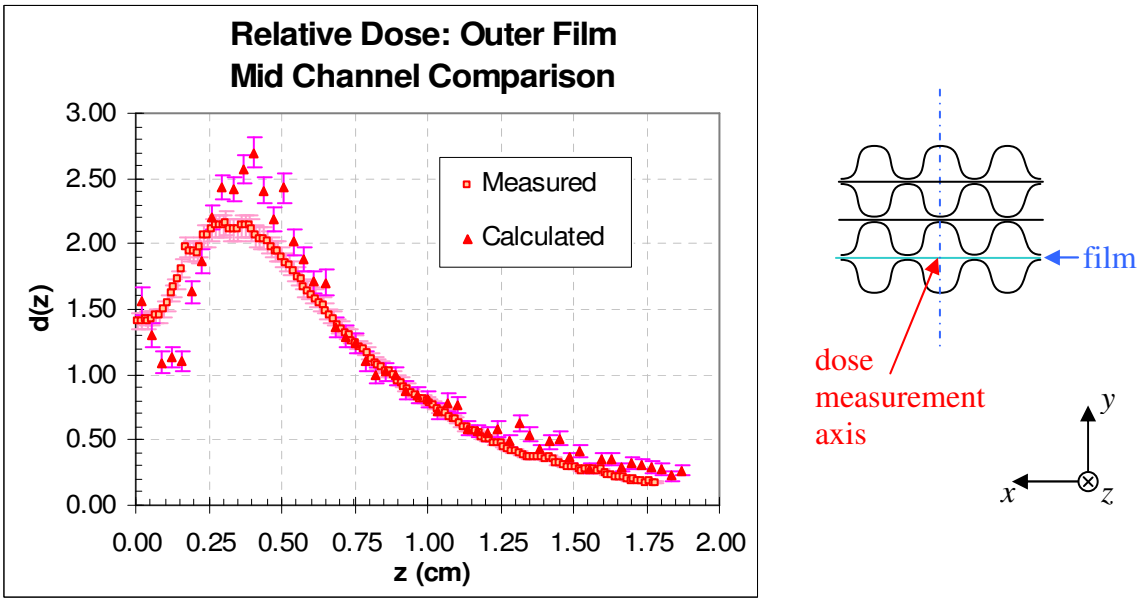

FIGURE 4.8. Dose vs. depth plot along midline of channel.

Figure 4.9 shows the dose vs. depth plot along the borderline between the channel and contact regions. (The "spike" in the measured dose at 0.15 cm is due to a blemish in the film). Trends are similar for both measured and calculated dose inasmuch as they both reach a maximum at approximately the same depth (z = 0.3875 for measured,

z = 0.3675 for calculated). As with the channel region, the calculated dose drops before building up to maximum while the measured dose does not. After reaching maximum, the calculated dose decreases more rapidly with depth than does the measured dose.

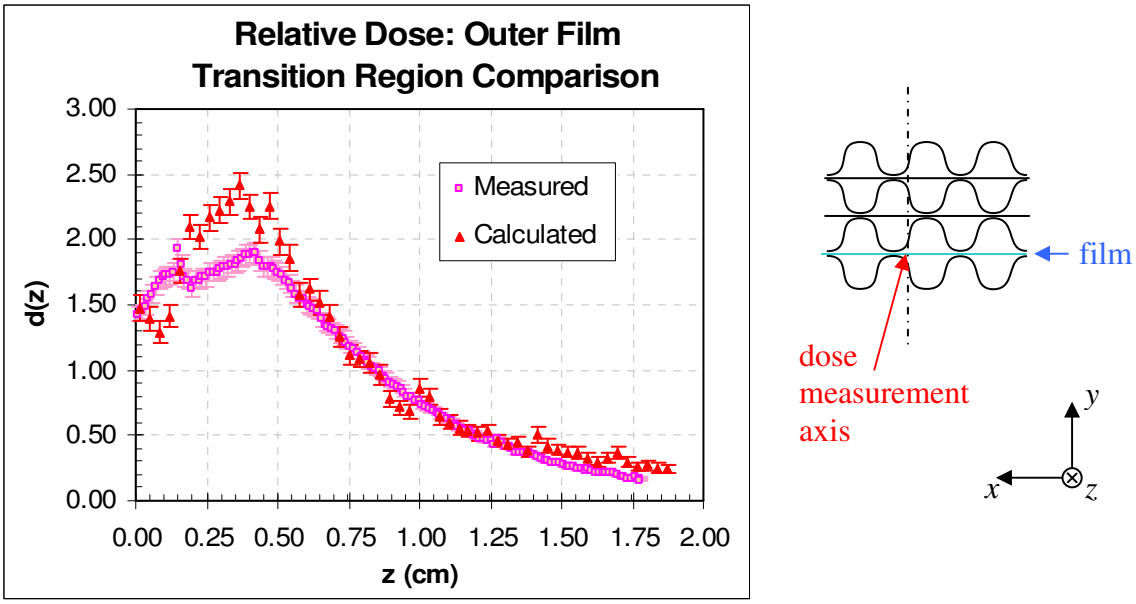

FIGURE 4.9. Dose vs. depth plot along boundary between channel and contact regions.

Figure 4.10 shows the dose vs. depth plot along the midline of the contact region. The measured dose starts at $1.54\,\overline{D}$ at z = 0 cm, drops to ~ $1.33\,\overline{D}$ at z = 0.1817 cm, before increasing to a maximum of $1.17\,\overline{D}$ at z = 0.4382 cm, and then decreases monotonically with depth thereafter.

The calculated dose rises with depth to a maximum very quickly at z = 0.0875 cm, and then decreases thereafter. There is a noticeable "bump" superimposed on the attenuation curve, which coincides with the measured D_{max} at z = 0.4382 cm.

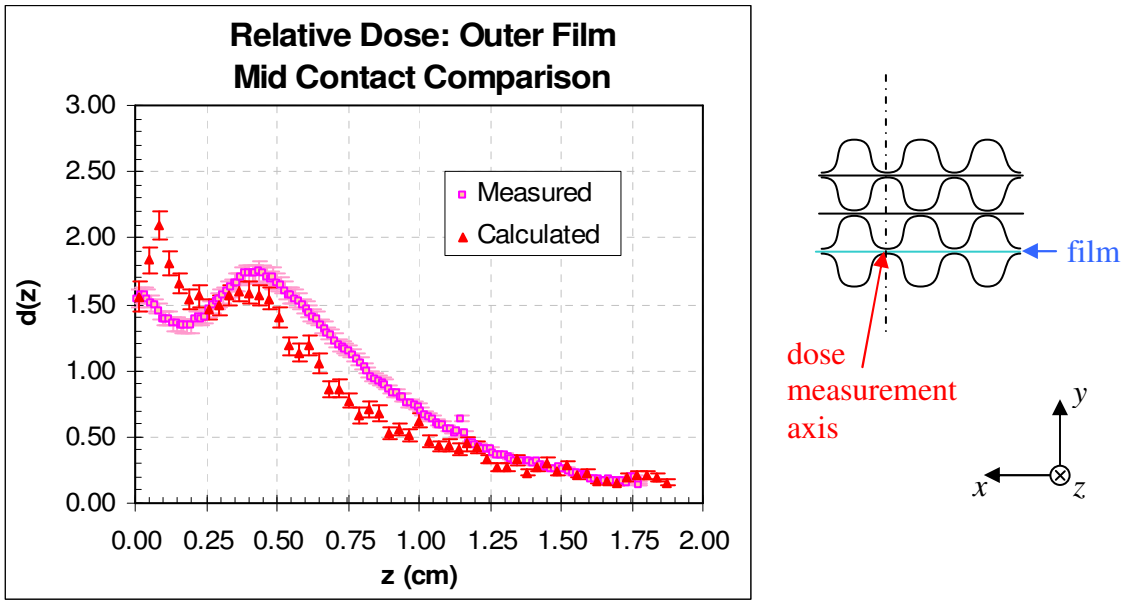

FIGURE 4.10. Dose vs. depth plot along midline of contact region.

Center Film

The center film (-1 position) is shown in Figure 4.11 with the region of interest chosen at the center fold, similar to the outer film in Figure 4.4.

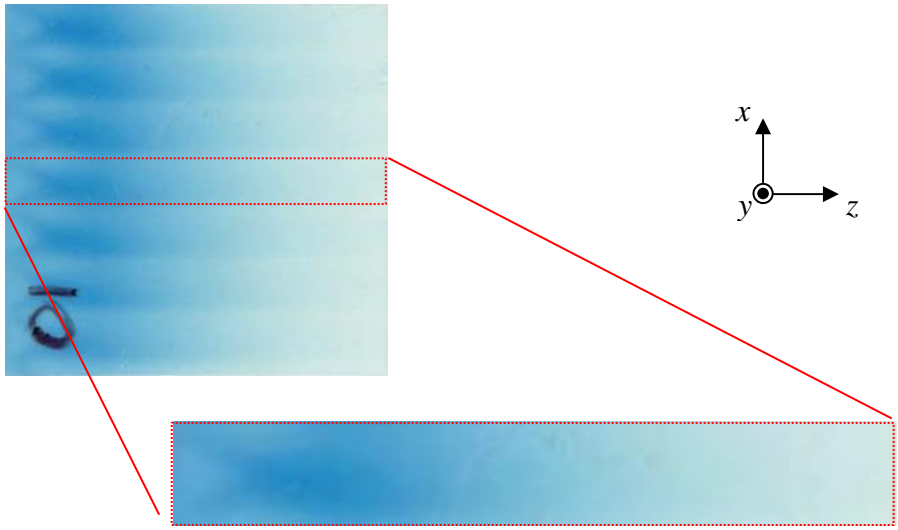

FIGURE 4.11. Center (0 position) film image from 2 mm phantom, showing region of interest (highlighted).

The isodose distribution shown in Figure 4.12 is of the measured dose to the region of interest in figure 4.11. The center of the channel is at $x = 0$ and the mid-contact regions are at approximately ± 0.1 cm. Due to the concavity of the tiles in the contact region, the transition regions occur at ~ ± 0.075 cm as opposed to 0.8 cm in the outer film. The channel region is therefore narrower and the contact region is wider in the center film than in the outer film. This is noticeable in the isodose plot as the region of high dose is narrower for the center film. The maximum dose D_{max} occurs at $x = 0$ cm and z =0.35 cm for the measured distribution.

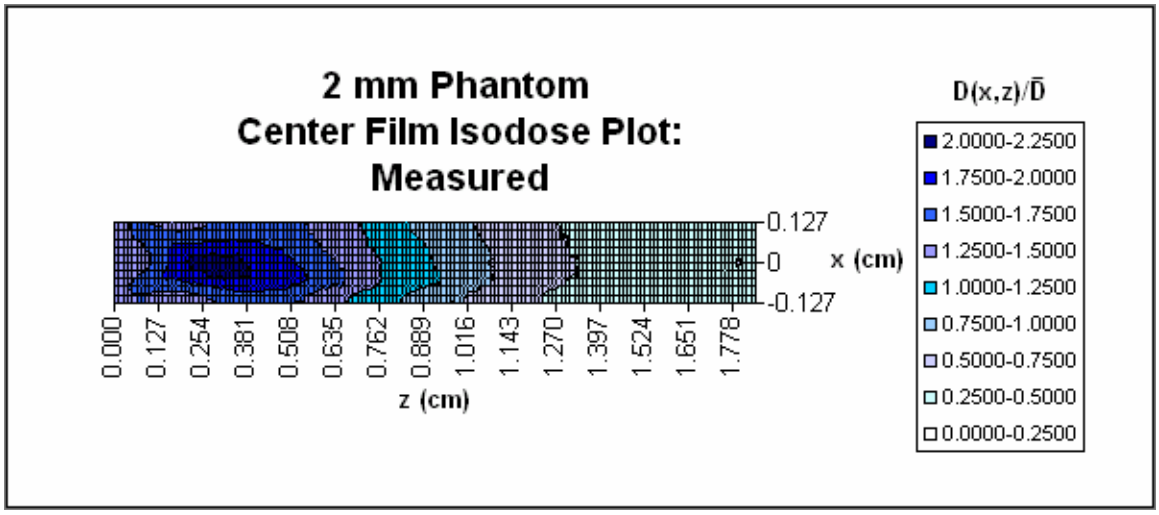

FIGURE 4.12. Measured isodose plot taken from center film region of interest in Figure 4.10.

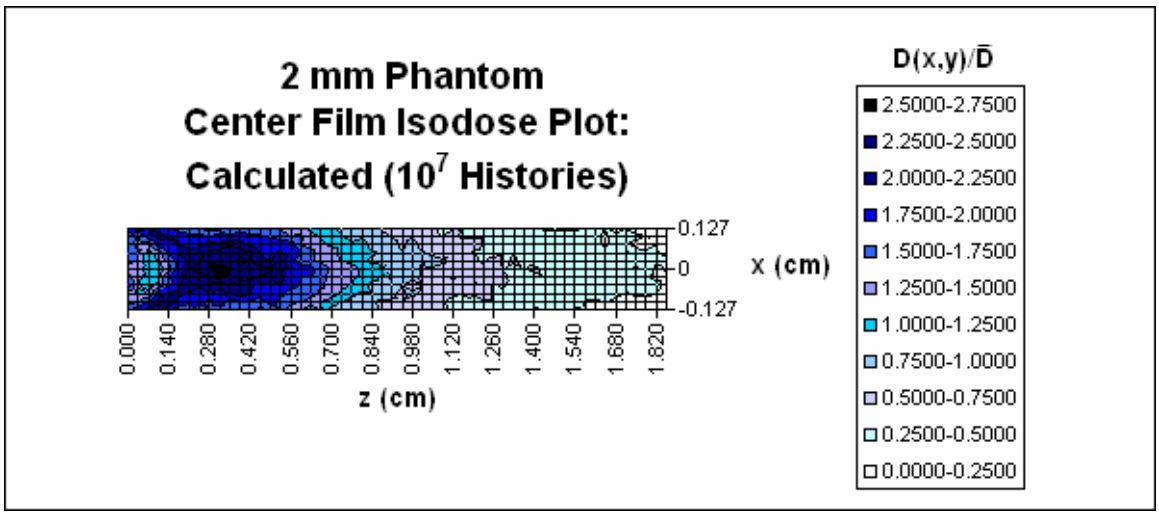

FIGURE 4.13. Calculated isodose plot for center film region of interest in Figure 4.10.

The calculated isodose distribution is shown in Figure 4.13. The channel, transition and contact regions are the same as those for the measured distribution. The region of high dose is smaller, in general, for the calculated distribution. D_{max} also occurs in approximately the same place: x = -0.025 cm and z =0.315 cm.

Figure 4.14 shows the dose vs. depth plot along the midline of the channel. The entrance dose is 1.34 $\overline{D}$ for measured and 1.37 $\overline{D}$ for calculated. The measured dose peak is narrower for the center film than the outer film, ranging from z = 0.2731 cm to z = 0.3366 cm. The calculated D_{max}, 2.54 $\overline{D}$, occurs at z = 0.3325 cm, while the measured value, 2.11D, occurs at z = 0.3111 cm. As with the outer film, calculated dose initially drops with depth (to ~ 1.03D at z = 0.1225 cm), before building up to the maximum. The measured dose drops slightly before building up monotonically to D_{max}. As with the outer film, the calculated dose decreases more rapidly with depth following D_{max} than does the measured dose.

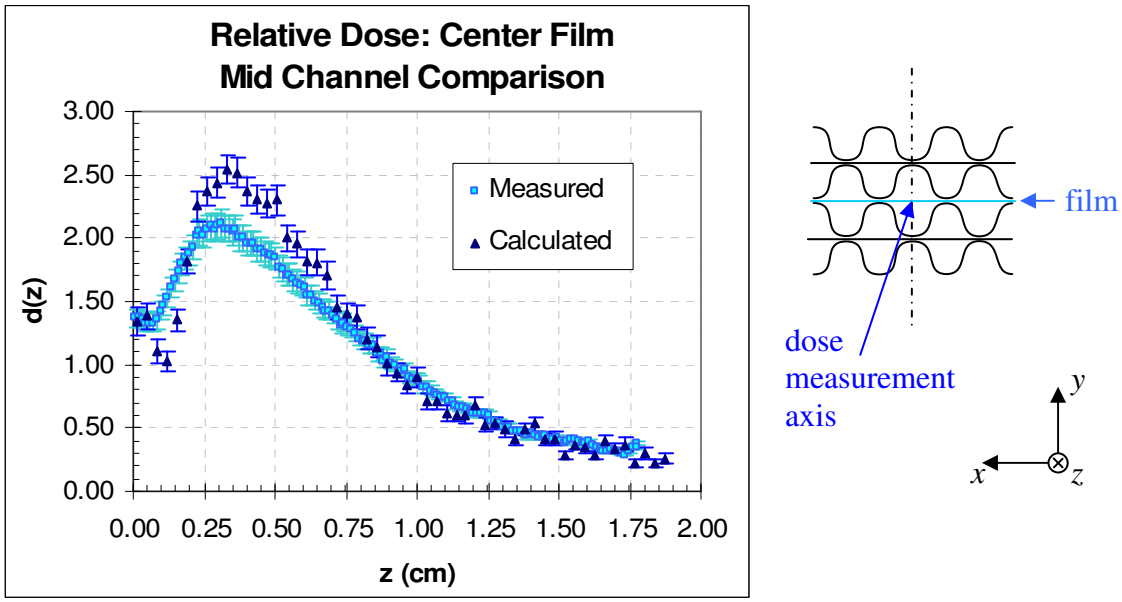

FIGURE 4.14. Dose vs. depth plot along midline of channel.

Figure 4.15 shows the dose vs. depth plot along the borderline between the channel and contact regions. As with the outer film, trends are similar for both measured and calculated dose. They both reach a maximum at approximately the same depth (z = 0.4001 for measured, z = 0.4025 for calculated). As with the channel region, the calculated dose drops before building up to maximum while the measured dose does not. After reaching maximum, the calculated dose decreases more rapidly with depth than does the measured dose.

Figure 4.16 shows the dose vs. depth plot along the midline of the contact region. This region also shows the most difference between measured and calculated distributions. The measured dose starts at $1.45\,\overline{D}$ at $z = 0$ cm, drops to $1.35\,\overline{D}$ at $z = 0.1842$ cm, before increasing to a maximum of $1.65\,\overline{D}$ at $z = 0.4255$ cm, and then decreases monotonically with depth thereafter.

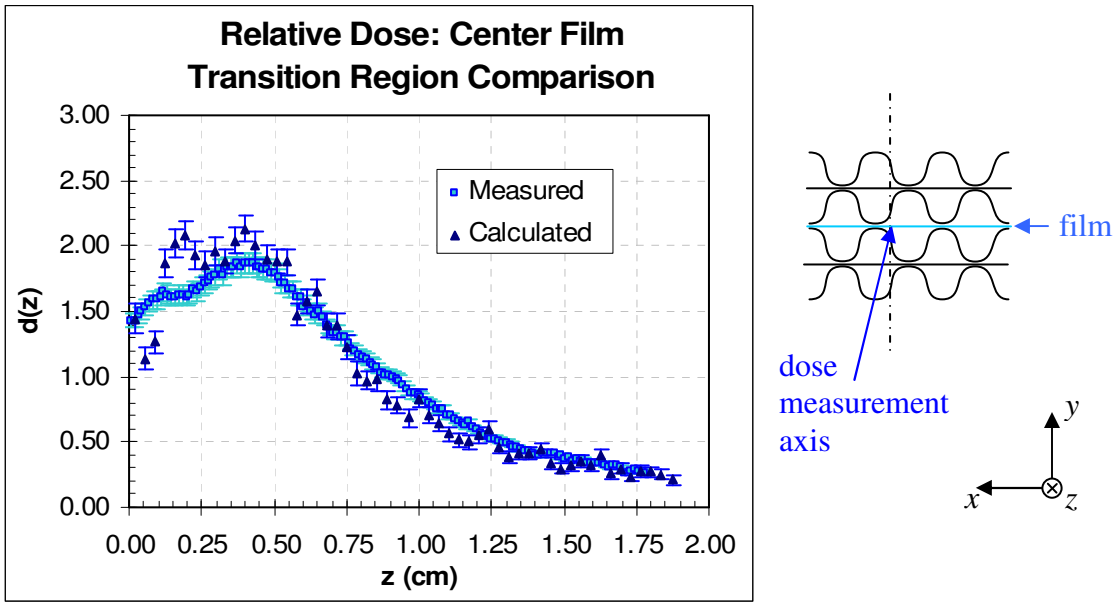

FIGURE 4.15. Dose vs. depth plot along boundary between channel and contact regions.

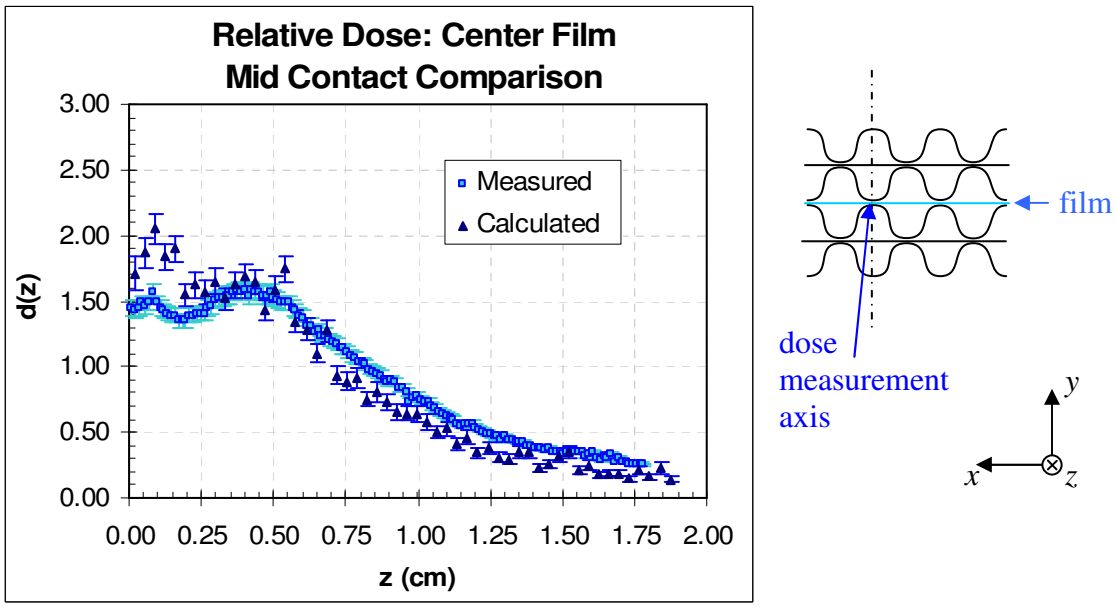

FIGURE 4.16. Dose vs. depth plot along midline of contact region.

The calculated dose rises with depth to a maximum $1.71\,\overline{D}$ very quickly at $z = 0.0875$ cm, and then decreases thereafter. As with the outer film, there is a slight increase superimposed on the attenuation curve, which coincides with the measured $D_{\max}$ at $z = 0.4255$ cm.

4.1.2 5.5 mm Phantom

In the 5.5 mm pitch phantom, the center fold of the film was sampled, from midline of the contact region on one side, to the other (Figure 4.17)

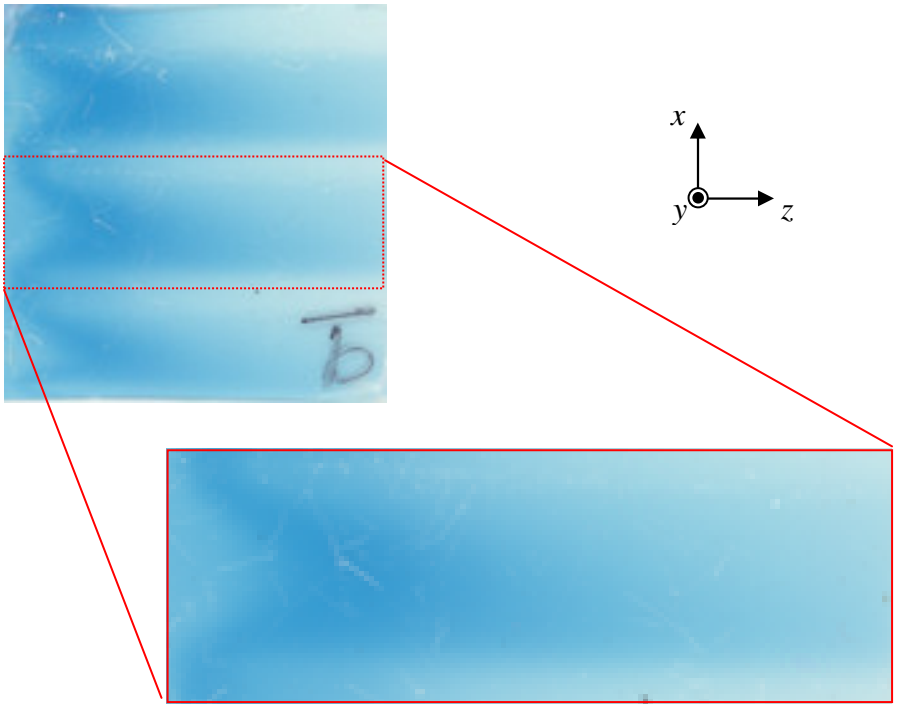

FIGURE 4.17. Film image from 5.5 mm phantom, showing region of interest (highlighted).

The isodose distribution shown in Figure 4.18 is of the measured dose to the region of interest in 4.17. The center of the channel is at x = 0 and the mid-contact regions are at approximately ± 0.3 cm. The transition regions occur at ~ ± 0.18 cm. The region of highest dose appears in the middle of the channel. The maximum dose, D_{max}, occurs along the midline (x = 0) at z = 0.4445 cm. The asymmetry is due to an error in the irradiation angle (θ_x = ~5° instead of 0°) which affects the transition region slightly.

The calculated isodose distribution is shown in Figure 4.19. The channel, transition and contact region values are the same as those for the measured distribution. The

calculated dose distribution differs significantly from the measured dose in that D_{max} occurs in the middle of the contact region as opposed to the channel region, at z = 0.875 cm. There is a very sharp transition between the contact region and the channel region. In the measured dose distribution, this is more gradual.

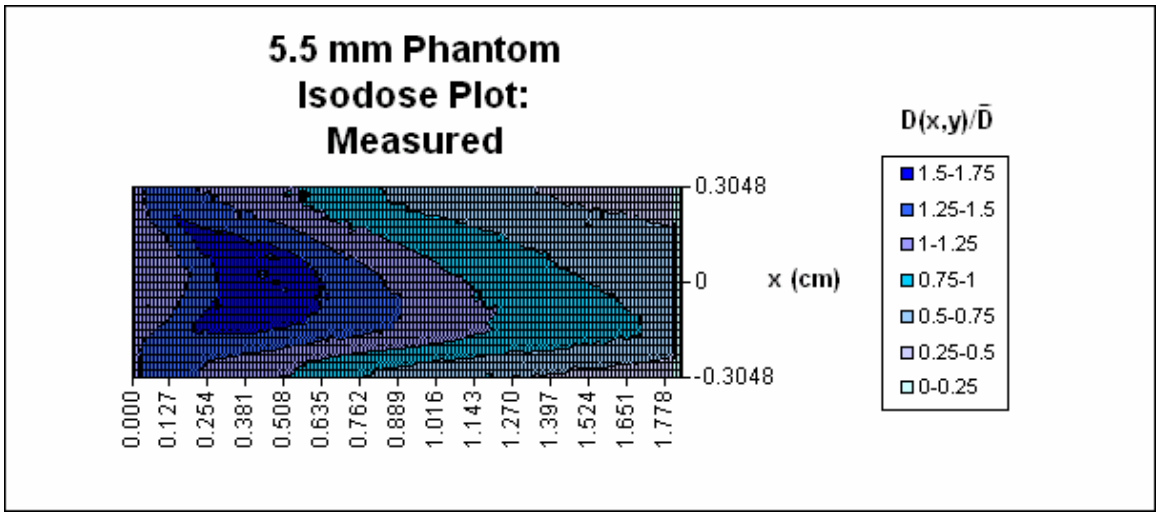

FIGURE 4.18. Measured isodose plot taken from region of interest in Figure 4.13.

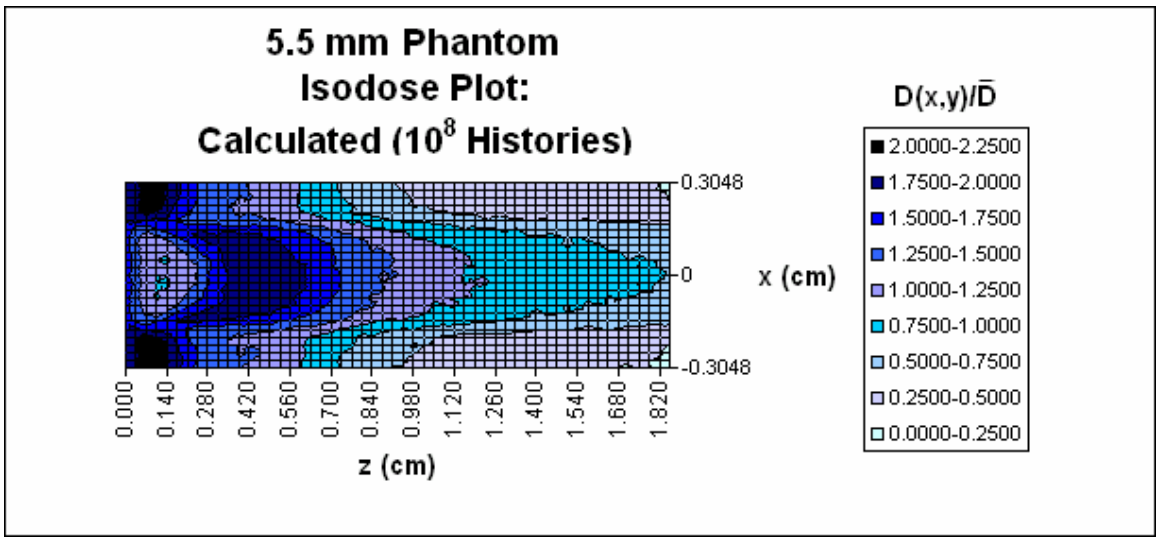

FIGURE 4.19. Calculated isodose plot taken from region of interest in Figure 4.13.

Figure 4.20 shows the dose vs. depth plot along the midline of the channel (x = 0 cm). The entrance dose is $1.08\,\overline{D}$ for measured and $1.57\,\overline{D}$ for calculated. The maximum

occurs at approximately the same depth (z = 0.44 cm) for each. As with the 2 mm pitch phantom, the calculated dose initially drops with depth (to ~ $0.99\,\overline{D}$ at z = 0.1575 cm), before building up to the maximum, while the measured dose builds up monotonically to D_{max}. The peaks are approximately equivalent in width, and the calculated and measured doses decrease with depth equally.

Figure 4.21 shows the dose vs. depth plot along the borderline between the channel and contact regions. The main difference is in the maximum value ($1.48\,\overline{D}$ measured, $1.78\,\overline{D}$ calculated) and where it occurs (z = 0.1334 cm measured, z = 0.0525 cm calculated). Both the calculated and measured doses decrease equally with depth.

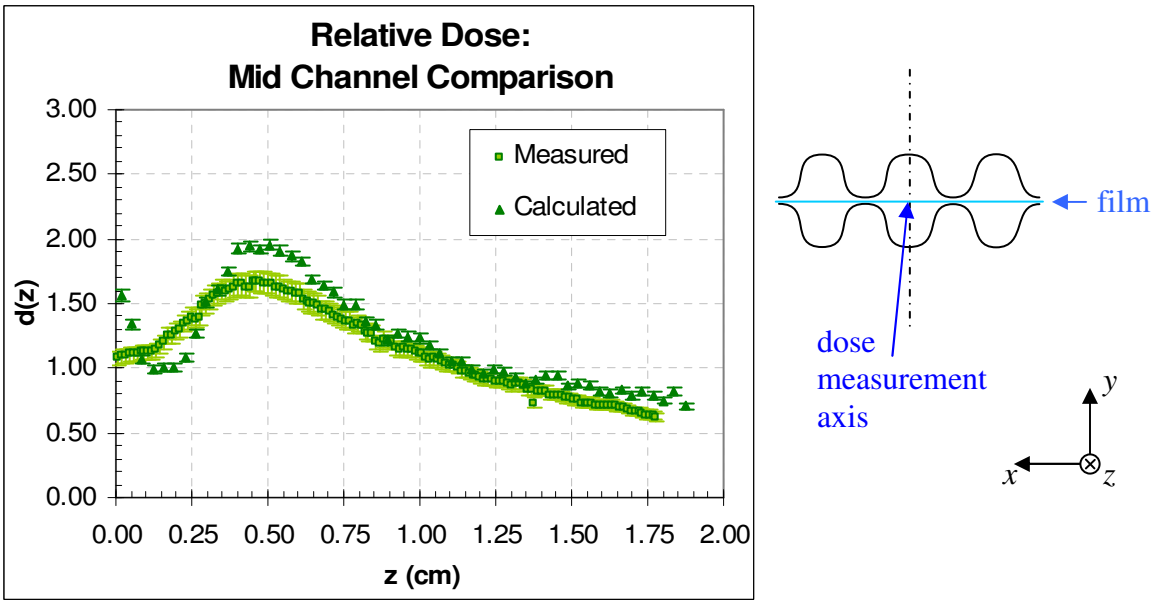

FIGURE 4.20. Dose vs. depth plot along midline of channel.

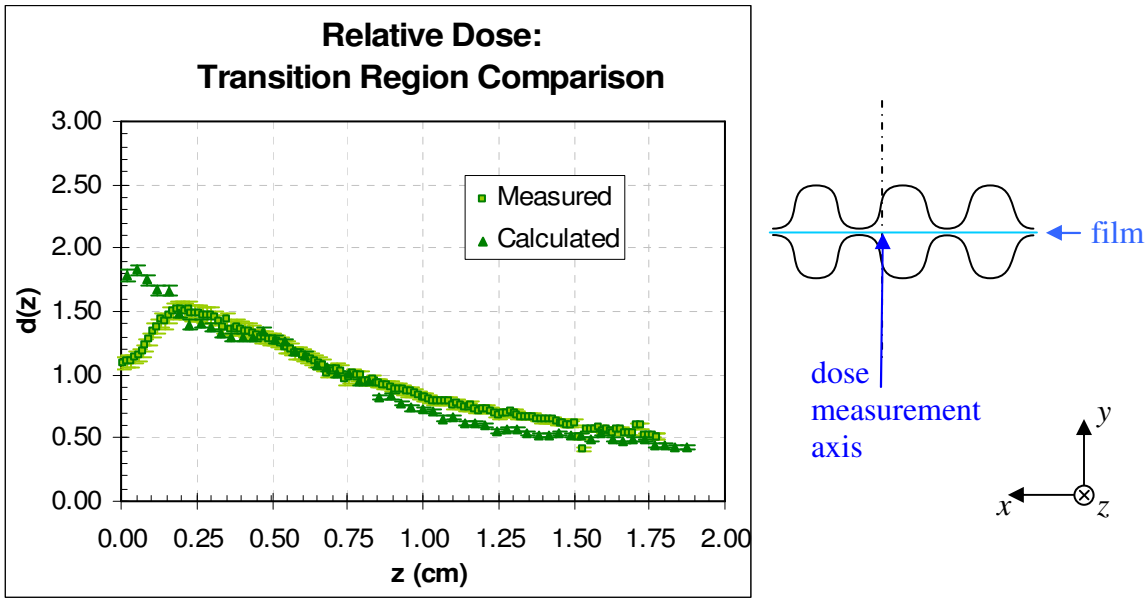

FIGURE 4.21. Dose vs. depth plot along boundary between channel and contact regions.

Figure 4.22 shows the dose vs. depth plot along the midline of the contact region. In contrast with the 2 mm phantom, this region shows the most similarity between measured and calculated distributions. The measured dose starts at $1.06D$ at $z = 0$ cm, increases to a maximum of $1.47\,\overline{D}$ at $z = 0.1207$ cm, and then decreases monotonically with depth thereafter. The calculated dose starts at $1.76\,\overline{D}$ of at $z = 0$ cm, increases to a maximum of $2.13\,\overline{D}$ at $z = 0.0875$ cm, and then decreases monotonically with depth thereafter. This is the only region in the phantom where the calculated dose decreases more rapidly with depth than the measured dose.

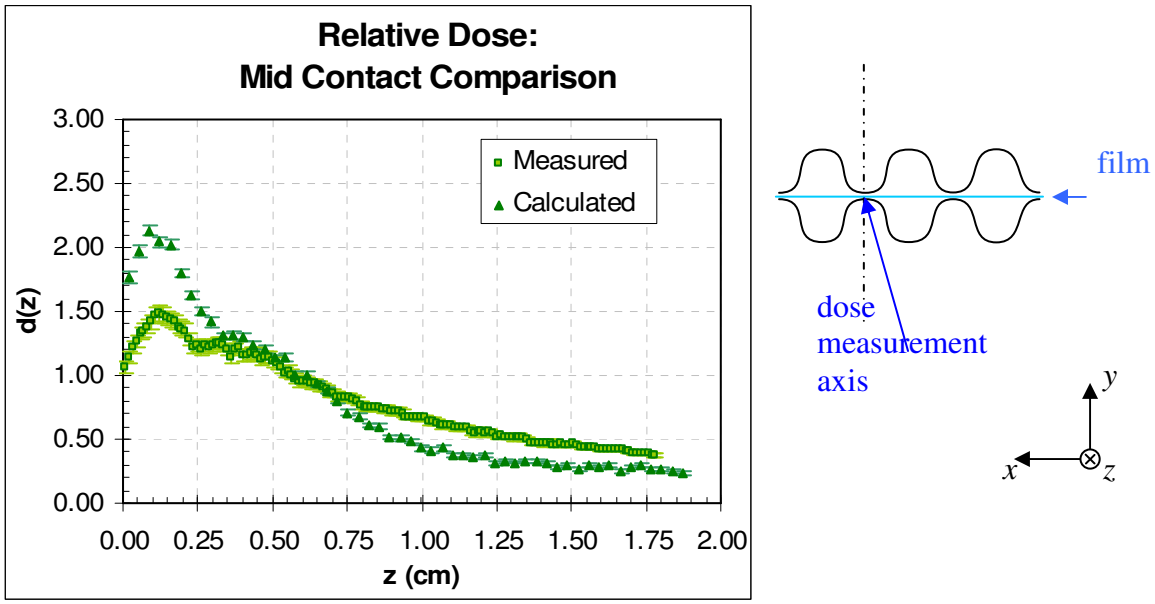

FIGURE 4.22. Dose vs. depth plot along midline of contact region.

4.3 Summary of Observations

When comparing measured and calculated dose distributions, the following trends were observed.

a. Entrance dose region:

- Calculated and measured doses are approximately equal in channel region. (2 mm phantom).
- Calculated dose greater in channel region (5.5 mm phantom).

b. Buildup region:

- Measured dose increases directly to D_{max} in channel. Calculated dose drops before increasing to D_{max} (2 mm and 5.5 mm).
- Maximum occurs at entrance in 5.5 mm contact region.

c. After D_{max}:

- Measured and calculated doses both decrease more rapidly with depth in channel region (2 mm and 5.5 mm) than in contact region.

- Calculated dose decreases more rapidly with depth than measured for 2 mm and 5.5 mm channel region.

- Calculated and measured dose decrease equally with depth in contact and transition region.

d. General

- Measured dose non-uniformity is greater for 2 mm phantom than for 5.5 mm phantom ($2\overline{D}$ vs. $1.7\overline{D}$).

- Calculated dose distributions show greater non-uniformity than measured dose ($2.5\overline{D}$ vs. $2.0\overline{D}$ for 2 mm phantom, $2.2\overline{D}$ vs. $1.5\overline{D}$ for 5.5 mm phantom).

CHAPTER V

DISCUSSION

In this chapter, the differences between the measured and calculated dose distributions are explored in both the quantitative and qualitative aspects.

5.1 Quantification of Differences Between Measured and Calculated Dose, as a Function of Topographical Features of Phantom

5.1.1 Relative Error in Voxel Map

Due to limitations in the Monte Carlo software, it was not possible to exactly model the phantom. However it was possible to approximate the phantom to within 5-6% on all critical dimensions (Figure 5.1, Table 5.1).

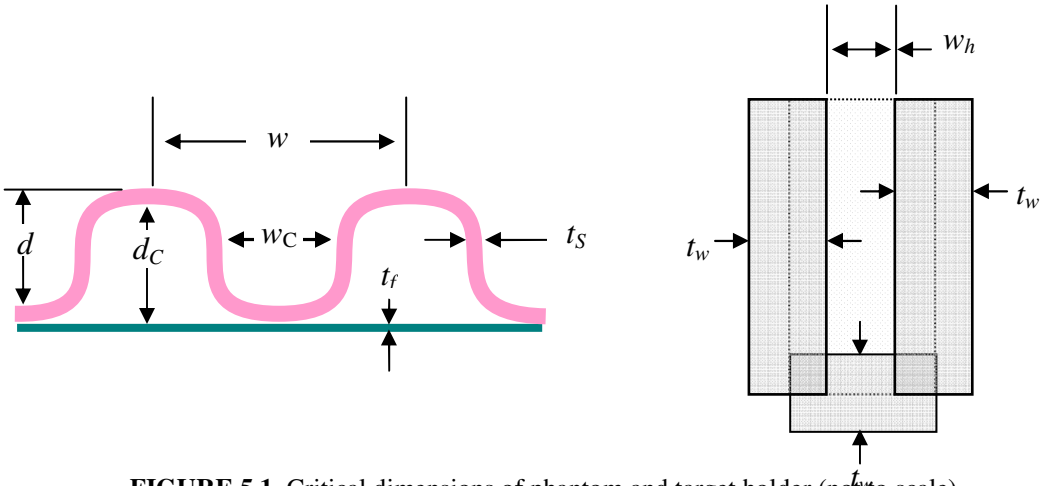

FIGURE 5.1. Critical dimensions of phantom and target holder (not to scale).

These errors could be reduced further by finely adjusting the dimensions of the voxels. But this would introduce other difficulties. As it is currently modeled, the film pixels and model voxels are of approximately the same dimension . Changing these dimensions will

make matching the points of comparison more difficult and offset the modest reduction in dimensional error here.

TABLE 5.1
Percent difference between phantom and voxel map dimensions

		Value		
Parameter	Symbol	Measured	Modeled	% deviation
Film thickness	t_f	0.0110 cm	0.0110 cm	0.00%
Tile thickness	t_S	0.0508 cm	0.0500 cm	-1.57%
2 mm tile depth	d	0.1219 cm	0.1250 cm	2.53%
2 mm channel depth	d_C	0.0711 cm	0.0750 cm	5.46%
2 mm width	w	0.2743 cm	0.2750 cm	0.25%
5.5 mm depth	d	0.2600 cm	0.2625 cm	0.95%
5.5 mm channel depth	d_C	0.2092 cm	0.2125 cm	1.56%
5.5 mm width	w	0.6000 cm	0.5750 cm	-4.17%
Target holder (2 mm)	w_h	0.5311 cm	0.5330 cm	0.36%
Target holder (5.5 mm)	w_h	0.5311 cm	0.5360 cm	0.92%
Wall thickness	t_w	0.5842 cm	0.5842 cm	0.00%

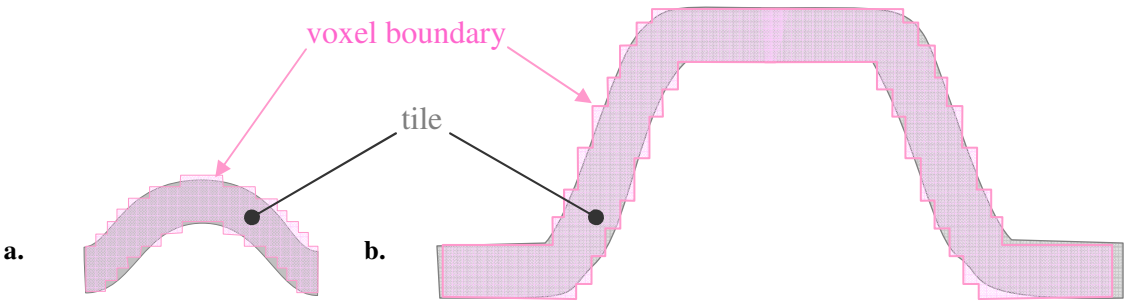

FIGURE 5.2. Voxel map vs. segment of tile for **a.** 2 mm phantom and **b.** 5.5 mm phantom.

What is more significant is the set of "coarse element" errors as discussed in section 2.2.1. Figure 5.2 shows the overlap and underlap of the voxel map, when compared to the actual tiles. The maximum fraction of a voxel that has a density different than the density of the phantom at that location is approximately 30%. However there is approximately an equal amount of overlap and underlap in the tile voxels, so the net scattering and buildup to the film is within ~5% of the actual tiles. This would be a more significant issue if

scoring in the tiles was being considered. However, the film dose is of primary interest here, and it *is* modeled exactly.

5.1.2 Simplified Models of Phantom Components

In an attempt to understand the limitations of the Monte Carlo calculations and understand the contribution of each component to the difference between calculated and measured doses, simplified models were made to simulate each component of the phantom and the dose was calculated for them. The simulated channel was simply a layer of styrene on either side of the film at a distance equal to the depth of the channel d_C (Figure 5.3.a). The simulated contact region was modeled by placing the styrene in contact with the film on either side (Figure 5.3.b). The simulated transition region consisted of styrene tile perpendicular to the film extending a distance equal to the tile depth d on either side (Figure 5.3.c). In each of the three models, the film was surrounded on both sides by acrylic representing the target holder.

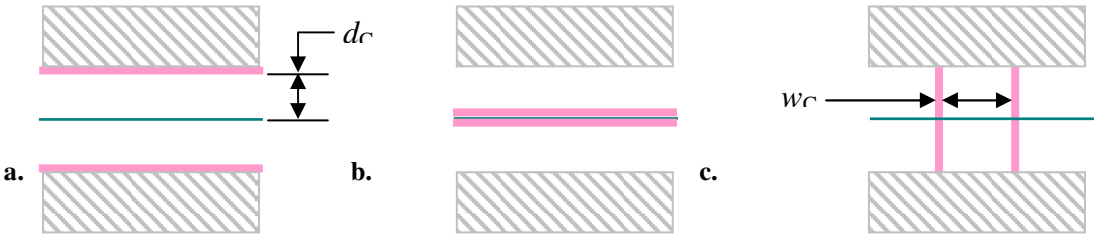

FIGURE 5.3. Simulated model for **a.** Channel, **b.** Contact, **c.** Transition (not to scale).

2mm Phantom

Analysis of the simulated channel region of the 2 mm phantom is shown in Figure 5.4.

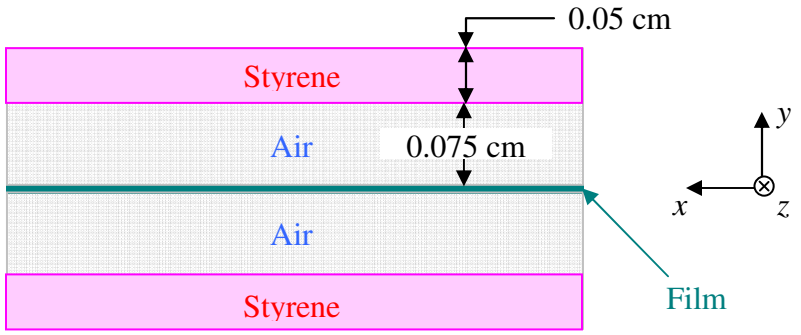

FIGURE 5.4. Simulated channel region for 2 mm phantom.

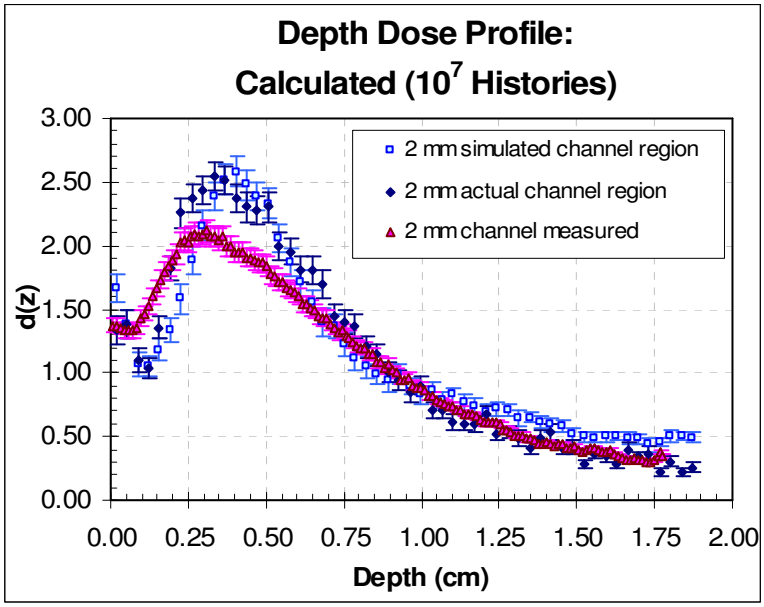

FIGURE 5.5. Calculated doses for simulated channel region.

The diagram is a scale representation of the simulated channel region, showing dimensions. Figure 5.5 is a plot of the calculated dose vs. depth for the simulated channel region. The measured and calculated dose values for the actual phantom channel are

included in the plot for comparison. The simulated curve is closer to the actual calculated region than it is to the measured. Both calculations exhibit the same degree of dose underestimate in the first 0.25 cm and overestimate in the second 0.25 cm. The calculated dose values begin to diverge beyond about 1.2 cm with the actual phantom calculations decreasing faster.

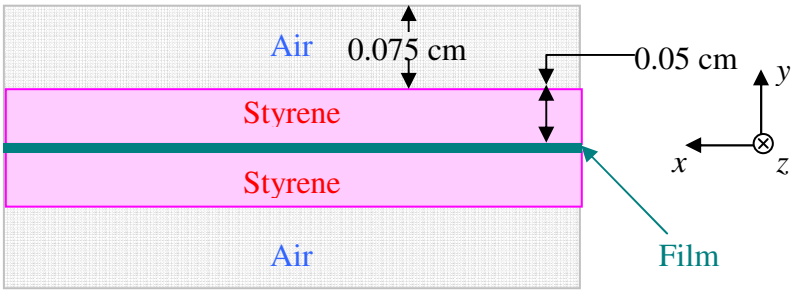

FIGURE 5.6. Simulated contact region for 2mm phantom.

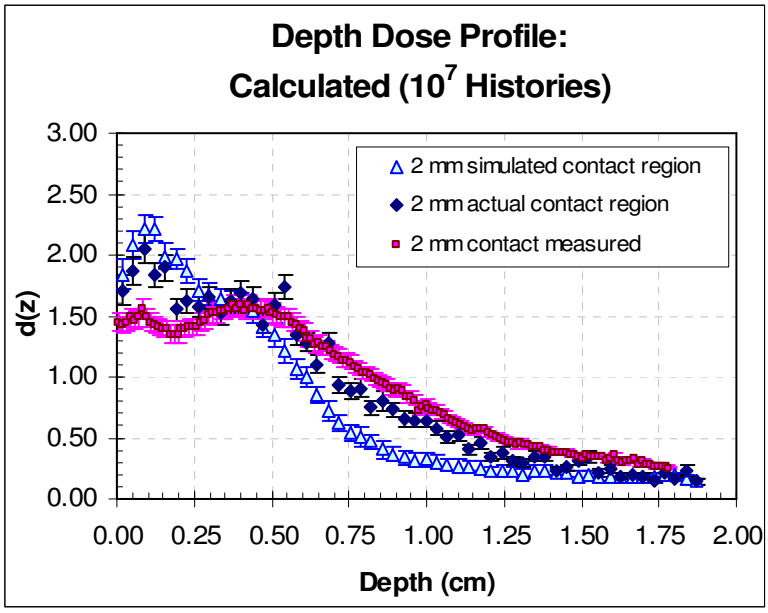

FIGURE 5.7. Calculated doses for simulated contact region, 2mm phantom.

Figure 5.6 is a scale representation of the simulated contact region, showing dimensions. Figure 5.7 is a plot of the calculated dose vs. depth for the simulated contact

model, with the measured and calculated dose values for the actual phantom channel included for comparison. As with the channel region, the simulated and actual contact region calculated doses are largely more similar to each other than they are to the measured dose. However, beyond about 0.6 cm the actual calculated values decrease more slowly, and re closer to measured values up to about 1.2 cm.

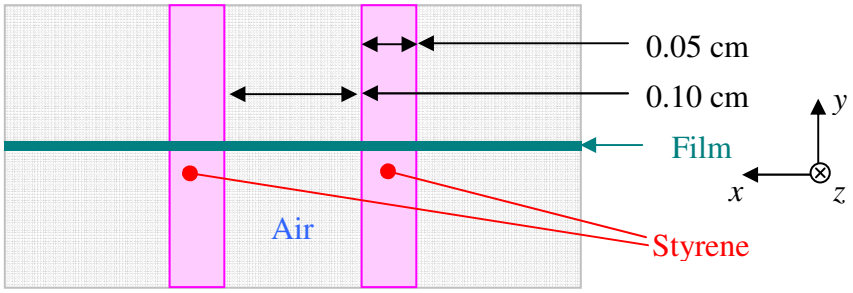

FIGURE 5.8. Simulated transition region for 2mm phantom.

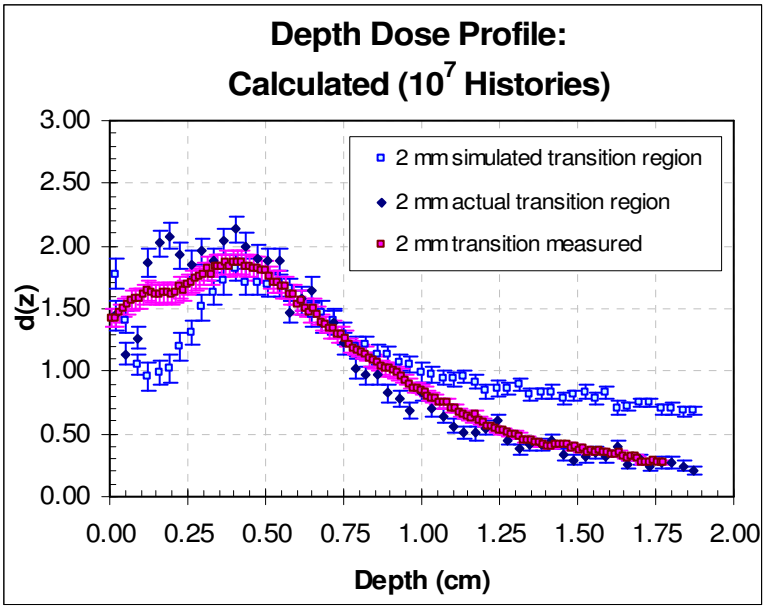

FIGURE 5.9. Calculated doses for simulated transition region, 2mm phantom.

Figure 5.8 is a scale representation of the simulated transition region, showing dimensions Figure 5.9 is a plot of the calculated dose vs. depth for the simulated contact

model, with the measured and calculated dose values for the actual phantom channel included for comparison. This case shows the greatest amount of difference in calculated values between the simulated and actual transition regions. In the actual phantom, there is a contribution from the neighboring regions. In-scattering is expected more from the contact region in the first few mm due to the greater density of (and shorter electron range in) the material.

5.5mm Phantom

The 5.5mm phantom was also analyzed. Figure 5.10 shows the depth dose curves for the simulated channel region along with calculated and measured values for the actual channel. In contrast to the 2 mm phantom, the calculated dose in the simulated channel region is now much closer to the measured dose than the calculated dose for the actual channel. When the contact region is simulated (Figure 5.11), it is closer to the measured dose for the actual region. It is the simulated region that most closely matches the actual region. The highest calculated dose occurs in the contact region for both the actual and simulated 5.5 mm phantom, while the highest measured dose occurs in the channel region

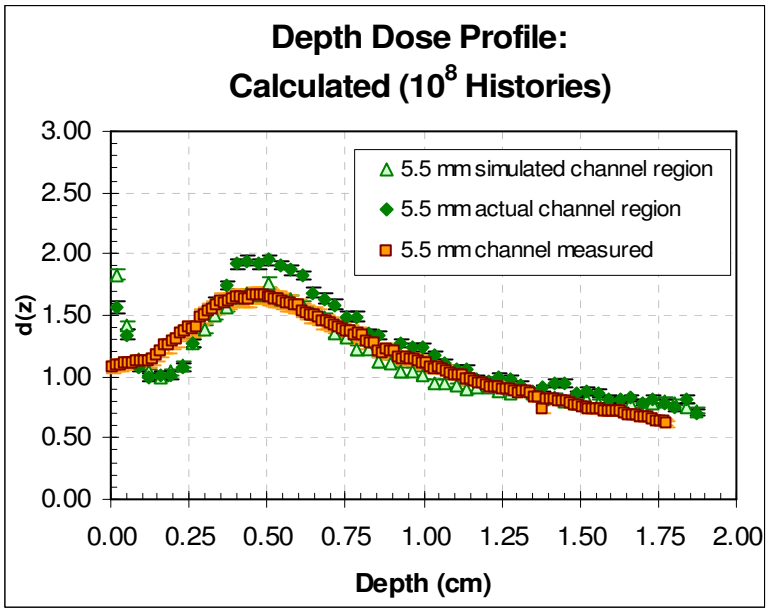

FIGURE 5.10. Calculated doses for simulated channel region, 5.5mm phantom.

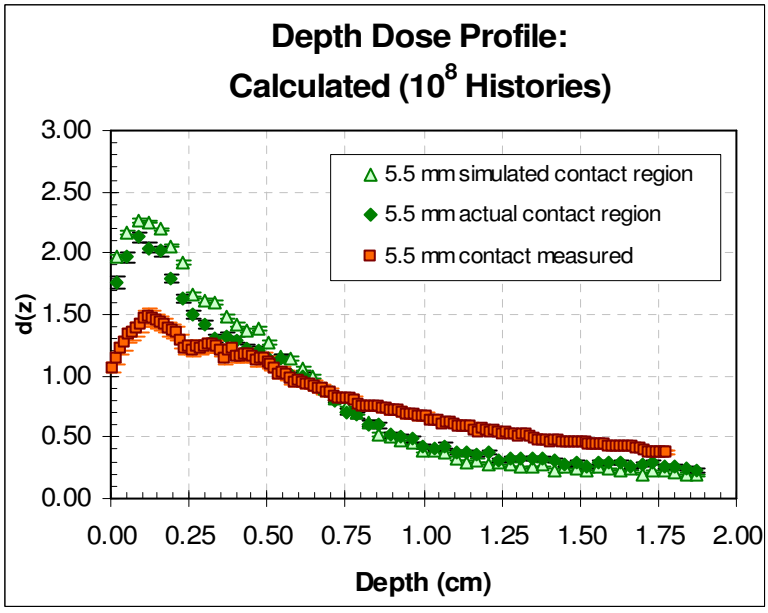

FIGURE 5.11. Calculated doses for simulated contact region, 5.5mm phantom.

5.1.3 Direct Comparison of Measured and Calculated Dose

Re-binning of Measured Depth Dose Curves

To directly compare measured and calculated dose d, they must be compared at an equivalent depth z. In their original format the z-axes of the measured and calculated doses were not equivalent due to voxel limitations in the z direction, which represented depth. It was therefore necessary to re-bin the measured values so that their z values were equivalent with those of the calculated dose. The measured values had a higher resolution (0.0127 cm) than the calculated values (0.035 cm) so a re-binning was possible by way of linear interpolation:

$$d_{M_i \to C_i} = d_{M_i} + \frac{z_{C_i} - z_{M_i}}{z_{M_{i+1}} - z_{M_i}} (d_{M_{i+1}} - d_{M_1}) \tag{5.1}$$

where $z_{M_i} < z_{C_i} < z_{M_{i+1}}$.

2 mm Phantom

Figure 5.12 shows a plot of the difference between measured and calculated values for the channel region of the 2 mm phantom. The y axis is the percent difference of d_{calc} - d_{meas}. The solid red line at zero represents equivalence of calculated and measured values. The dotted lines represent the maximum magnitude of the measured dose error bars, ± 4% of d_{meas}. Points above the range represent overestimates by the simulation, while those outside and below the range represent underestimates. The calculation underestimates the measured dose by approximately 32.9% at z = 0.1225 cm, and then overestimates by 23.3% just following the maximum value, or D_{max}, at z = 0.3675 cm.

The deviation drops to 2.16% at z = 0.9975 cm and increases randomly (as noise) for the remainder of z.

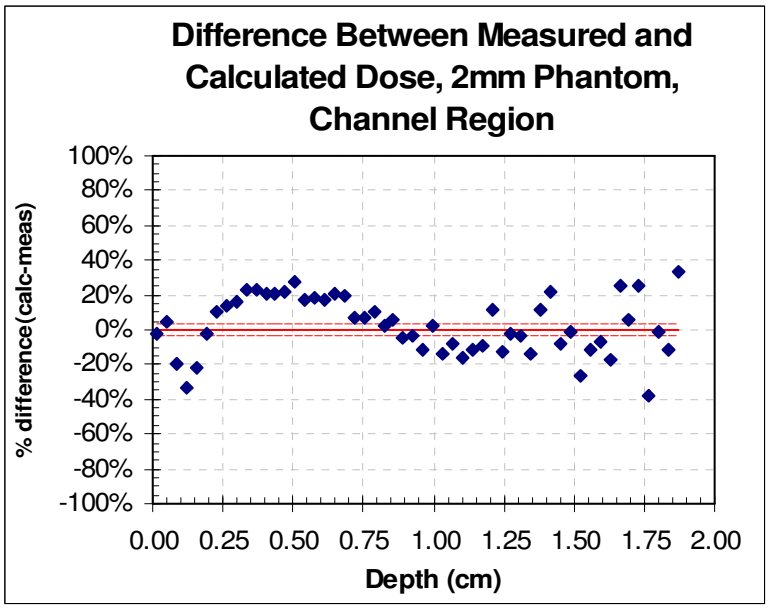

FIGURE 5.12. $D_{calc} - D_{meas}$ for 2 mm phantom, channel region.

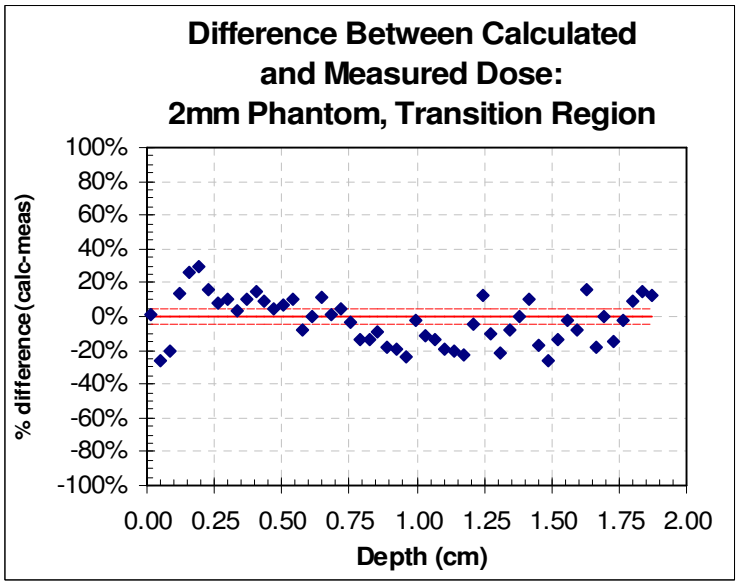

FIGURE 5.13. $D_{calc} - D_{meas}$ for 2 mm phantom, transition region.

Figure 5.13 shows a plot of the difference between measured and calculated values for the transition region of the 2 mm phantom. The measured dose is underestimated by

25.6% in the first 0.1 cm of z, and then rises to ~ 29.0% at 0.2 cm. The calculation decreases to an underestimate of about 20% at z = 0.92 cm and then continues roughly within ± 25% for the remainder of z.

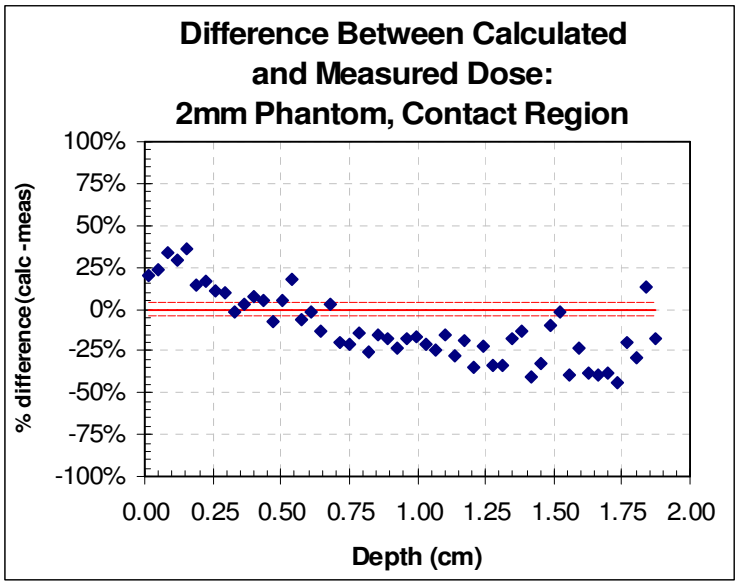

FIGURE 5.14. $D_{calc} - D_{meas}$ for 2 mm phantom, contact region.

Figure 5.14 is a plot of the difference between measured and calculated values for the contact region of the 2 mm phantom. The dose is consistently overestimated for z < 0.4 cm, reaching 36.8 % at z = 0.1575 cm. Beyond that it is primarily underestimated, reaching -43.7% at z = 1.7325 cm

In summary, the measured dose is mostly over-estimated by the calculation for z < ~ 0.75 cm and mostly under-estimated beyond that. There is also some under estimate of measured dose in the first few mm of z in the channel and transition regions but not in the contact region. Because the dose values are normalized to the mean dose $\overline{D}$, the dose is underestimated by the calculation approximately 50% of the time while overestimated the rest of the time.

5.5 mm Phantom

Figure 5.15 is a plot of the difference between measured and calculated values for the channel region of the 5.5 mm phantom. An underestimate of 20.2% occurs at z = 0.1925 cm and then increases to 19.4% at z = 0.4375 cm. It drops to within 10% for z = 1.0675 cm through z = 1.3475 cm, before gradually diverging in the positive direction.

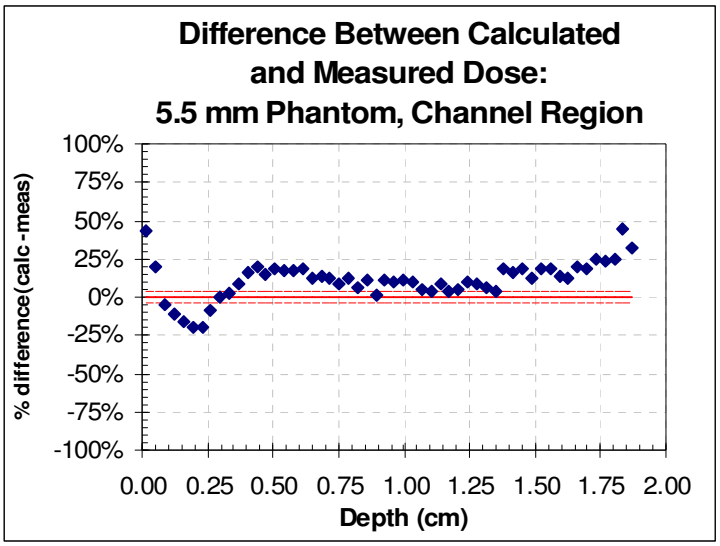

FIGURE 5.15. $D_{calc} - D_{meas}$ for 5.5 mm phantom, channel region.

Figure 5.16 is a plot of the difference between measured and calculated values for the transition region of the 5.5 mm phantom. The measured dose is consistently overestimated in the first 2 mm, staring at 61.1 % at z = 0 and decreasing monotonically to zero at z = ~0.2 cm. It remains within -10% out to z = 0.82 cm and then gradually decreases to -15-20% thereafter. The "spike" at around z = 1.5 cm is due to scratches on the film.

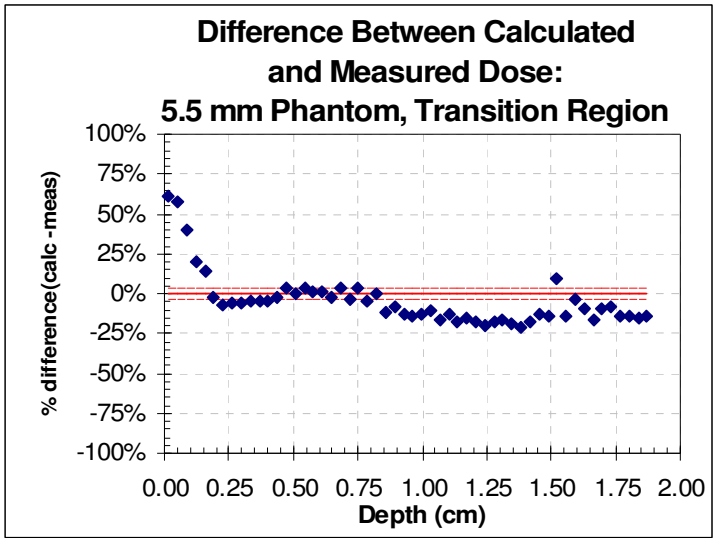

FIGURE 5.16. $D_{calc} - D_{meas}$ for 5.5 mm phantom, transition region.

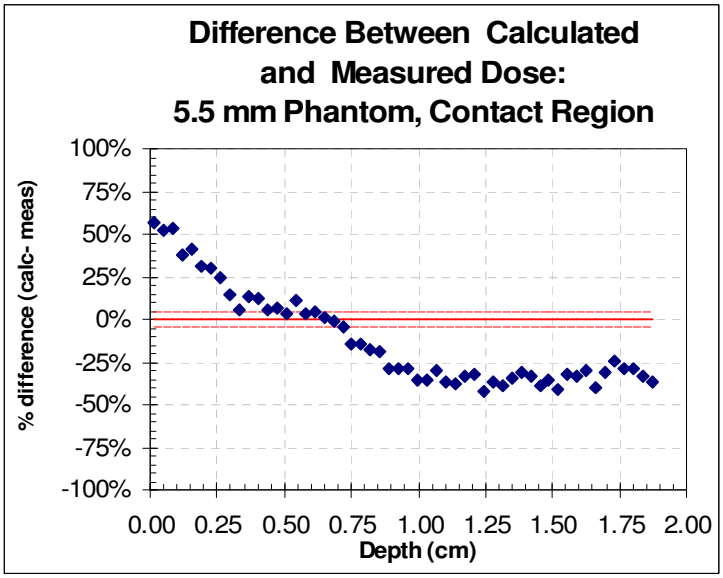

FIGURE 5.17. $D_{calc} - D_{meas}$ for 5.5 mm phantom, contact region.

Figure 5.17 is a plot of the difference between measured and calculated values for the Contact region of the 5.5 mm phantom. $D\max|_{calculated}$ occurs in this region at d = 0.0875 (0.0127 cm off the centerline in y) and the calculated dose is overestimated by + 53.0%. By contrast $D\max|_{measured}$ occurred mid channel region. Beyond this depth it drops monotonically to -35.4% at z = 0.9975 cm and slowly increases to -30-40% at the end of the phantom.

In summary, the maximum deviation from measurement is an overestimate of 56.4% which occurs at the entrance of the contact region. The maximum underestimate is 42.7%, which occurs at the z = 0.127 cm in the contact region. The calculated dose is overestimated in the channel region beyond z = 0.4 cm, while is it underestimated in the transition and contact region.

5.1.4 Decomposition of Depth Dose Curves

The depth dose curve can be decomposed into two main components: a). attenuation and b). scattering. Component a is the simple stopping power curve for the film. Component b represents scattering from the other structures in the phantom into the film. (Figure 5.18).

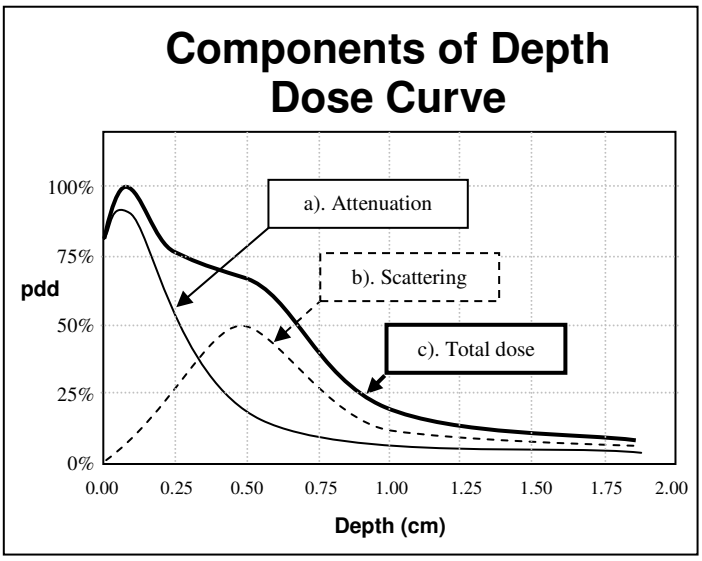

FIGURE 5.18. Decomposition of a depth dose distribution curve.

The attenuation component will primarily be produced by the film itself, as it is too thin to produce measurable build-up from internal scattering events. The scattering component will occur from several sources. The layers of styrene in the phantom, the walls of the target holder, the other layers of film, and the intervening air. All the physical components are accounted for in the voxel map. The decompositions of the calculated curves are shown in Figures 5.19 and 5.20.

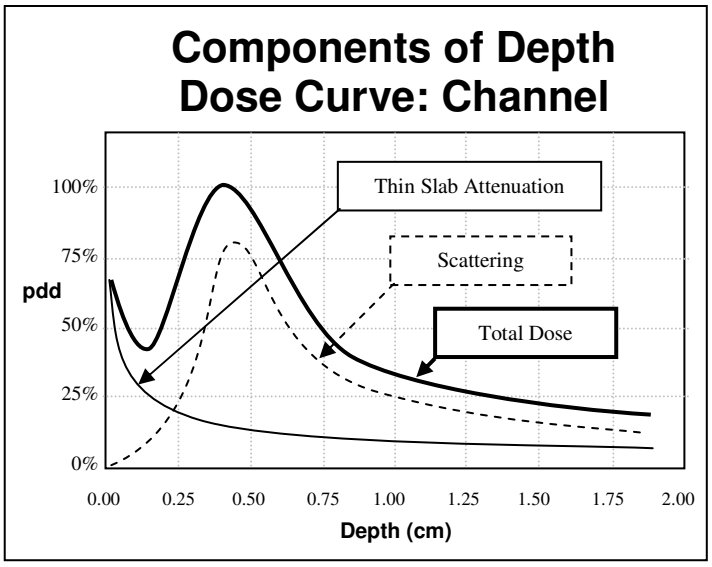

FIGURE 5.19. Decomposition of depth dose curves in channel region.

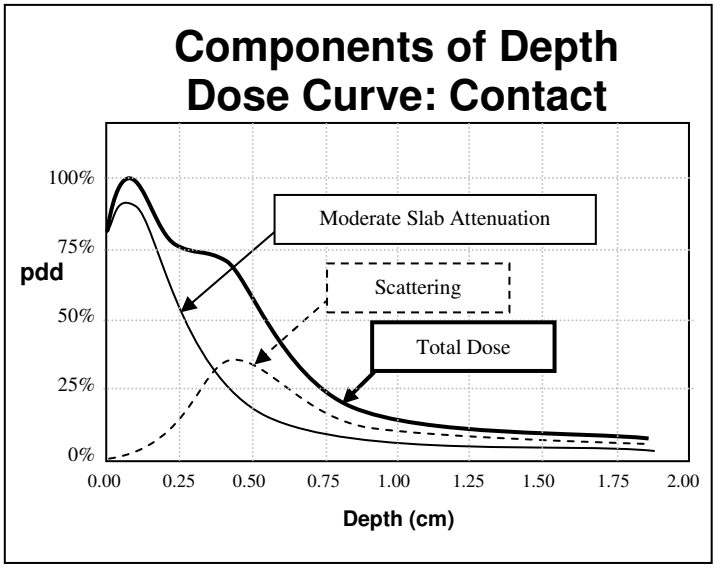

FIGURE 5.20. Decomposition of depth dose curves in contact region.

2mm Phantom

Figure 5.21 shows the summary of difference between calculated and measured dose for the 2mm phantom. This time, the difference is taken by subtracting calculated from measured, so positive values in Figure 5.25 represent an underestimate of the dose.

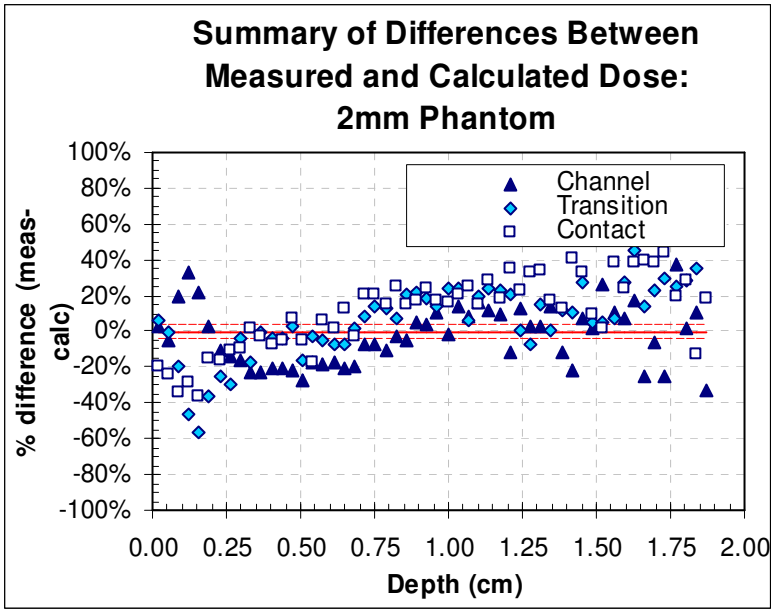

FIGURE 5.21. Summary of calculated dose subtracted from measured dose for ROI in 2 mm phantom.

The primary "missing" component appears to be a scattering component in the first 0.22 cm of the channel region. However, roughly the same degree of *over*estimate (or "added" component) appears in the transition and contact regions. There also appears to be a second scattering component missing between 0.75 cm and 1.25 cm, particularly in the transition and contact regions.

5.5mm Phantom

Figure 5.22 shows the difference between calculated and measured dose for the 5.5 mm phantom. Trends are similar to the 2mm phantom, except that the "missing" scattering component is greater in the contact region beyond about 0.75 cm. Since there are overestimates in this phantom as well, decomposition of depth dose curves is inconclusive.

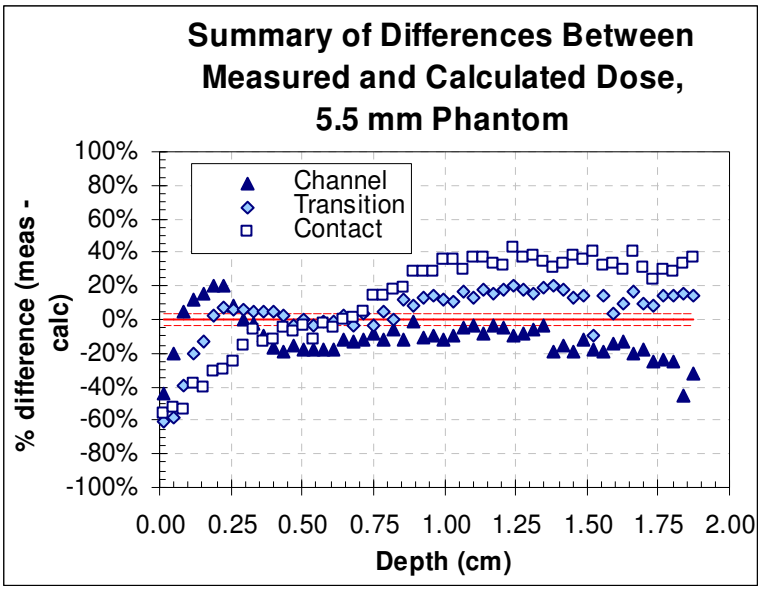

FIGURE 5.22. Summary of calculated dose subtracted from measured dose for ROI in 5.5 mm phantom.

5.1.5 Regions of Greatest Error

The errors in the region beyond about z = 1.25 cm can be disregarded. The dose values for z >1.25 cm are approaching zero, causing all % difference values to approach 100%. For depths of $z \leq 1.25$ cm, the greatest error (~60%) occurs in the entrance region of $z < 0.23$ cm. This is about 1/3 of the CSDA range for 1.35 MeV electrons in polyester

0.67 cm. Over 90% of the thin target attenuation dose is dissipated in this region (Figures 5.23 a and b)

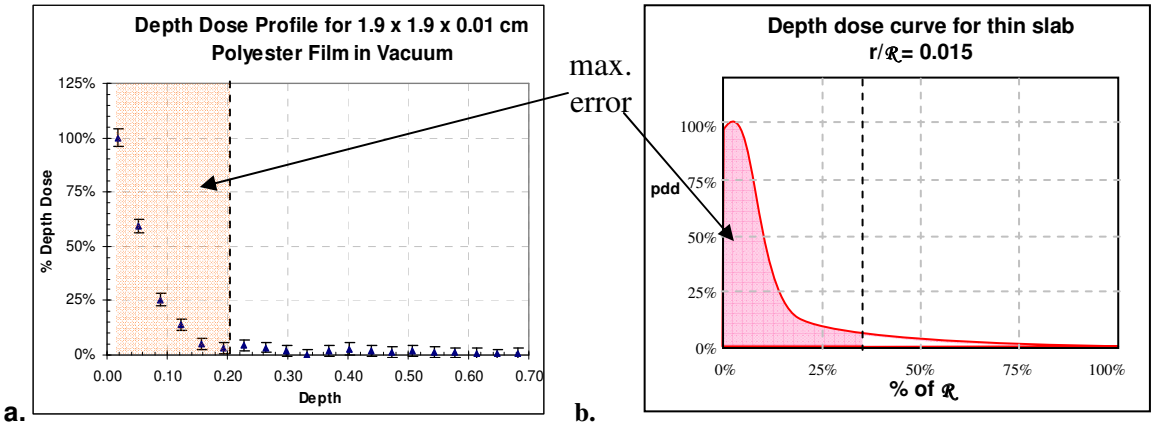

a. **b.**

FIGURE 5.23. a. Calculated depth dose profile for 0.01 cm thin film **b.** Depth dose curve for circular beam, r/ℛ= 0.015.

5.2 Characterizing Areas of Uncertainty and Non-Uniformity

This section details ways to develop predictions of uncertainty and non-uniformity of dose, which can be applied to our phantom as well as other designs.

5.2.1 Examination of Factors Affecting Dose

There are many factors which contribute to the dose distribution in any irradiated object. In chapter II, the beam geometry was mentioned. In the case of our experiment, the beam width was equal to approximately half the electron range in air, and many times the electron range in the phantom materials.

Dose to medium

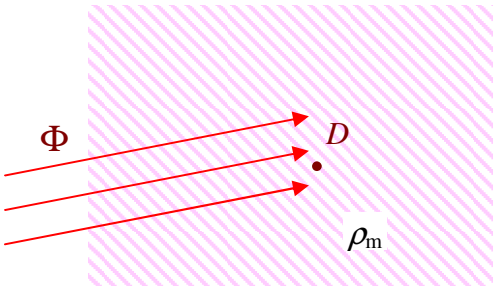

FIGURE 5.24. Dose to a medium *m*.

For a particular medium *m* with density ρ_m (Figure 5.24) irradiated by monoenergetic charged particles with incident energy E_i, the dose *d* at any given point in the is the product of the particle fluence Φ and the mass stopping power (*1/ρ* * *dT/dx*), (*19*) :

$$d_m(T) = \Phi\left[\frac{1}{\rho_m}\left(\frac{dT}{dx}\right)_c\right] = \Phi\left[\left(\frac{dT}{\rho dx}\right)_{c,m}\right]_T \qquad (5.2a)$$

T is the kinetic energy at the point of interest and *dT/dx* is evaluated at that point. The dose over the particle track (D_m) is the integral of the dose over the entire particle energy range:

$$D_m = \int_0^{E_i} d_m(T)dT = \int_0^{E_i} \Phi\left[\frac{1}{\rho_m}\left(\frac{dT}{dx}\right)_c\right]dT = \int_0^{E_i} \Phi\left[\left(\frac{dT}{\rho dx}\right)_{c,m}\right]_T dT \qquad (5.2b)$$

Interfaces and Boundary Effects

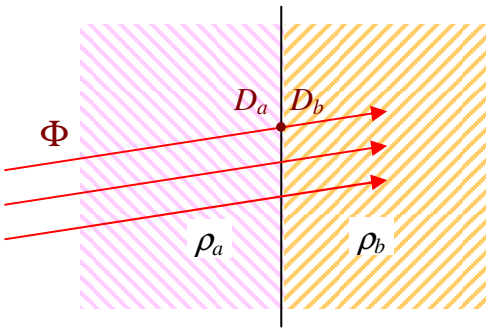

FIGURE 5.25. Interface between medium *a* and medium *b*.

In a typical irradiation scenario for leafy vegetable there will be thin (< 0.1 mm) leaves on the order of a few cm in width in contact with air gaps on the order of a few mm in depth. Due to the large number and relatively small sizes of the food items involved, there will be many of these interfaces, so the effects of such are of prime interest. If Φ is continuous across the boundary between medium *a* and medium *b* (Figure 5.25), then the dose ratio D_a/D_b is simply the ratio between the mass stopping powers (*20*):

$$\frac{D_b}{D_a} = \frac{(dT/\rho dx)_{c,a}}{(dT/\rho dx)_{c,b}} \tag{5.3}$$

$${}_m\overline{S}_a = \frac{\int_0^{T_{\max}} D_a dT}{\int_0^{T_{\max}} \Phi(T) dT} = \frac{\int_0^{T_{\max}} \Phi(T)\left(\frac{dT}{\rho dx}\right)_{c,a} dT}{\int_0^{T_{\max}} \Phi(T) dT} = \frac{1}{\Phi}\int_0^{T_{\max}} \Phi(T)\left(\frac{dT}{\rho dx}\right)_{c,a} dT = \frac{D_a}{\Phi} \tag{5.4a}$$

and:

$${}_m\overline{S}_b = \frac{\int_0^{T_{\max}} D_b dT}{\int_0^{T_{\max}} \Phi(T) dT} = \frac{\int_0^{T_{\max}} \Phi(T)\left(\frac{dT}{\rho dx}\right)_{c,b} dT}{\int_0^{T_{\max}} \Phi(T) dT} = \frac{1}{\Phi}\int_0^{T_{\max}} \Phi(T)\left(\frac{dT}{\rho dx}\right)_{c,b} dT = \frac{D_b}{\Phi} \tag{5.4b}$$

Most published research deals with perpendicular irradiation across interfaces, with very little study of irradiation where the beam is oriented parallel to the interface. When radiation traveled obliquely across a boundary, we found an immediate buildup of dose after the radiation crossed into the higher density region (Figure 5.26a) (*21*).

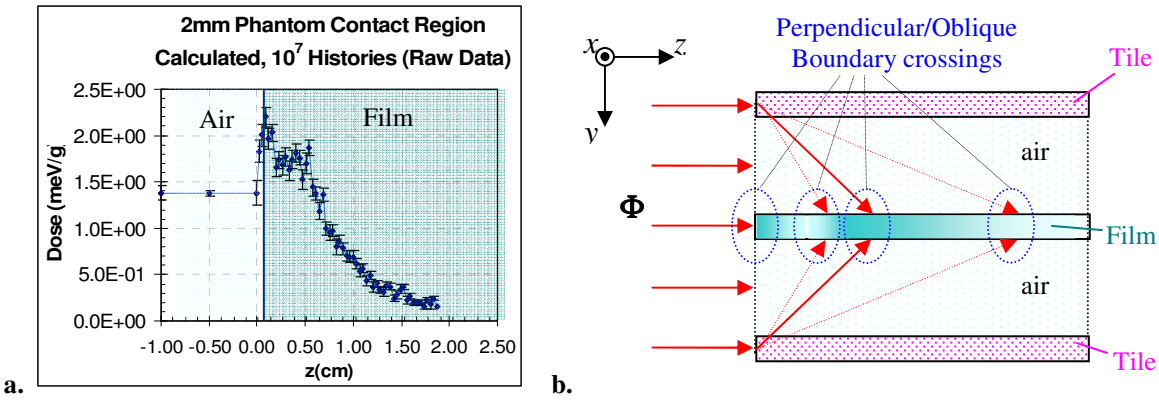

FIGURE 5.26. a. Buildup at boundary crossing (low ρ to high ρ) **b.** Oblique boundary crossing sites due to scattering from tile.

The channel regions are where oblique boundary crossings will primarily occur. The radiation will be scattered in from the tiles, particularly from the leading edges (Figure 5.26.b), For this reason, we also expect more "hot spots" in these areas (as evidenced by channel region plots in Chapter IV)

When radiation travels parallel to the interface, there are situations where the beam may be preferentially scattered from high density media into lower density media particularly in the entrance region. This will be examined in detail in the remainder of this section.

Boundary Effects due to Cavity Conditions

In one respect, the channel region of the phantom can be considered as a "cavity" of film surrounded by gas on either side in *y* (Figure 5.27). The thickness of the film (0.011 cm) is very small relative to the range of the incident electrons (~ 1 m) in the case of transverse irradiation (Figure 5.27a). In this case, the film may be treated as a Bragg-Gray cavity, in which the doses of the two media satisfy equation 5.3 (*22*):

$$\frac{D_{film}}{D_{air}} = \frac{(dT/\rho dx)_{c,film}}{(dT/\rho dx)_{c,air}} = \frac{{}_m\bar{S}_{film}}{{}_m\bar{S}_{air}} = {}_m\bar{S}_{air}^{film} \tag{5.5}$$

In the case of parallel film irradiation (Figure 5.27b), the "width" of the cavity (~2 cm) is larger relative to the electron range, on the order of a few percent. In this case, satisfaction of the Bragg-gray condition becomes weaker, and greater errors in measurement would be expected.

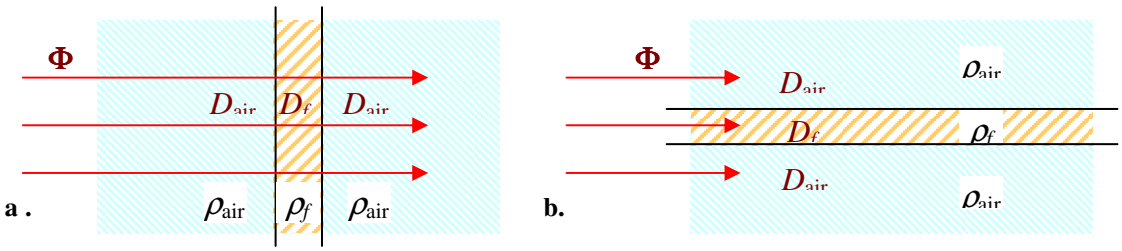

Figure 5.27: Thin layer of film surrounded on either side by air, **a**. Transverse irradiation **b**. Parallel irradiation.

One important point in this case however, is that the film represents the measurement of interest, as opposed to being the proxy to determine the surrounding dose. The film in this case represents a spinach leaf with an air gap on either side. Thus, we are interested in the *effect* of surrounding air on the film dose, not the air dose itself. Therefore, cavity conditions are not expected to contribute to the boundary errors in this case.

Boundary Effects due to Step Size

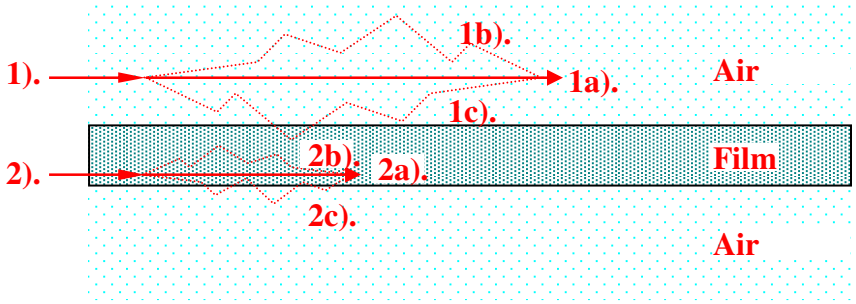

FIGURE 5.28. Possible errors in calculated film dose in the case of irradiation parallel to interface.

For the case of irradiation parallel to the surface of the film there are two possible scenarios leading to under- or over-estimates of the measured dose. Consider two histories depicted in Figure 5.28. Case 1 is an electron moving into the air adjacent to the film. Path 1a is the modeled condensed history step represented by the solid straight arrow. In actuality, the electron may have taken a different path to the same destination. If it follows the upper path 1b, then all energy imparting interactions occur in the same scoring region and the step is accurate. However if it follows the lower path 1c, then some of the energy will be imparted in the film, but will not be scored as such in the calculation. This will lead to an underestimate of the dose in the film. A similar but opposite effect can occur in case 2. In this case, the electron is moving into the film itself. Energy may be imparted outside of the film along path 2c but scored within the film, leading to an overestimate of the measured dose (*23*).

Ideally, the underestimates should balance the overestimates, leading to a reasonably accurate calculation. However differences in relative density of the two media, as well as variations in volume to surface area ratios of each, make the boundary a likely source of calculation errors. Preferential scattering from high to low density media suggest that underestimates should occur in the entrance region of the channel. As the channel size is decreased, the ratio between the surface area of the channel boundary and the volume of the channel is increased. Therefore, the relative amount of scoring (and dose value) errors are expected to be greater in smaller channels.

These errors are less pronounced when the irradiation is perpendicular or oblique with respect to the boundary as the transverse vector component of motion is greater (Figure 5.27a). The particle quickly crosses the boundary and there is less potential for

error. Unfortunately, it is nearly impossible to force all leaves to be arranged with their surfaces perpendicular to the beam. Further, layered vegetables such as onions and scallions have curved surfaces, all but assuring that there will be interfaces parallel to the beam in at least some cases.

Boundary Effects due to Relative Densities

The density of the irradiated material is the major determining factor of stopping power, mean free path, and particle range. On the boundary between two materials of disparate density, irradiated parallel to the boundary, the electrons can travel further along the less dense material and be scattered into the greater density material.

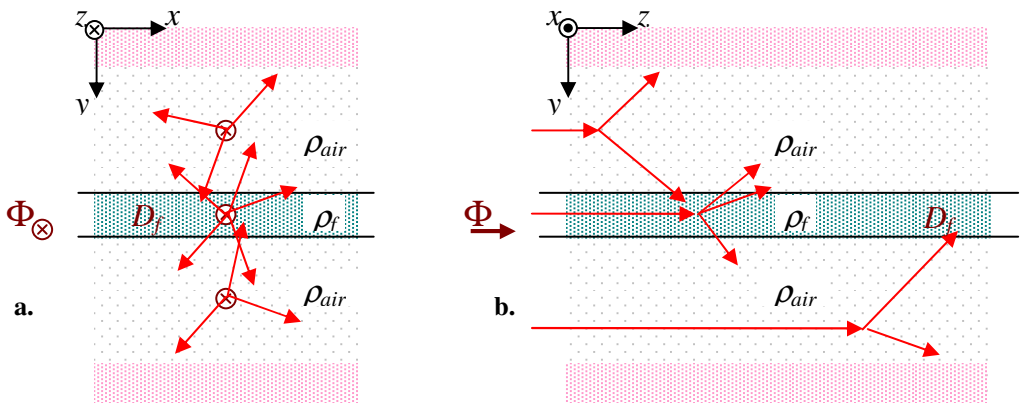

FIGURE 5.29. a. Azimuthal and **b.** polar angle scattering in channel region.

Figure 5.29 shows a film surrounded by air on either side. Due to the lower density of air fewer electrons are scattered laterally into the film as are scattered out of it. However the electrons have a much greater mean free path in air than in the film. Therefore while fewer electrons are scattered into the film at a given depth in z, they are able to travel further and be scattered into the film at a greater depth z. The result is that the dose drops more quickly with z, but remains measurable at greater depths.

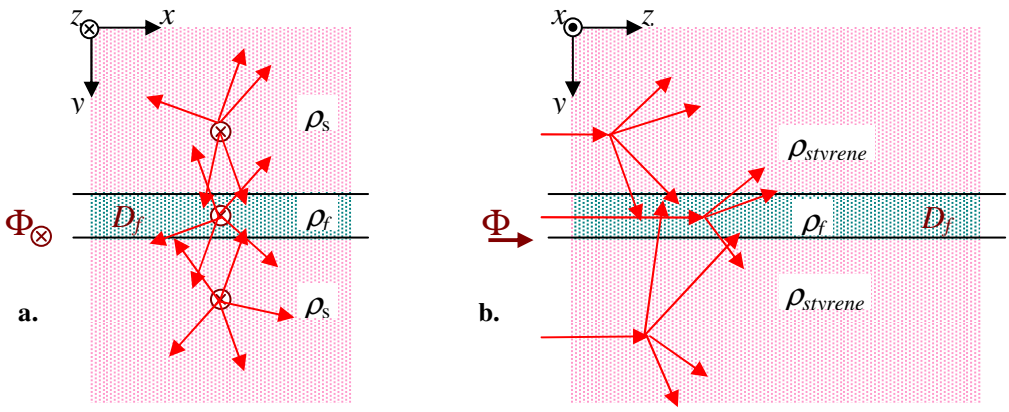

FIGURE 5.30. a. Azimuthal and **b.** polar angle scattering in contact region.

Figure 5.30 shows a film surrounded by styrene on either side. Due to the higher density of styrene more electrons are scattered laterally into the film as were scattered from the film. However the electrons have a much smaller mean free path in styrene than in the air. Therefore while more electrons are scattered into the film at a given depth in *z*, they are not able to travel as far to be scattered into the film as they would be in air.

The transverse thickness of the object plays a large part in determining the amount of build up in the first few millimeters of the phantom Also, how close the region of interest is near the edge of the material will have an effect on the dose further along in the *z* direction.

Thick vs. Thin Slab Attenuation

Figure 5.31 shows dose-depth plots for slabs of three different thicknesses of polystyrene: 0.01 cm, 0.1 cm, and 1.0 cm. The slabs were surrounded on either side by a 1 cm layer of air. The thinnest slab is 0.01 which is approximately equal to the film

thickness. The moderate thickness slab of 0.1 cm is on the order of the two tile thicknesses, which is found in the contact region. The thickest slab is 1.0 cm which is approximately equal to two wall thicknesses of the target holder.

In this section, doses are expressed as a percentage of D_{max}. The dose drops off more quickly for thinner slabs than for thicker ones. This is due to the fact that more electrons are scattered out of the thinner slab than for the thick slab. The dense material on either side of the axis in the thicker slab is more likely to scatter electrons back into the axis than the air surrounding the thinner slab. This is similar to the effect of beam geometry (broad beams vs. narrow beams) as illustrated in Figure 2.2.

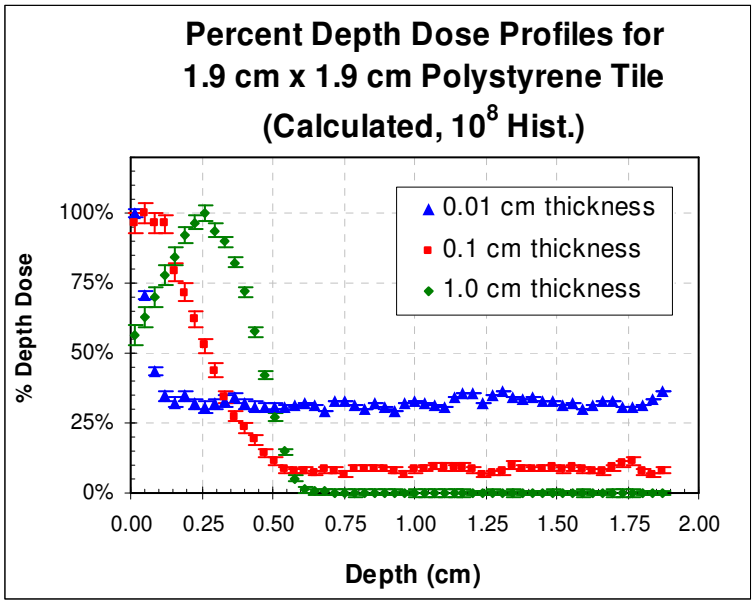

FIGURE 5.31. Depth dose profile polystyrene of varying thicknesses.

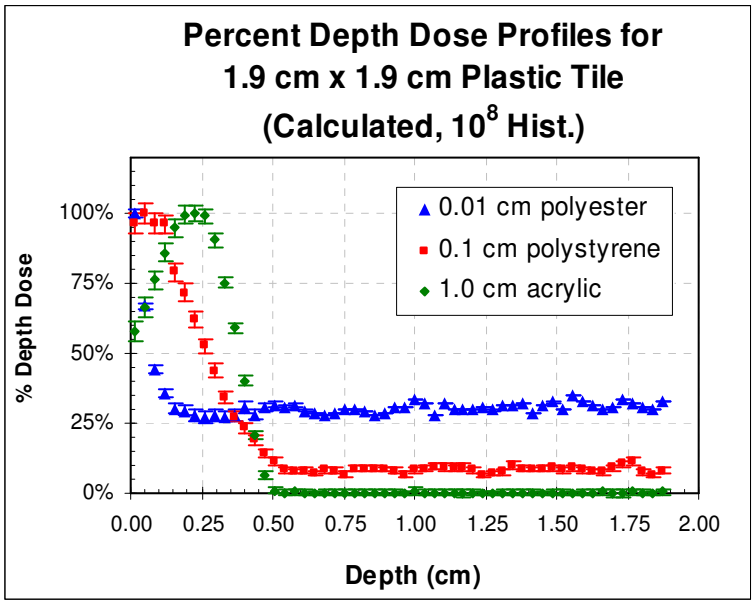

FIGURE 5.32. Depth dose profile for phantom materials and approximate thicknesses.

In actual practice the target consists of three different materials: Polyester (ρ = 1.39 g cm^{-3}), acrylic (ρ = 1.19 g cm^{-3}) as well as Styrene (ρ = 1.06 g cm^{-3}). The polyester comprises the film (0.01 cm thickness), and the acrylic makes up the target holder (2 × ~ 0.5 cm thickness). Figure 5.32 shows the depth dose curves for the three materials and their approximate thickness.

Note that for thinner targets, the dose levels out at a non-zero value. This is due to electrons traveling further in z through the surrounding air and then being scattered into the slab at greater depth. The dose is measured along the center axis of the slab; therefore the thinner slab has less material attenuating the scattered dose. It is not affected by SMAX, as was expected. Figure 5.33 shows depth dose plots for a thin slab for SMAX values of 0.01 cm and 5.90 cm. This is the range of dimensions found within the target system. There was no statistically significant difference between the two curves.

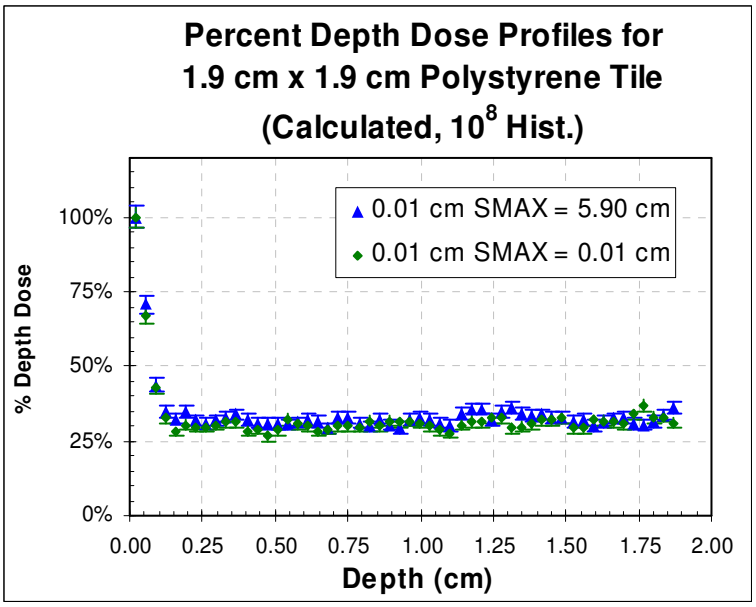

FIGURE 5.33. Effect of SMAX on dept dose distribution for thin slab of polystyrene

Effects of Voxel Proximity to Boundary

The calculated effects of scattering for thin film can also be seen near the edges of thick slabs as well (Figure 5.34). In this case, the "edge" dose was calculated 0.005 cm from the actual edge of the film, so as to stay within the voxels defining the slab. Near the edge of the slab, there is less material to attenuate the electrons scattered into the slab from the air. The resultant curve appears to be a superposition of a thin film attenuation and thick film (Figure 5.35). The thin film calculation is divided by two in this particular case, since the scattered electrons are only entering from one side of the film. However the electrons traveling within the film are not reduced, so this would account for initial drop in the resultant curve which is not seen in this approximation.

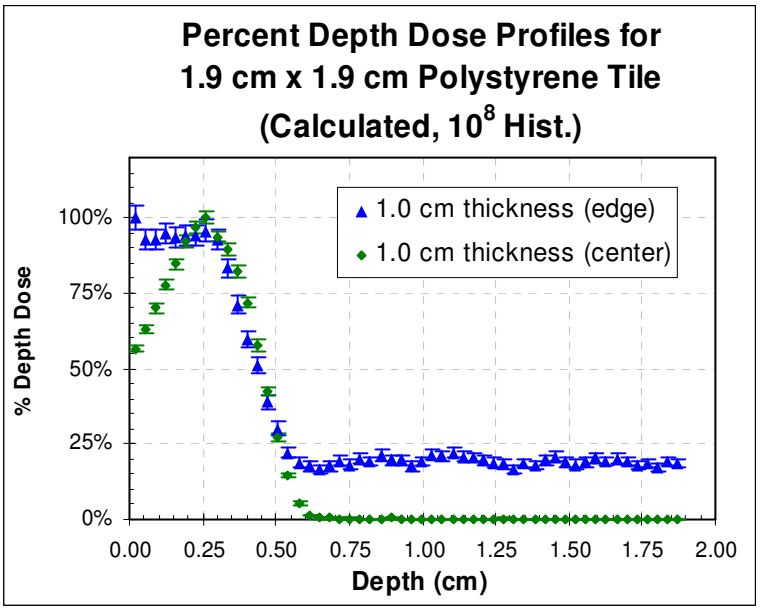

FIGURE 5.34. Depth dose profiles for thick slab of polystyrene

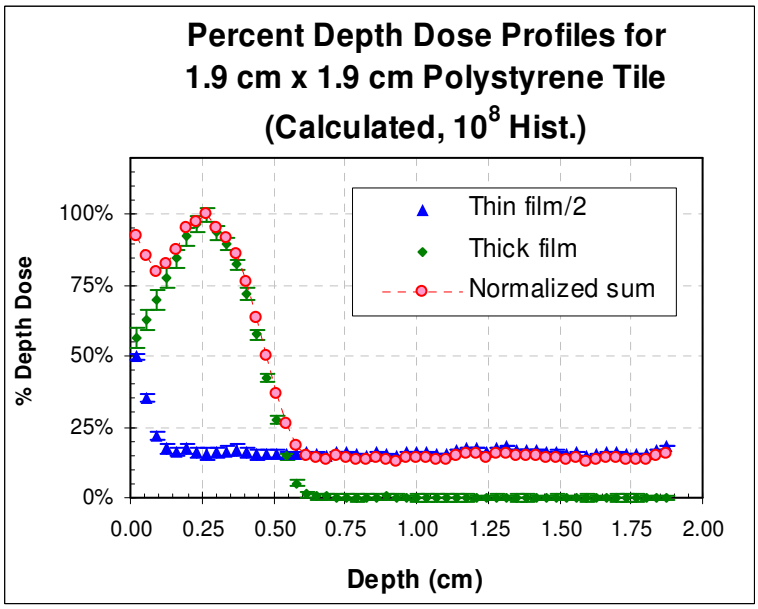

FIGURE 5.35. Estimated depth dose profile components for edge of polystyrene slab

Voxel Width Effects

Due to the film thickness relative to the other phantom dimensions; it is sometimes necessary to reduce the voxel width in one dimension or another in order to accurately

represent the phantom. In particular, the film voxels are thinner in *y* than the voxels used to model the tiles. The film is 0.011 cm in thickness while the tile is 0.0508 cm. To model this exactly, one would need to use voxels 0.0002 cm in width. To represent the phantom and intervening air, this would require:

$$N_v = \left(\frac{5.9\,\text{cm}}{0.002\,\text{cm}}\right)\times\left(\frac{1.9\,\text{cm}}{0.002\,\text{cm}}\right)\times\left(\frac{1.9\,\text{cm}}{0.002\,\text{cm}}\right) = (29500)\times(9500)\times(9500) \qquad (5.6)$$

or 2.66 x 10^{12} voxels, which is beyond the capacity of most Monte Carlo simulation software, and cost prohibitive from a computing standpoint. In our simulation the tiles are modeled with voxels 0.0125 cm in *x* and *y*, and 0.035 cm in *z*. The film is modeled as a 0.011 cm film of polyester which is thinner than the voxels used in the tiles.

Figure 5.36 shows a first approximation, using a 1.0 cm thick slab, made of voxels with cubic widths of 0.025 cm. The region above the slab in y is comprised of 1 cm of air. The dose is calculated in a plane 0.005 cm from the edge in *y*. In the first simulation, the slab is entirely composed of 0.025 cm voxels. In the second simulation, the top layer of voxels in the slab is reduced to 0.01 cm in *y*. The air voxels are 0.025 in width for each case.

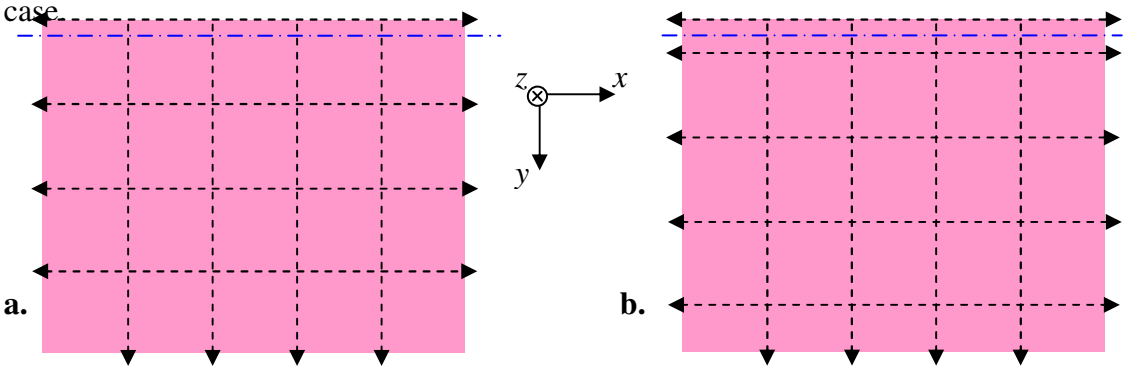

FIGURE 5.36. Solid slab composed of **a.** uniform voxels and **b.** variable width voxels.

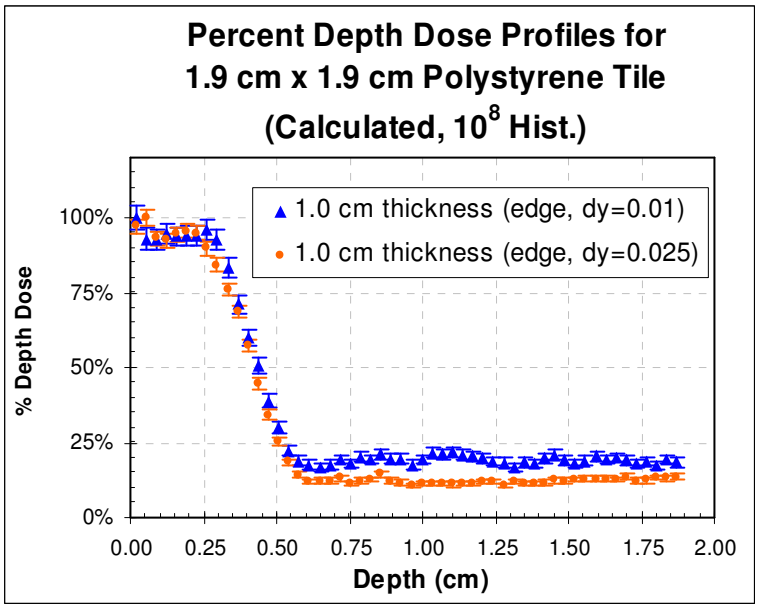

FIGURE 5.37. Effect of voxel width on edge calculations.

Figure 5.37 shows the dose depth plot for the two simulations. There is very little statistically significant deviation, except at the end of the particle range, where the values to not go fully to zero. The fact that the thicker voxels settle to a lower dose value than the thinner voxels is an averaging effect. The dose value per voxel is average value over the volume of the voxel, and plotted at the midpoint of the voxel in each dimension (Figure 5.38).

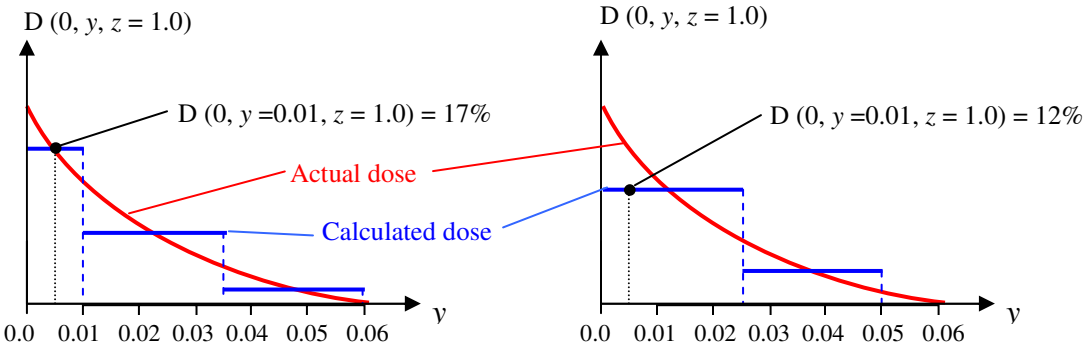

FIGURE 5.38. Voxel width and the effects of binning and averaging on dose distribution.

In practice the film was modeled as three layers, a base layer of polyester 0.009 cm thick, the active layer, which is 0.001 cm thick, covered by a top layer of polyester 0.001 cm thick (see Figure 2.10). The dose was calculated 0.015 cm from the top of the film (mid active layer)

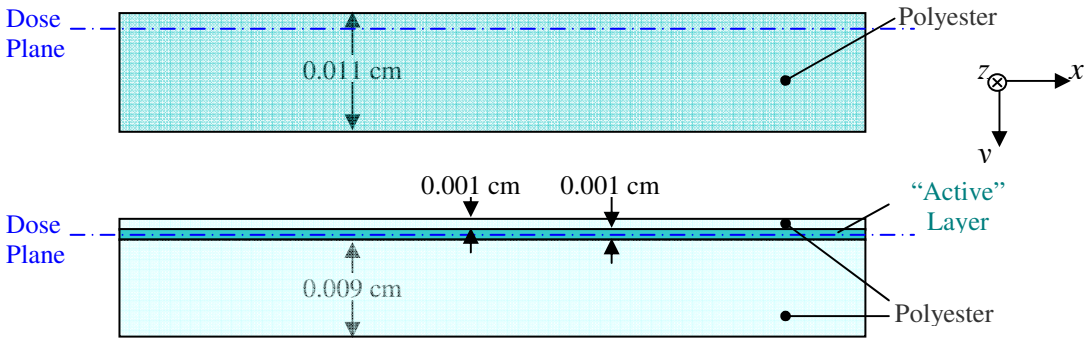

FIGURE 5.39. Representation of radiochromic film in phantom: "simple" (upper) and actual "complex" (lower).

To determine if the variation of voxel widths affected calculation accuracy, two versions of the film were modeled (Figure 5.39). One was a "simple" sheet of polyester consisting of a single layer of voxels 0.011 thick in *y*. The second was a "complex" version made up of three layers of voxels of widths 0.009 cm, 0.001 cm, and 0.001 cm in *y* respectively. This represented the base and cover layers, as well as the active layer, separately. In both cases the dose was calculated 0.015 cm from the top of the film.

Figure 5.40 shows the depth dose plot for each version of the film. There does not appear to be any statistically significant difference, as the vast majority of the error bars overlap. Figure 5.41 shows the calculation repeated with polystyrene replacing the air, with similar results.

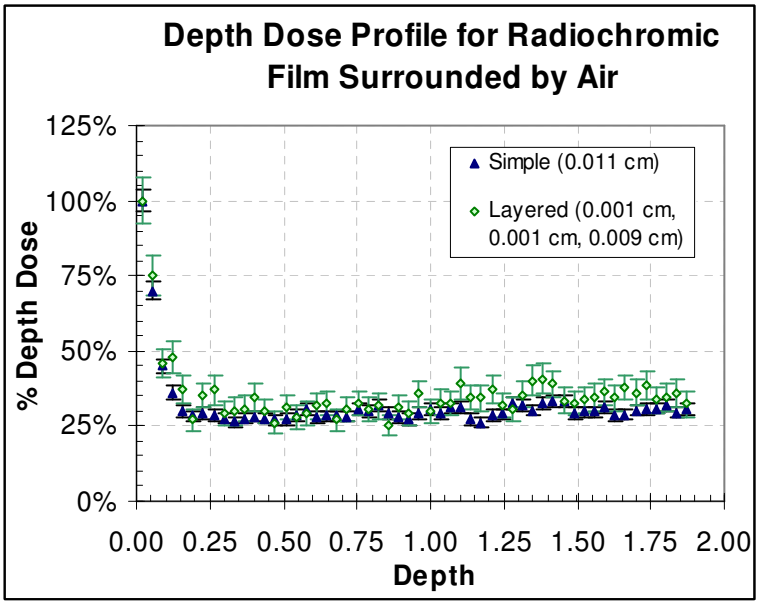

FIGURE 5.40. Depth dose plot for "simple" vs. "complex" film model (in air)

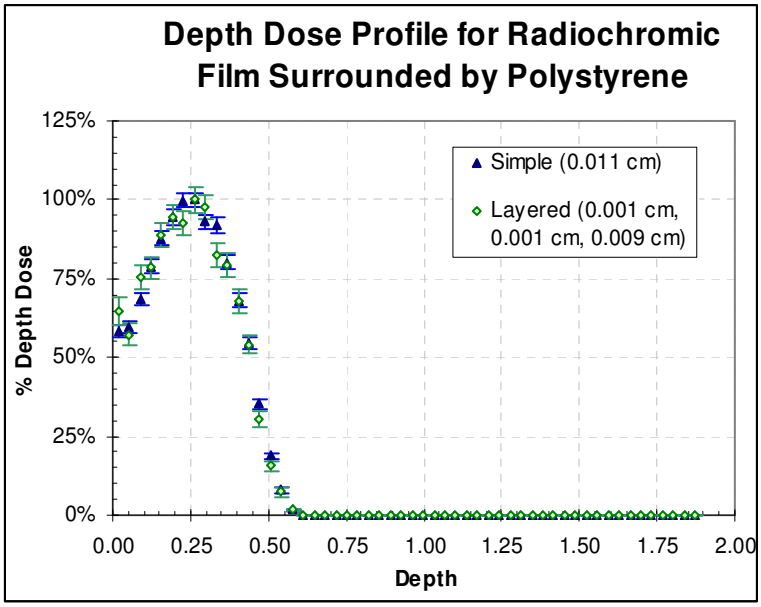

FIGURE 5.41. Depth dose plot for "simple" vs. "complex" film model (in polystyrene)

Film Asymmetry

Since the radiochromic film is not symmetrical from one side to the other, its response can be expected to vary depending upon which direction the active layer is facing. This

would be of no significance in large homogeneous media. However in our study, the phantom components are of similar dimensions as the film thickness, so the difference can be expected to be statistically significant.

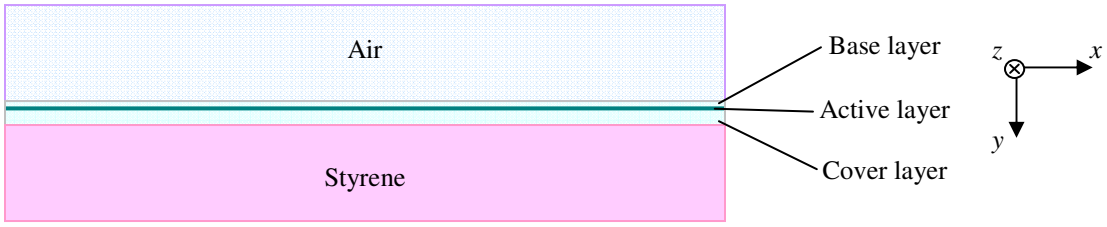

FIGURE 5.42. Radiochromic film in contact with styrene. Active layer facing away from polystyrene.

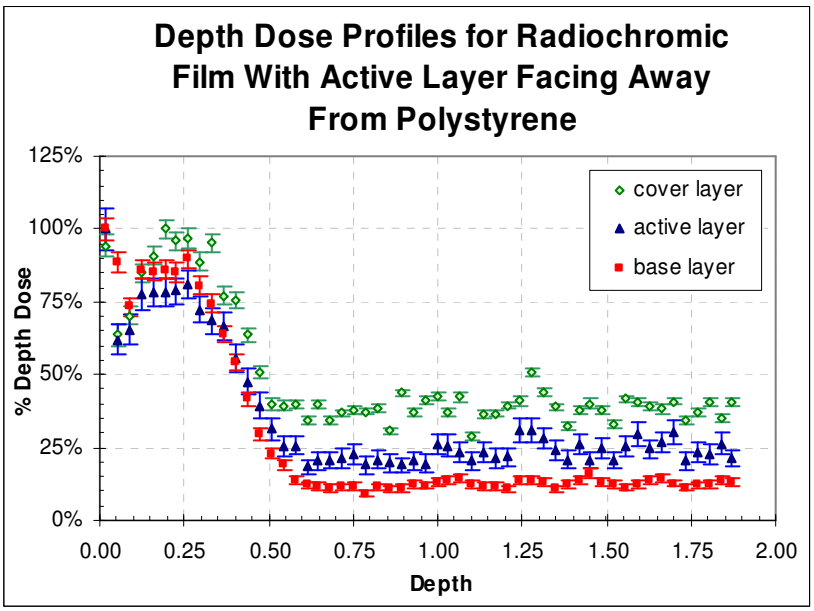

FIGURE 5.43. Depth dose profiles by film layer, Active layer facing away from polystyrene.

Figure 5.42 shows a sheet of radiochromic film placed on top of a 1 cm slab of styrene in air. Irradiation is parallel to the surface of the film. The active layer is facing away from the styrene, and base layer is in contact with it. Figure 5.43 is a calculated depth dose plot for each of the layers of the film. As expected, the highest dose occurs in the cover layer over most of the depth. In the first 0.25 cm the dose to the base layer is

greater than the active layer, and in the first 0.1 cm it is greater than the cover layer as well. This is due to greater scattering from the less dense air at greater depth, and greater scattering from the denser styrene at lesser depth.

Figure 5.44 shows a sheet of radiochromic film placed on top of a 1 cm slab of styrene in air. The active layer is facing toward the styrene, and cover layer is in contact with it. As before, the irradiation is parallel to the surface of the film. Figure 5.45 is a calculated depth dose plot for each of the layers of the film. As expected, the highest dose occurs in the base layer at large depth.

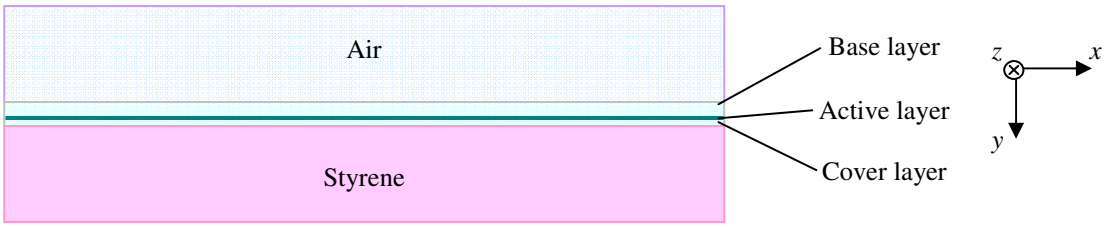

FIGURE 5.44. Radiochromic film in contact with polystyrene. Active layer towards polystyrene.

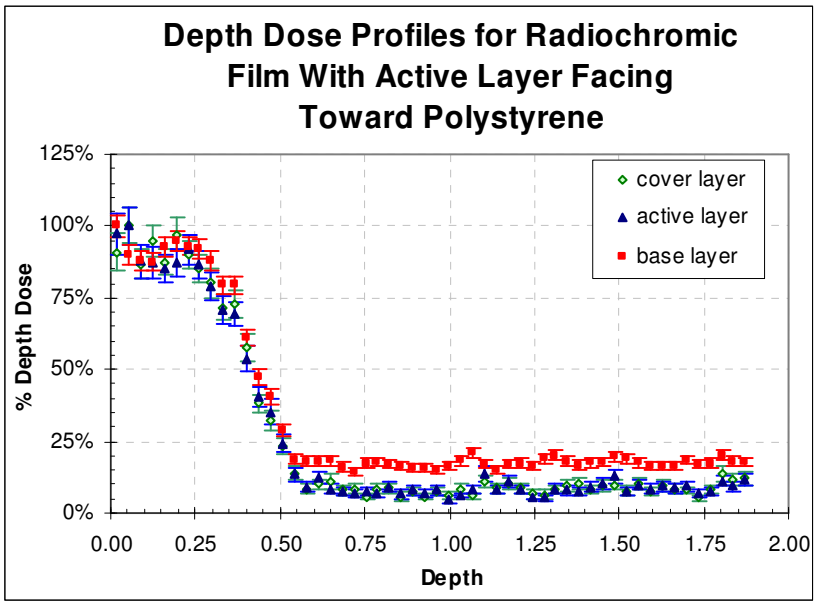

FIGURE 5.45. Depth Dose profiles by film layer, Active layer towards polystyrene.

Since the active layer is the *de facto* layer of interest when it comes to measured dose (it is the only calculation that can be verified), the effect of film orientation on the active layer is of primary interest. The dose is roughly equal (within error bars) for depth between 0.25 and 0.50 cm. For depths less than 0.25 cm, the film with the active layer facing the styrene has the higher dose (Figure 5.46). This is expected, as greater scattering occurs from they styrene at lesser depths, and the polyester base layer provides more shielding than the thinner cover layer. For depths greater than 0.50 cm, the film with the active layer facing away from the styrene has the higher dose. This is also expected as greater scattering occurs from they air at greater depths, and the polyester base layer provides more shielding than the thinner cover layer.

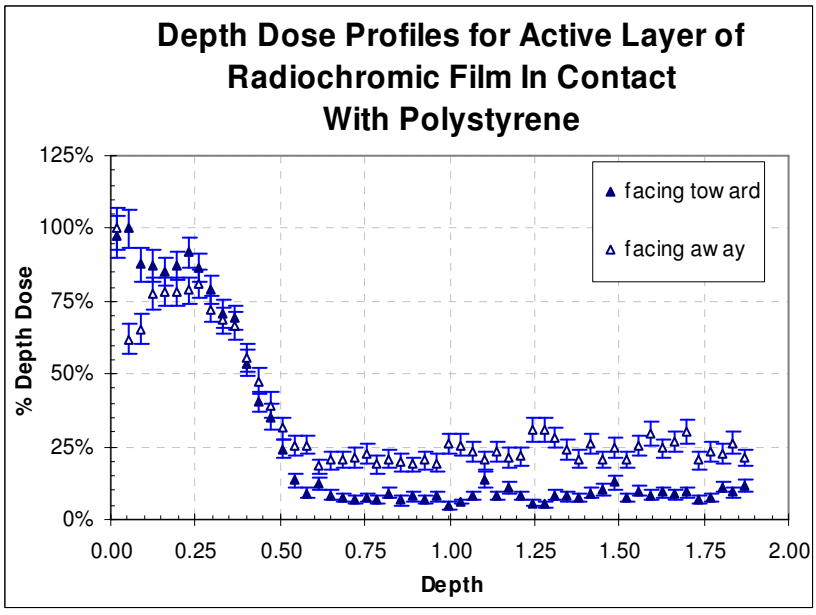

FIGURE 5.46. Depth dose profiles in the active layer of film.

5.2.2 Variation of Major Monte-Carlo Parameters

In this section, the effects of varying the three main parameters used in the condensed history approach to Monte-Carlo calculation are examined. Of the these parameters, SMAX should have most effect on calculation accuracy, while ECUT should the least[24]

In actual practice variation of SMAX and ESTEPE produced very little variation in the calculated values, while only ECUT produced noticeable variations.

SMAX

If, during the course of a history, a particle is allowed to make a step size significantly larger than the dimension of the phantom structure, an error in scoring can occur. It was hoped that by going to sufficiently small values of SMAX, the calculation errors incurred in the channel region would be eliminated or at least greatly reduced. Unfortunately this was not the case for any of the phantoms used in this study. Results for the 2mm phantom are shown in Figures 5.47, 5.48, and 5.49. SMAX is varied from 0.001 cm (the thickness of the active layer of the film), to the default value of 5 cm (2.5x the maximum dimension of the phantom).

Ten million (10^7) histories were modeled. In every case, the error bars overlapped, meaning that the only variation was statistical (as when the random number generator seed is reset to a new value for a new calculation). This was the most unexpected result of the study. This was the area where we expected the possible errors described section 5.2.1 to be reduced or exacerbated by varying SMAX. They were not.

Results for the 5.5 mm phantom were similar, and are not shown here. They can be seen in appendix C.

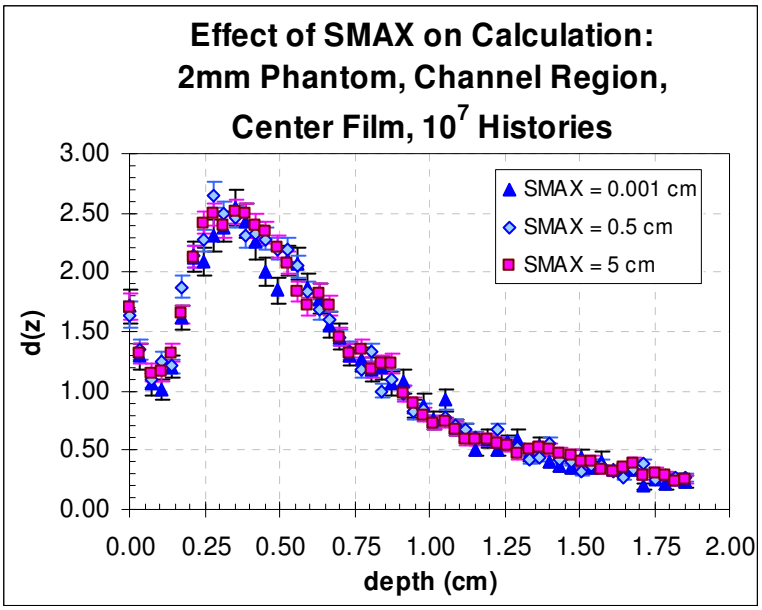

FIGURE 5.47. Effect of SMAX on dose in channel region of 2 mm phantom.

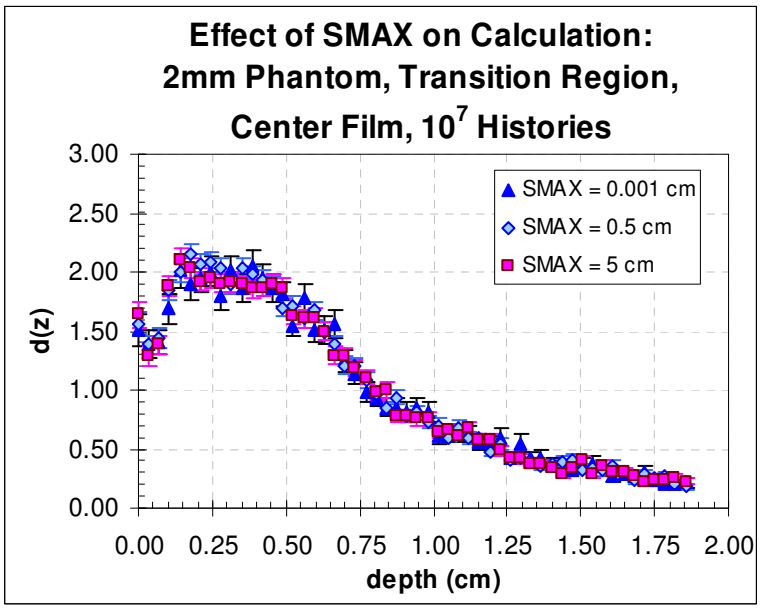

FIGURE 5.48. Effect of SMAX on dose in transition region of 2 mm phantom.

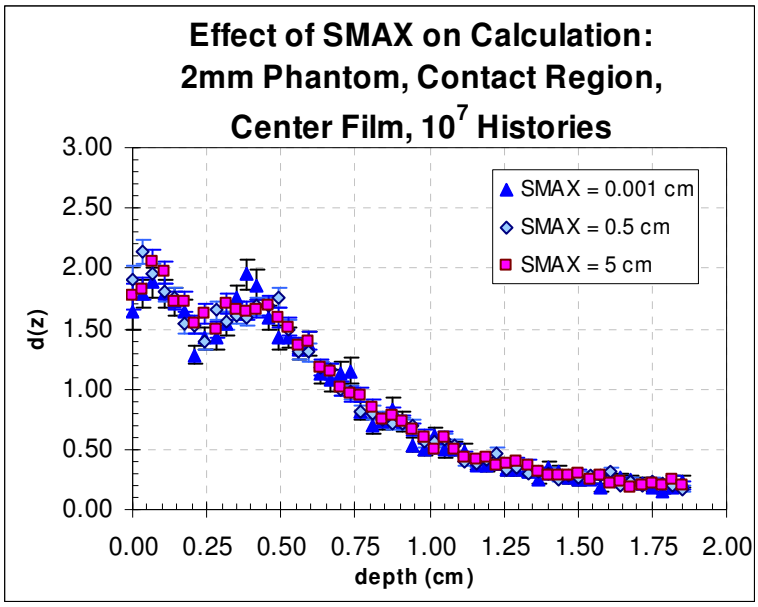

FIGURE 5.49. Effect of SMAX on dose in contact region of 2 mm phantom.

ESTEPE

The default value for ESTEPE is 25% of the incident energy. In actuality, the energy loss per individual interaction is much smaller, but many interactions may be condensed which creates a greater fractional energy loss per step. The greater the maximum allowed fractional energy loss allowed in a single step (definition of ESTEPE), the more interactions are condensed into that step. Reducing the value of ESTEPE reduces the number of interactions per step.

Figures 5.50, 5.51, and 5.52 show the calculation results for the 2mm phantom with ESTEPE ranging from 0.1% to 50%. No statistically significant variation was observed for any of the phantoms.

(See Appendix C for 5.5 mm phantom results)

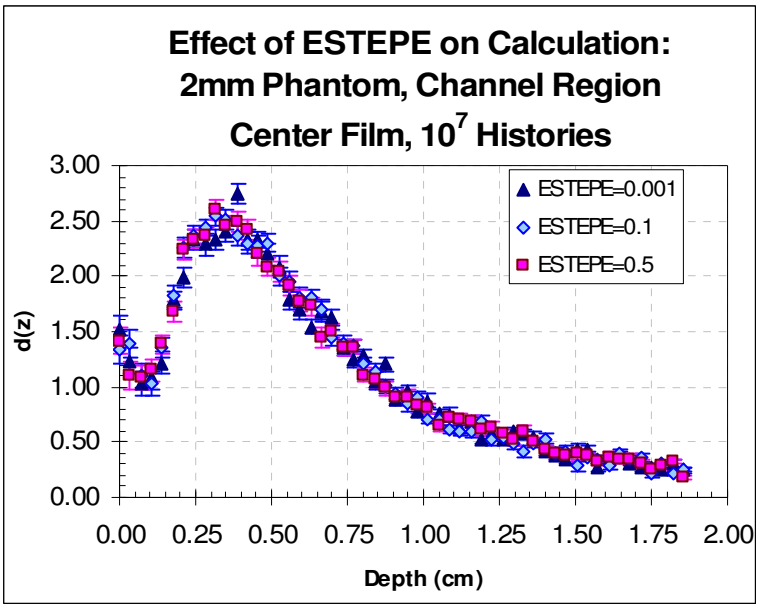

FIGURE 5.50. Effect of ESTEPE on dose in channel region of 2 mm phantom.

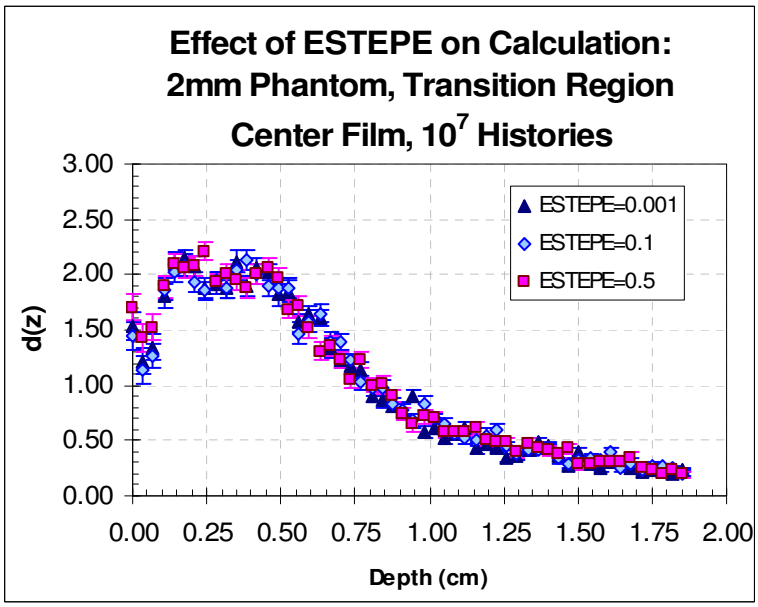

FIGURE 5.51. Effect of ESTEPE on dose in transition region of 2 mm phantom.

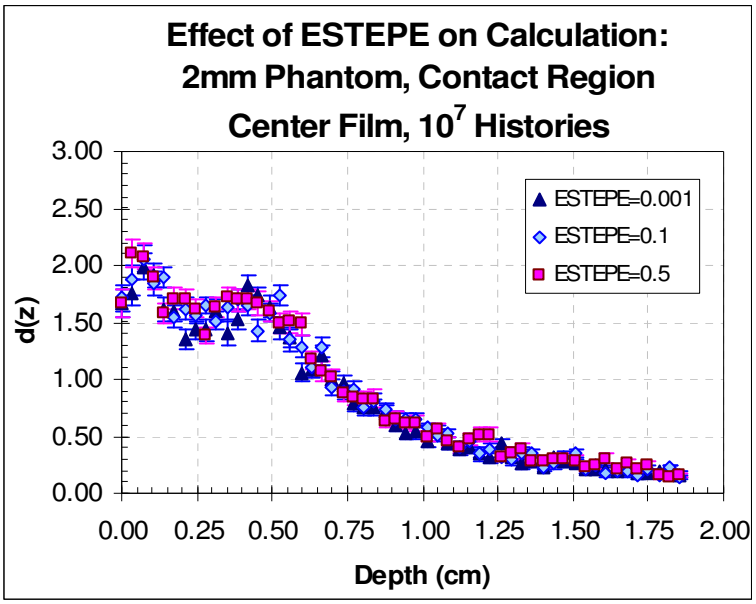

FIGURE 5.52. Effect of ESTEPE on dose in contact region of 2 mm phantom.

(See Appendix C for 5.5 mm phantom results)

ECUT

ECUT is typically chosen so that the electron CSDA range (Figures 5.53 and 5.54) for that value is equal to the smallest structural dimension of the phantom. In this case, it is the thickness of the film at approximately 0.011 cm. This corresponds to an electron energy of ~0.02 MeV. The tile thickness of 0.051 cm corresponds to an electron energy of ~0.11 MeV. There is no discernable difference between calculations for ECUT = 0.11 and ECUT = 0.02, or any calculations for values of ECUT below 0.11.

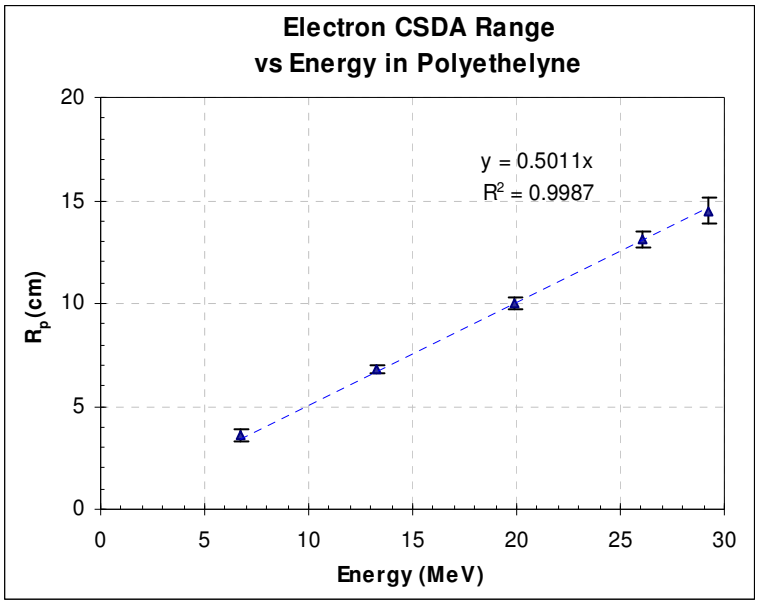

FIGURE 5.53. Electron ranges for Polyethylene (*25*).

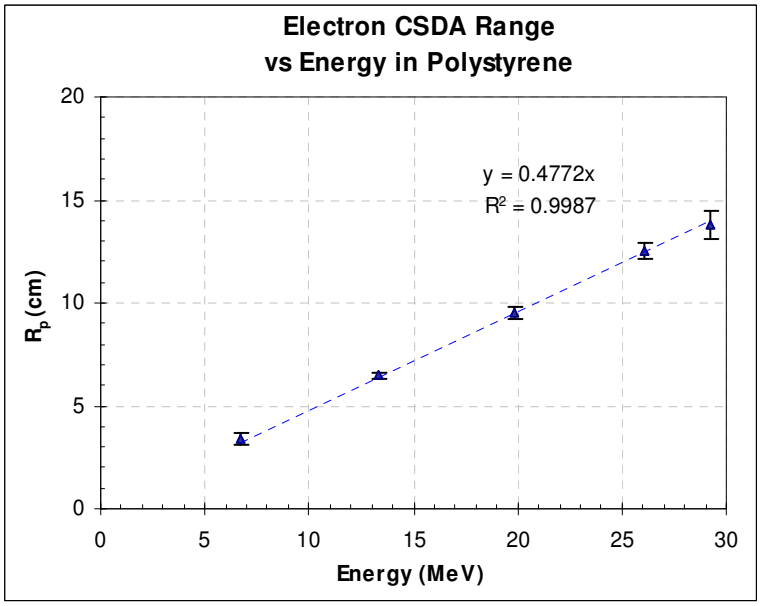

FIGURE 5.54. Electron ranges for Polystyrene (26).

The value for ECUT was increased to 0.67 MeV, which is half of the incident radiation value. This is the only case where statistical noise was noticeable in the isodose distribution (Figure 5.55).

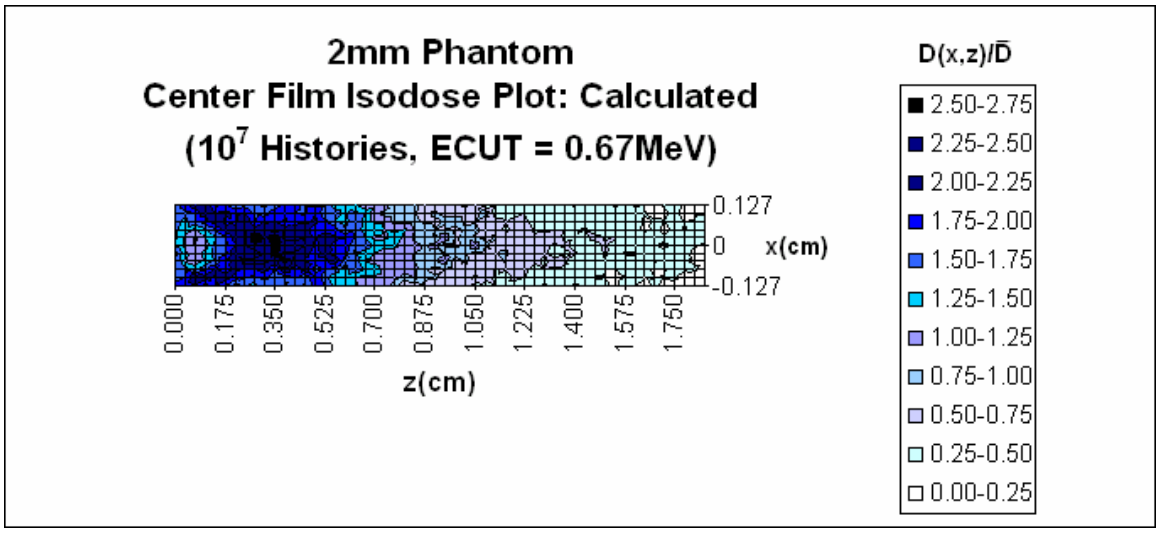

FIGURE 5.55. Isodose distribution for 2mm phantom, showing statistical noise due to ECUT.

Figures 5.56, 5.57, and 5.58 show the depth dose curves for the channel, transition and contact regions for the 2 mm pitch phantom. The depth dose curves are similar for ECUT values of 0.11 and 0.67 with only statistical noise in evidence for higher values of ECUT.

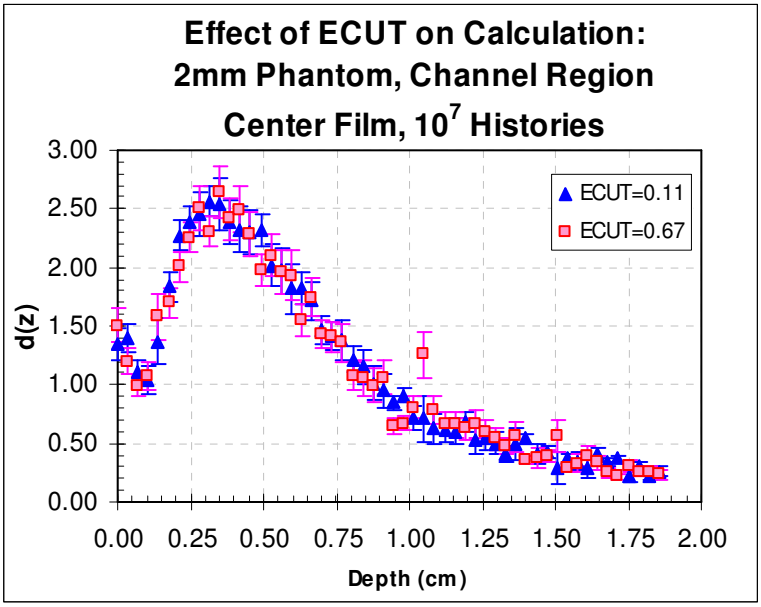

FIGURE 5.56. Effect of ECUT on dose in channel region of 2 mm phantom.

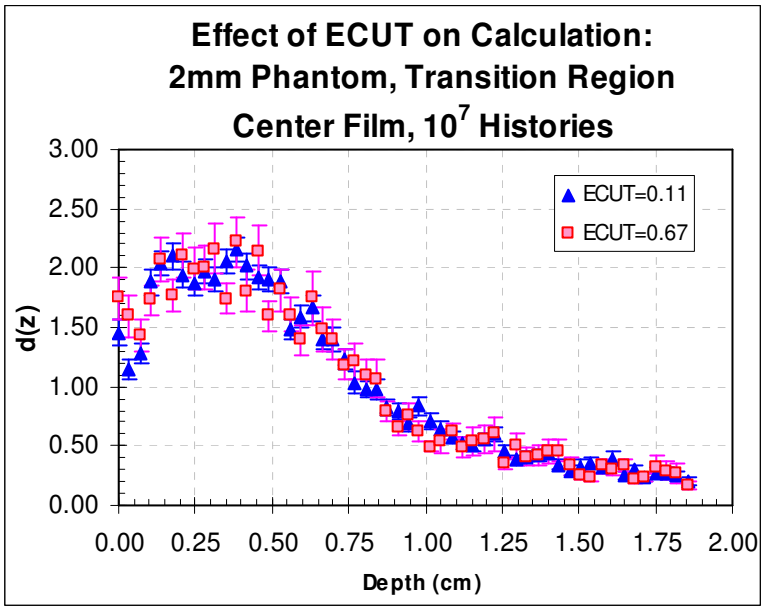

FIGURE 5.57. Effect of ECUT on dose in transition region of 2 mm phantom

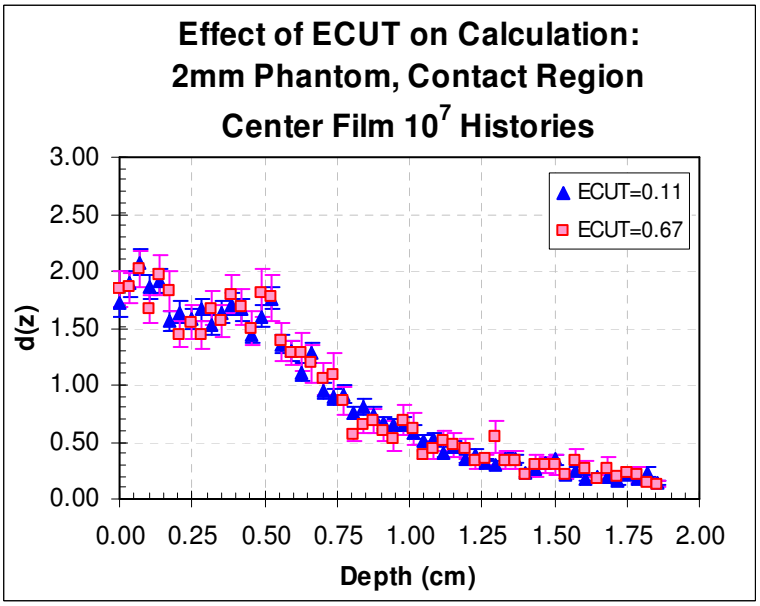

FIGURE 5.58. Effect of ECUT on dose in contact region of 2 mm phantom.

(See Appendix C for 5.5 mm phantom results)

In summary, condensing the number of interaction steps did not increase the discrepancies between measurement and calculation. Conversely, increasing the number of interaction steps did not reduce the discrepancies between measurement and calculation.

5.3 Testing of Uncertainty and Dose Uniformity Predictions on Other Target Configurations

There are general trends which were observed, that can be applied to other target configurations. These trends are based on general physics and statistics explored in Section 5.3. However, it was not possible to produce a detailed mathematical model from the data acquired.

Predicted trends from observations:

- Greater errors will occur in smaller channels, as the ratio of channel boundary area to channel volume is increased.

- Dose non-uniformity is expected to also increase with smaller channels due to more oblique boundary crossings per volume as illustrated in figure 5.30a.

- Errors in low density region are reduced when film is on the edge, rather than center of the channel. This is due to the fact that there is a boundary of dissimilar density on only one side of the film vs. both sides.

- The base layer will provide a slightly different amount of "shielding" relative to the cover layer. This will affect the relative contribution from each side of the phantom.

5.3.1 1 mm Phantom

The smallest pitch corrugation is in the 1mm phantom. In this phantom, the ratio of channel boundary area to channel volume is greatest. Due to potential step artifacts described in section 5.2 we expect the greatest calculation errors here. It is worth noting in this case the actual pitch was not 1 mm due to the manufacturing process (it was actually 1.75 mm, nearly double the expected width in x of 1mm). However,the aforementioned area/volume ratio which which is of interest, so it was satisfactory for use. The ratios are shown in table 5.2.

TABLE 5.2
Channel boundary area to channel volume ratios for various corrugations (approximate)

Phantom	Channel boundary area	Channel volume	Ratio
1.0 mm	0.5249 cm^2	0.0082 cm^3	64.42 cm^{-1}
2.0 mm	0.7953 cm^2	0.0186 cm^3	42.72 cm^{-1}
5.5 mm	1.8974 cm^2	0.1149 cm^3	16.52 cm^{-1}

The 1mm phantom is shown in Figure 5.59. The voxel map was constructed with five folds, as with the "normal" tile phantom of Figure 3.10. This the phantom design is the one that comes closest to having a homogeneous structure, as well as having the highest film/air gap width, So in addition to greater discrepancies in the channel region, it should have the least discrepancies in the contact region The film image and region of interest are shown in Figure 5.60.

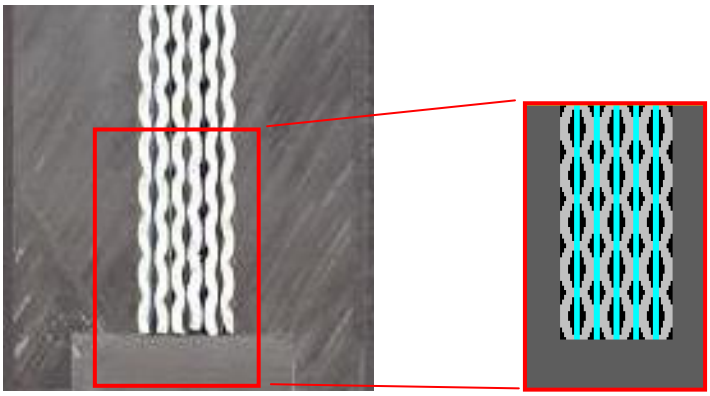

FIGURE 5.59. 1mm phantom and voxel map.

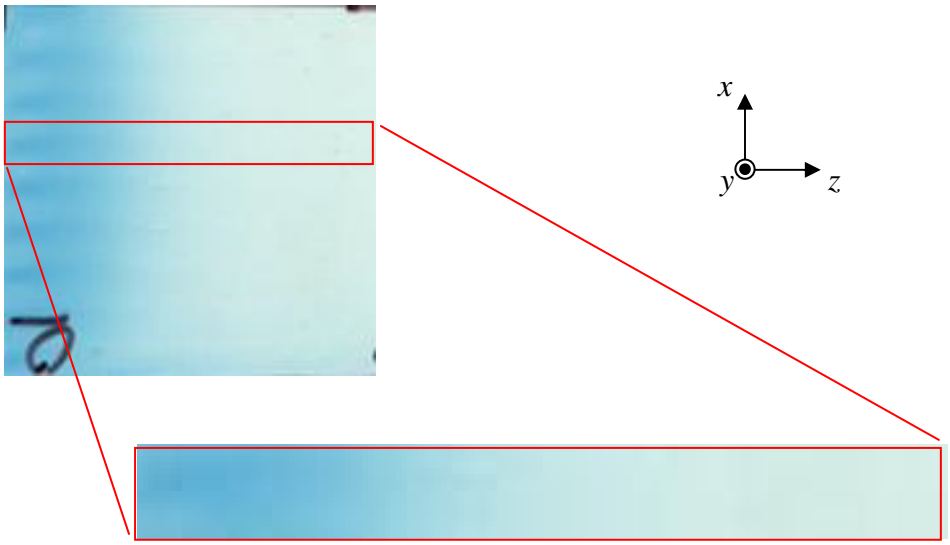

FIGURE 5.60. Film image and region of interest for 1mm phantom shown in Figure 5.59.

Figures 5.61 and 5.62 show the calculated and measured dose distributions for the 1 mm phantom of Figure 5.59. By visual inspection two things are readily apparent. One, the plots show the most discrepancy between calculated and measured dose distributions. Two, the dose is much more non-uniform than in other phantoms

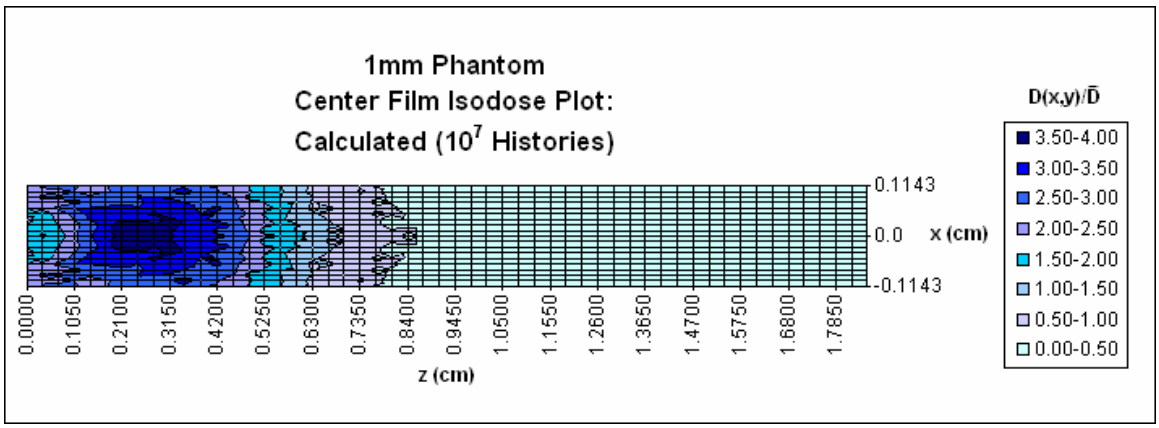

FIGURE 5.61. Calculated isodose distribution for 1mm phantom of Figure 5.59.

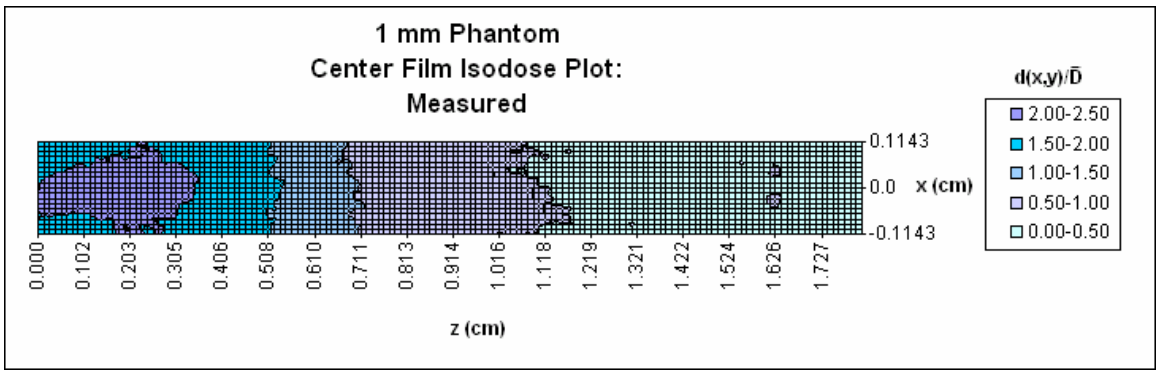

FIGURE 5.62. Measured isodose distribution for 1mm phantom of Figure 5.59.

The calculation overestimates the measured dose between z = 0.12 cm and z = 0.65 cm in the channel region, and for z > 0.65 cm for the transition and contact regions. Beyond that it underestimates the measured dose in all cases. (Figures 5.63, 5.64 and 5.65)

Figure 5.66 is a summary plot of the differences. The measured values are subtracted from calculated values, so positive values represent overestimates by the calculation relative to the measured dose. The maximum overestimate occurs at $z \sim 0.35$ cm in all cases and ranges from 60% in the contact region to 75% in the channel region. The increasing underestimate beyond $z = 0.65$ cm is due to the fact that the calculated dose approaches zero while the measured dose does not. It would appear that more electrons

and photons are making it down the channels than are being modeled by the calculation. This is not a step size artifact. If it were the case, then the effect would be reversed. More electrons would make it down the channel in the calculation than in the measurement.

If we consider the 5.5 mm phantom to represent loosely packed leaves and the 1mm phantom to represent more densely packed leaves, then the dosimetry is becomes less accurate as packing density increases.

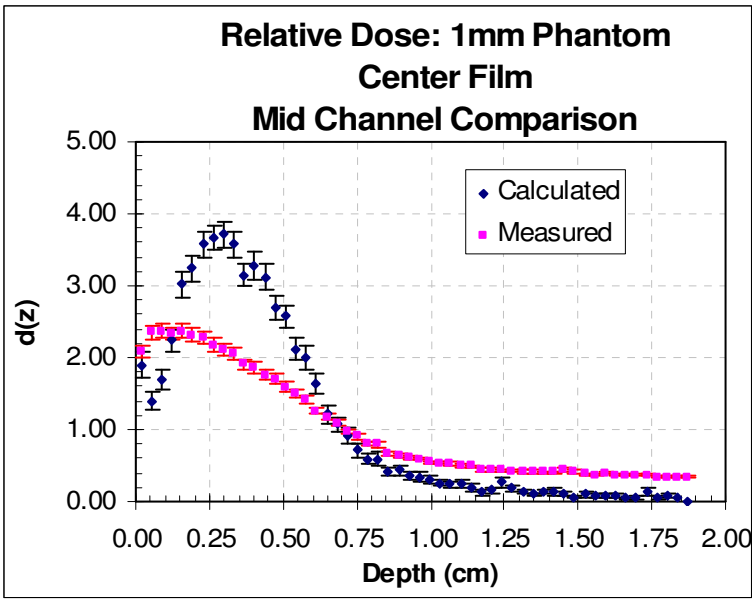

FIGURE 5.63. Channel region comparison for 1mm phantom.

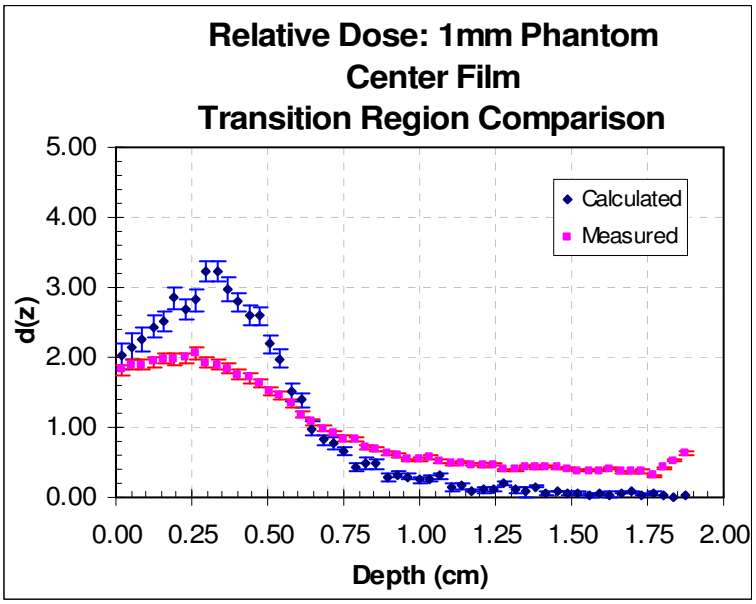

FIGURE 5.64. Transition region comparison for 1mm phantom.

Another serious issue is that of dose uniformity. The 1 mm phantom shows $D_{max}/\overline{D}$ ratios exceeding a factor of two, even in the contact regions. It reaches 2.37 in the channel. By contrast, $D_{max}/\overline{D}$ is only 1.66 in the 5.5mm phantom and 2.12 in the 2mm phantom. This agrees with the prediction that dose uniformity will decrease with smaller channels (for $z < \mathcal{R}$).

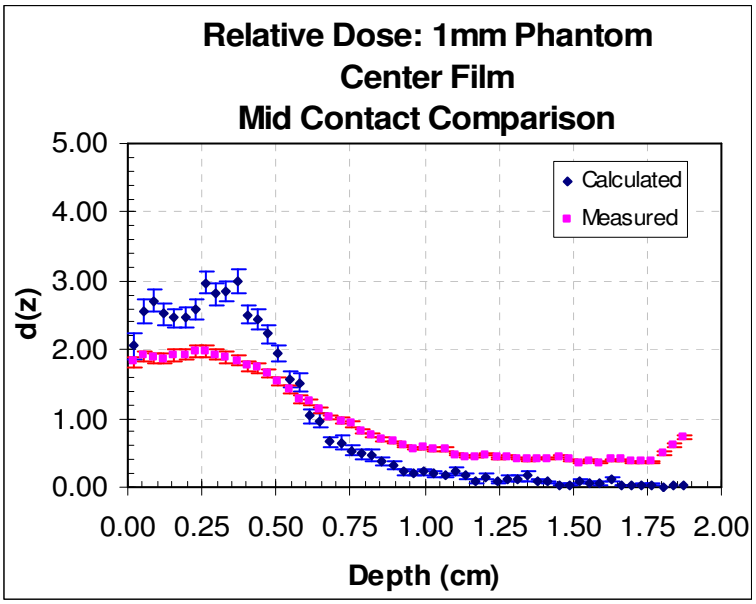

FIGURE 5.65. Contact region comparison for 1mm phantom.

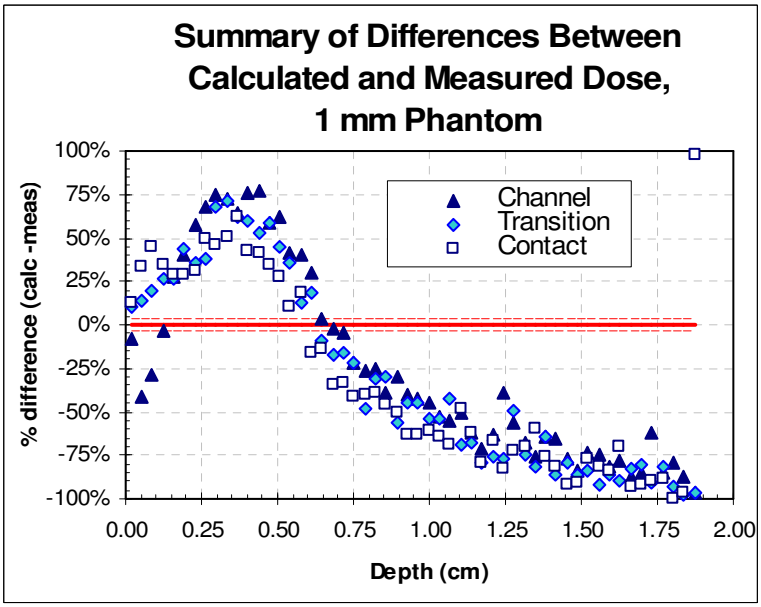

FIGURE 5.66. Summary of differences between calculated and measured values, 1 mm phantom.

5.3.2 Staggered Tile Phantom

Given the fact that the greatest errors so far have occurred where the film is in contact with an air gap on both sides, it is reasonable to assume that there will be smaller errors if the air gap is only on one side. To this end, a modified phantom was created in which the tiles were oriented all facing the same way. In this configuration the tiles were said to be "staggered", as the channel region on one side of the film coincided with the contact region on the other side

2 mm Staggered Tile Phantom

The 2mm staggered tile phantom is shown in Figure 5.67. The voxel map was constructed with four folds, as with the "normal" tile phantom of Figure 3.10. For clarity, two folds of the phantom were examined. The blue arrow indicates the point of comparison where the base layer of film comes in contact with the film (active layer facing air) immediately above the midpoint in the negative *x* direction. The midpoint of the region of interest is where the "active layer" side if the film comes into contact with the film and is where the other comparison was made (green arrow).

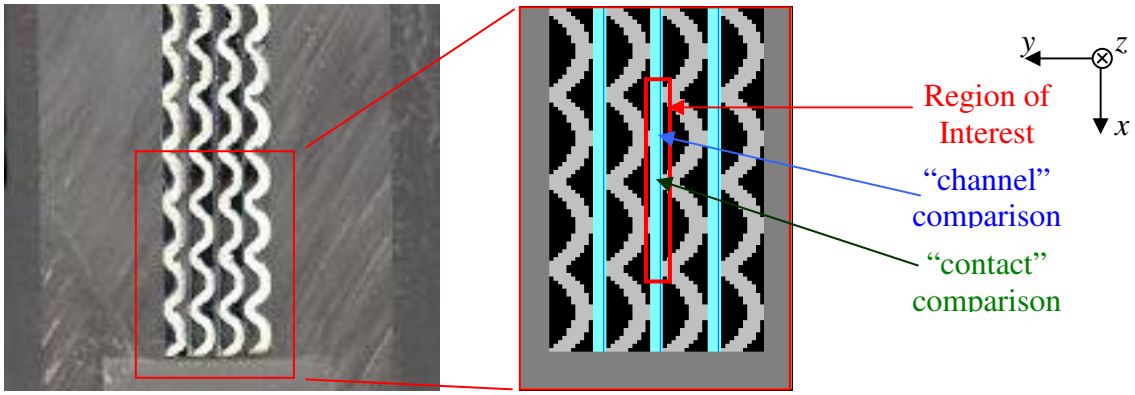

FIGURE 5.67. 2 mm "staggered" tile phantom and voxel map.

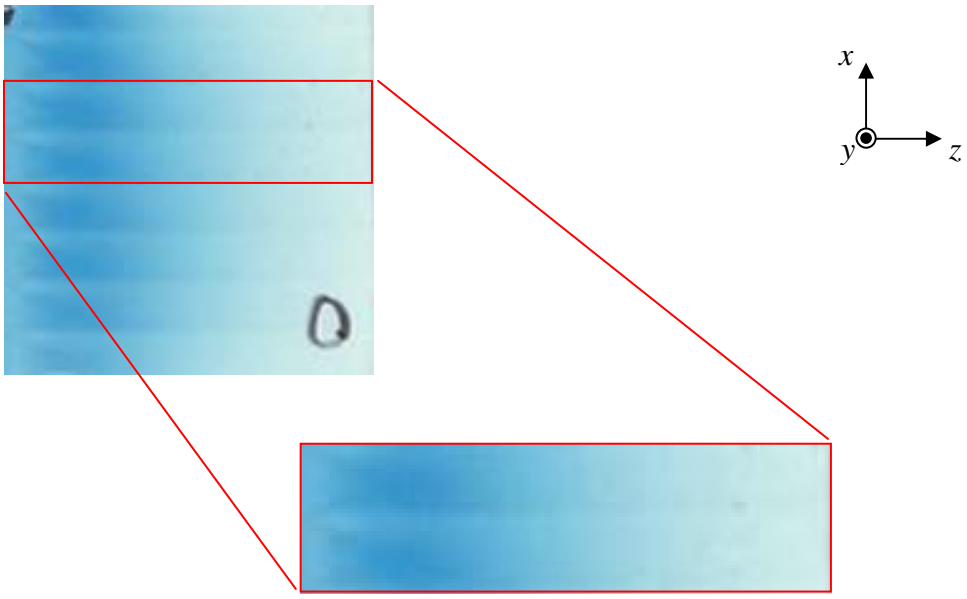

FIGURE 5.68. Film image and region of interest for phantom shown in Figure 5.67

Figure 5.68 shows the image of the radiochromic film and the associated region of interest. Figures 5.69 and 5.70 show the calculated and measured isodose distributions for the staggered tile phantom of Figure 5.67. The asymmetry from one section of the film to the other is due to scattering from the bottom of the film holder which is only one fold away from the region of interest (x is positive in the downward direction). By visual inspection it is apparent that the isodose distributions are more similar (between measurement and calculation) than those for the "normally" arranged tiles.

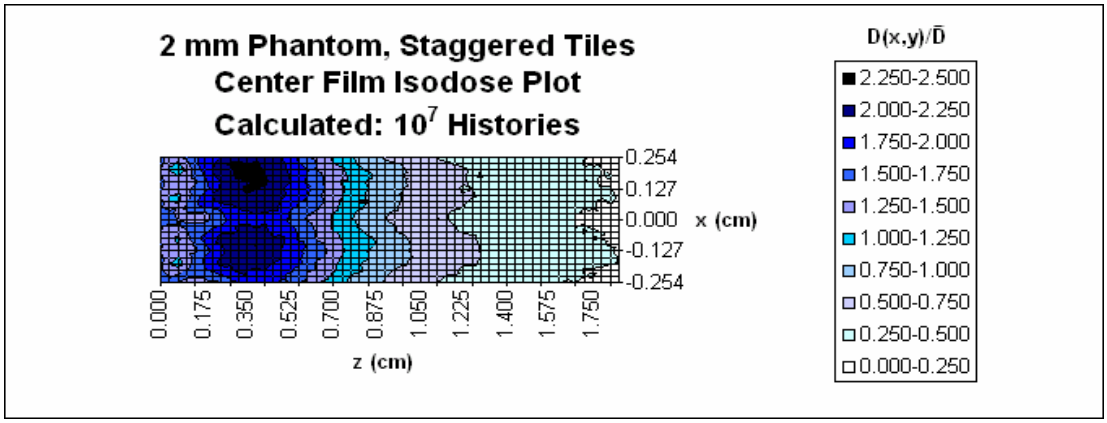

FIGURE 5.69. Calculated isodose distribution for staggered tile phantom of Figure 5.67

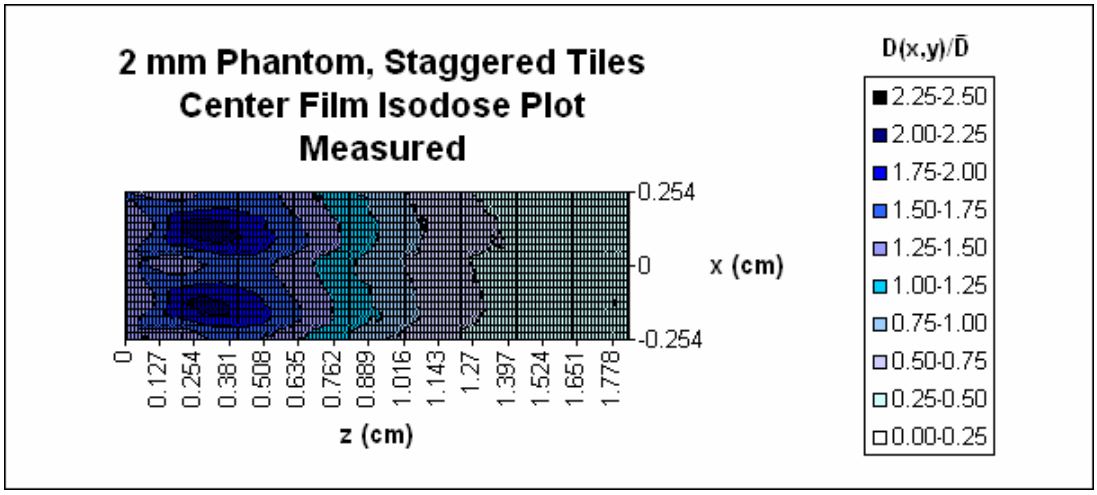

FIGURE 5.70. Measured isodose distribution for staggered tile phantom of Figure 5.67

Figures 5.71 and 5.72 are depth dose distributions which bear out the observation. Figure 5.71 is the depth dose curve for where the base layer is facing the point of contact, and the active layer is facing the channel. The dose uniformity is the same as for the normally oriented tile phantom ($D_{max}/\overline{D} \cong 2.12$ for both) but the errors are much smaller. Figure 5.72 is the depth dose curve for where the active layer is facing the point of contact, and the base layer is facing the channel. The differences between measured and calculated are greater than those for the normally arranged tiles, (Figures 4.14, 5.52) because in the latter, the styrene is in contact with both sides of the film as opposed to just one.

Figure 5.73 is a summary plot of the differences. The amount of error remains within 25% over the entire range of z, with the exception of the last 2mm, which is due to a blemish on the film

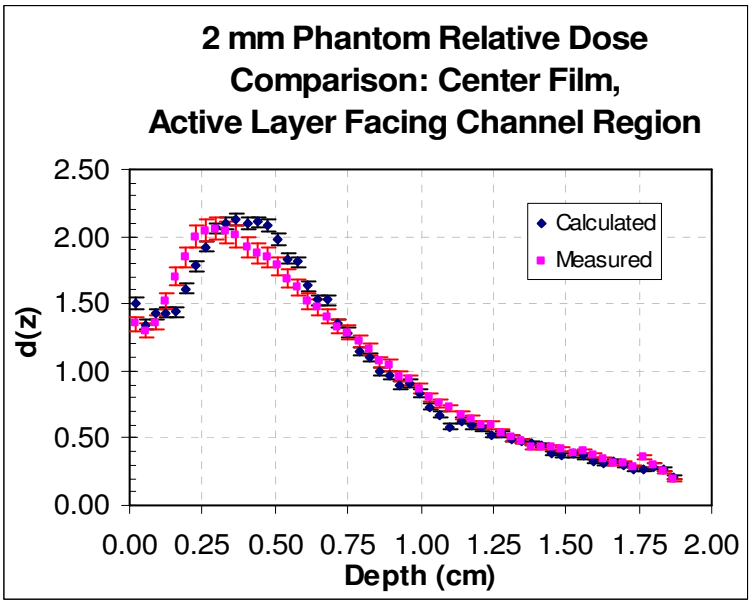

FIGURE 5.71. 2 mm phantom depth dose plot for base layer in contact with styrene, active layer facing air.

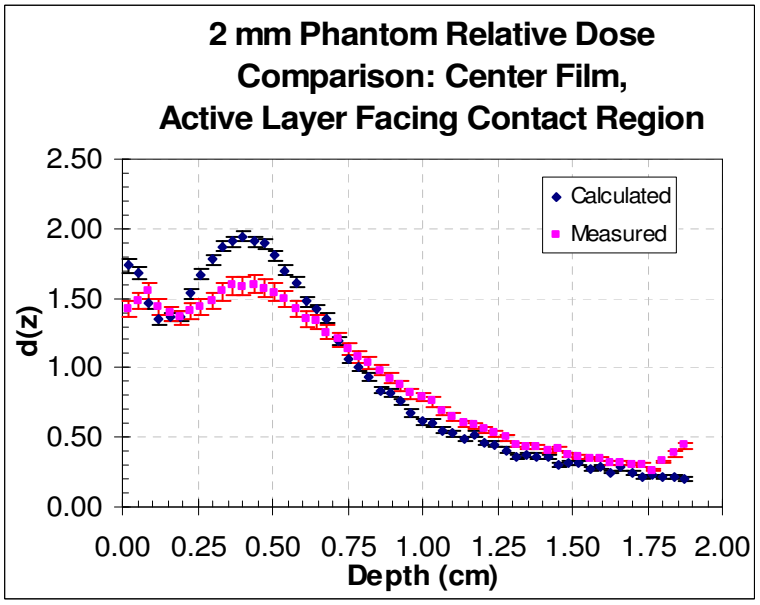

FIGURE 5.72. 2 mm phantom depth dose plot for base layer in contact with air, active layer facing styrene.

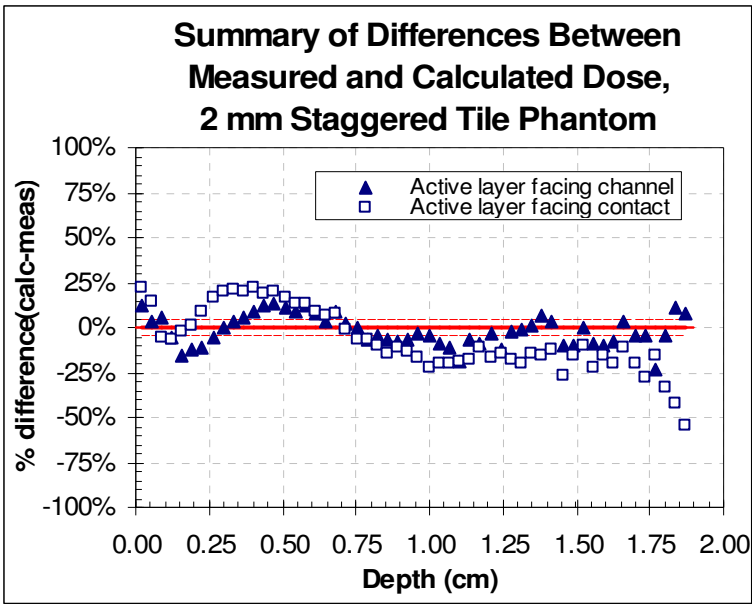

FIGURE 5.73. Summary of differences between calculated and measured values, 2 mm staggered tile phantom.

5.5 mm Staggered Tile Phantom

The 5.5 mm staggered tile phantom is shown in Figure 5.74. The voxel map was constructed with three folds, as with the normally oriented tile phantom of Figure 3.11. The midpoint of the region of interest is where the base layer of the film comes into contact with the tile (active layer facing air) and is where one comparison was made. The other point of comparison is the midpoint of where the active layer of film faces the styrene. Figures 5.75 and 5.76 show the calculated and measured isodose distributions for the staggered tile phantom.

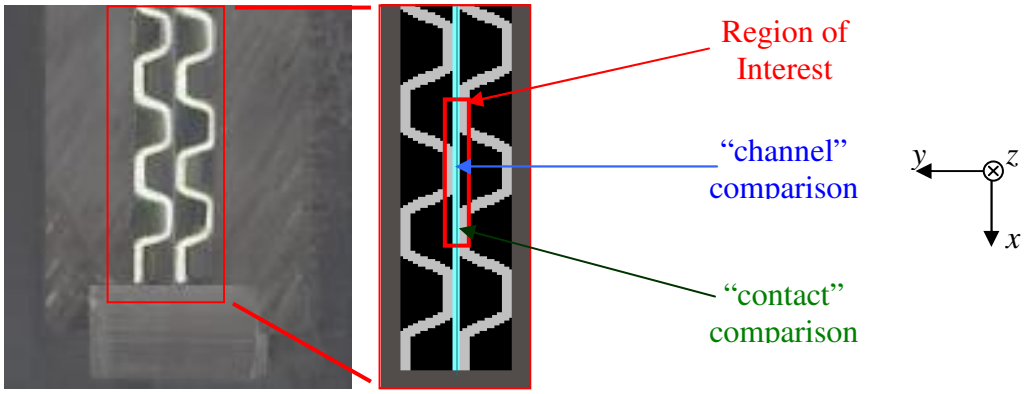

FIGURE 5.74. 5.5 mm "Staggered" tile phantom and voxel map.

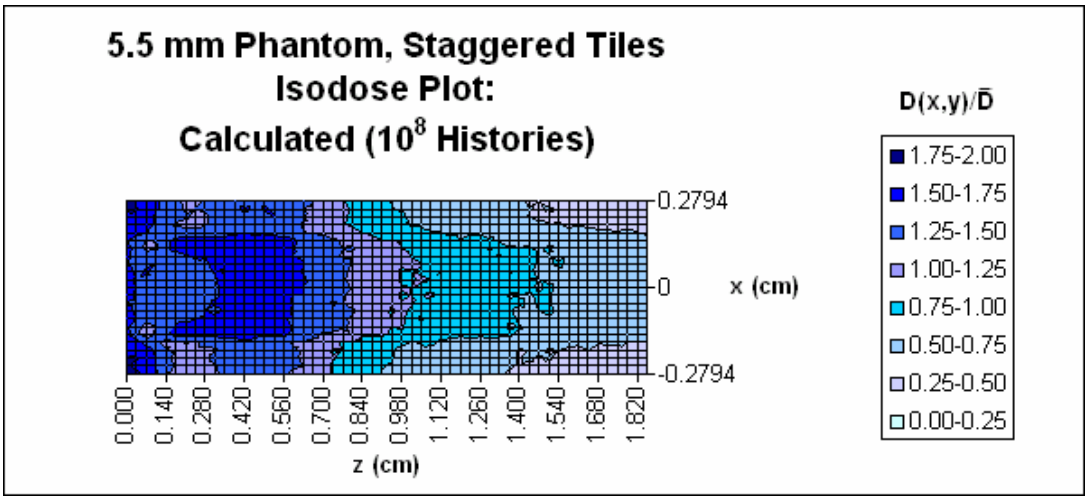

FIGURE 5.75. Calculated isodose distribution for staggered tile phantom of Figure 5.74

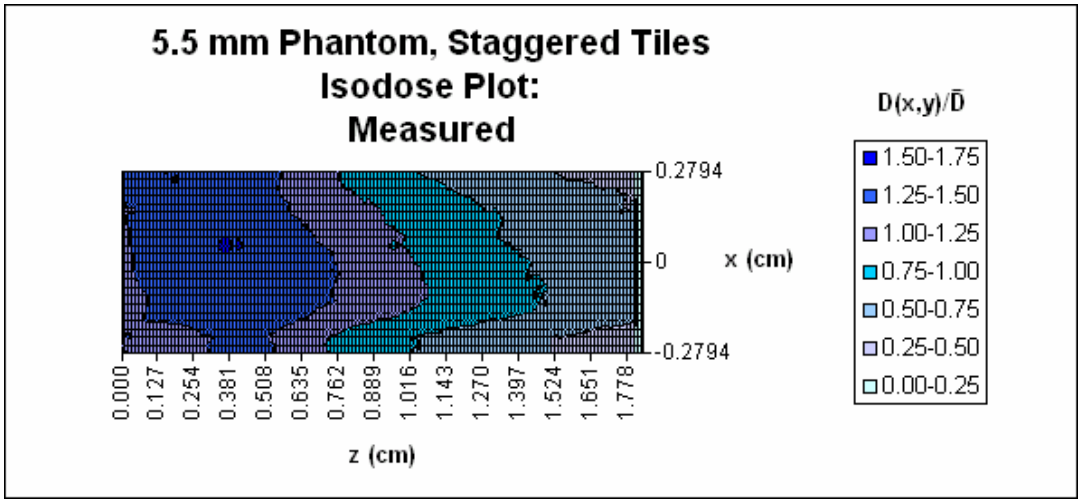

FIGURE 5.76. Measured isodose distribution for staggered tile phantom of Figure 5.74.

Figure 5.77 is the depth dose curve for the region where the base layer is facing the point of contact, and the active layer is facing the channel. As with the 2mm tile, the dose non-uniformity is the same for the normally oriented phantom ($D_{max}/\overline{D} \cong 1.50$ for both) Figure 5.78 is the depth dose curve for where the active layer is facing the point of contact, and the base layer is facing the channel. The greatest difference is in the entrance region. Figure 5.79 is a summary plot of the differences. The % difference remains within ± 25% for most of z. It exceeds it only in the entrance and exit regions.

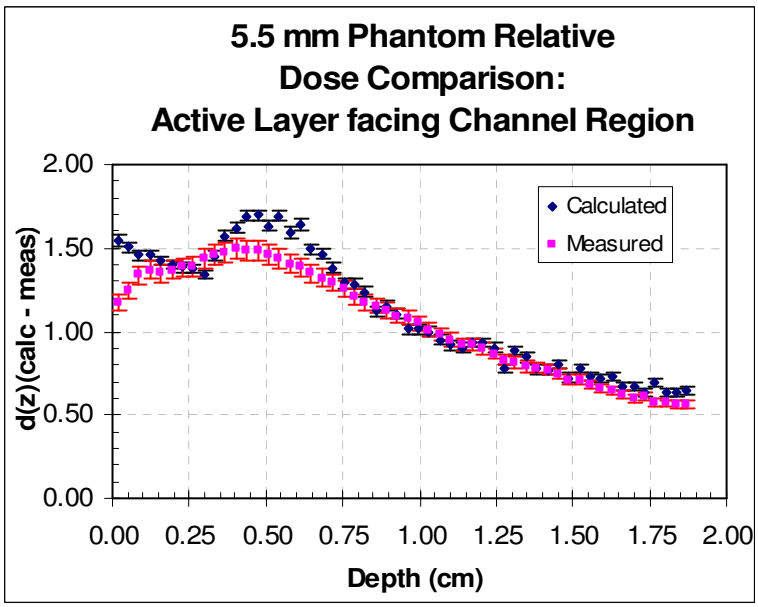

FIGURE 5.77. 5.5 mm phantom depth dose plot for base layer in contact with styrene, active layer facing air.

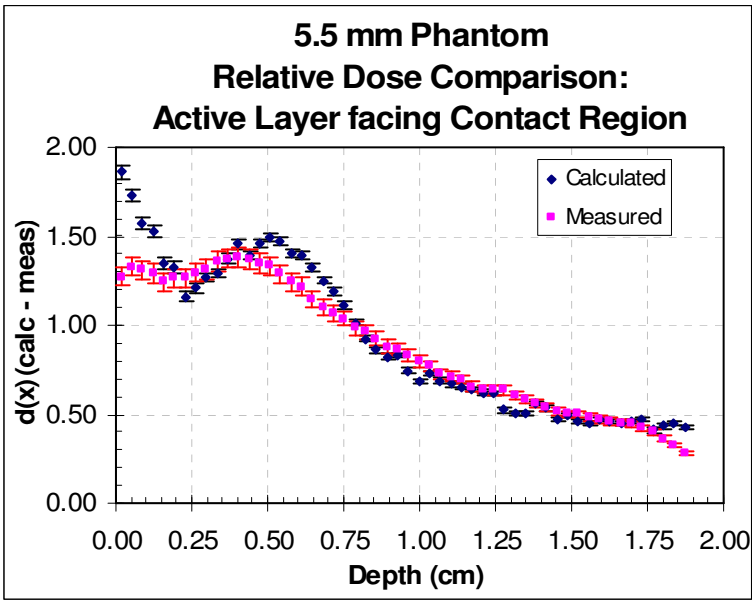

FIGURE 5.78. 5.5 mm phantom depth dose plot for base layer in contact with air, active layer facing styrene.

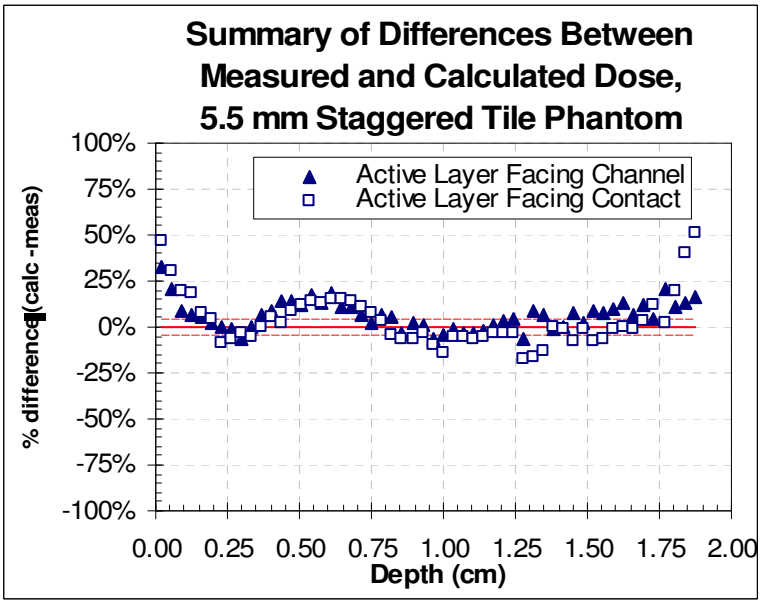

FIGURE 5.79. Summary of differences between calculated and measured values, 5.5 mm staggered tile phantom.

5.3.3 Partial Phantom

Figure 5.84 shows two partial phantom designs. 5.80.a is a 2mm corrugated tile phantom with left two tiles and film replaced with air, 5.80.b is a 2mm corrugated tile phantom with right two tiles and film replaced with air. In both cases, the active layer of the film faces to the right. So Figure 5.80.a models phantom material effects from the active side while 5.80.b models phantom effects from the base side.

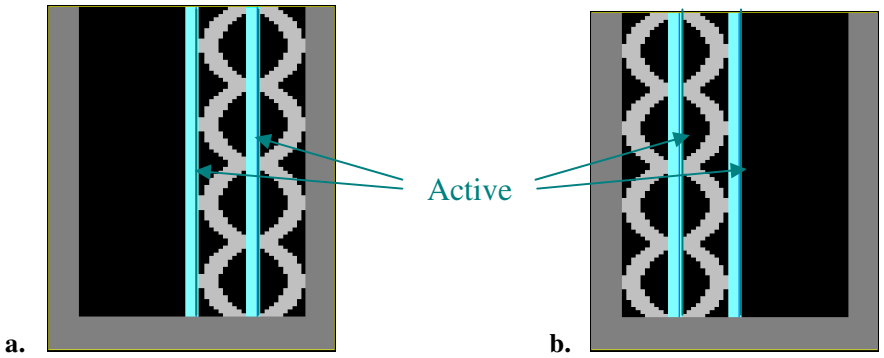

FIGURE 5.80. Partial phantom voxel map with **a.** active layer facing tiles **b.** base layer facing tiles

The partial phantom shows the relative contribution from each side of the phantom, as well as the relative shielding effect of the base layer vs. the cover layer. When the dose distribution is calculated (Figures 5.81, 5.82 and 5.83), the error bars are found to overlap between depth 0.00 and 0.50 cm. which is in agreement with section 5.2.1. This also shows that any shielding occurring due to the relatively thicker base layer of the film is minimal. The higher dose from the “base layer” phantom is due to the scattering from the air on the active side, as also discussed in Section 5.2.1.

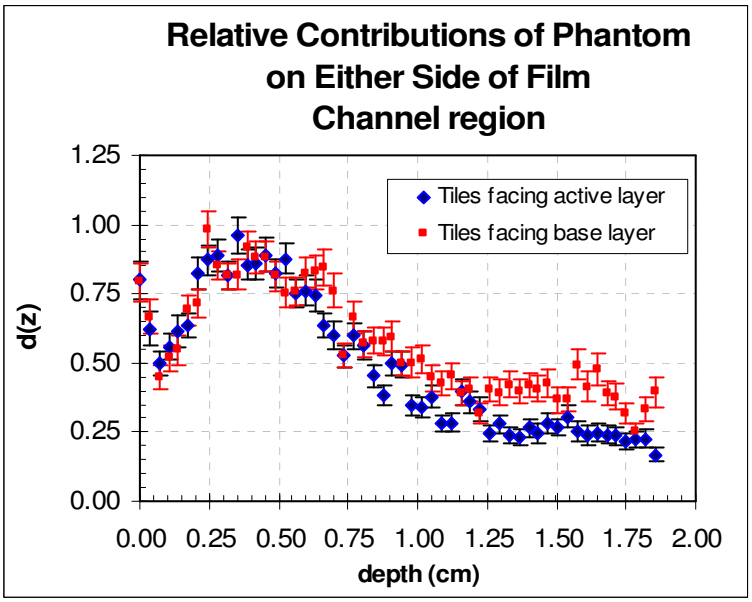

FIGURE 5.81. Relative contribution from each side of film in channel region

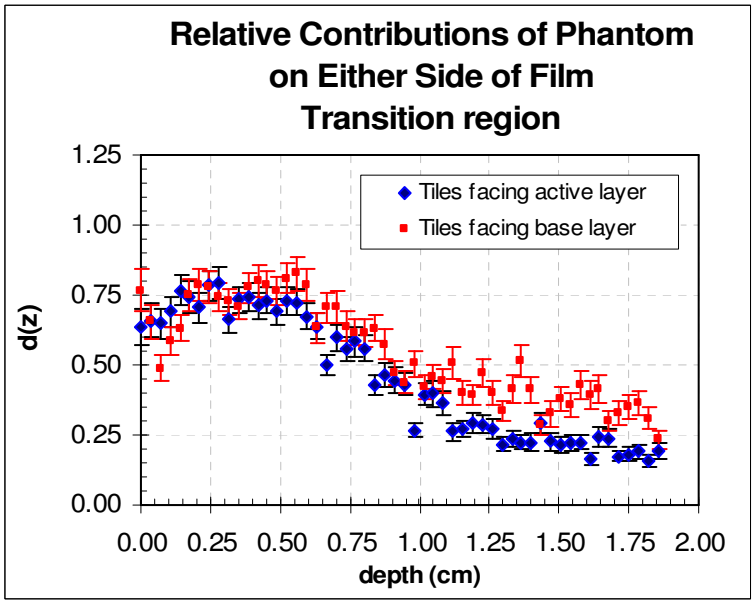

FIGURE 5.82. Relative contribution from each side of film in transition region

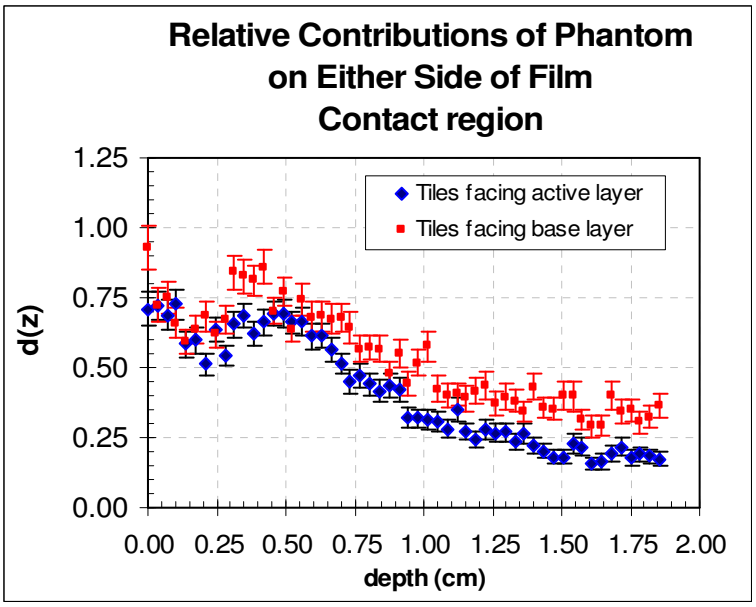

FIGURE 5.83. Relative contribution from each side of film in contact region

The measured values, however, tell a different story (Figures 5.84, 5.85 and 5.86). In all cases, the dose is greater for from the phantom facing the active layer. The distinctions between channel and contact regions are less clear. This may be due to the fact that it was not possible to assure contact between the film and tiles. Results are somewhat inconclusive in that respect.

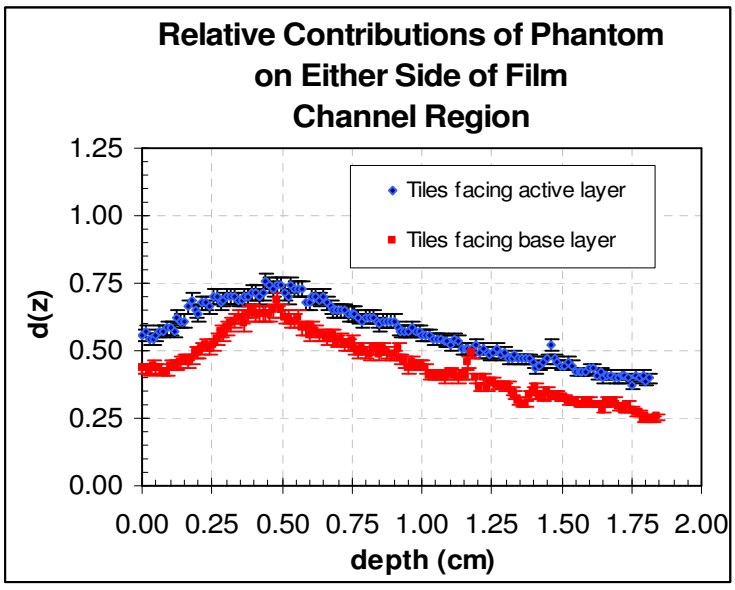

FIGURE 5.84. Relative contribution from each side of film in channel region (measured)

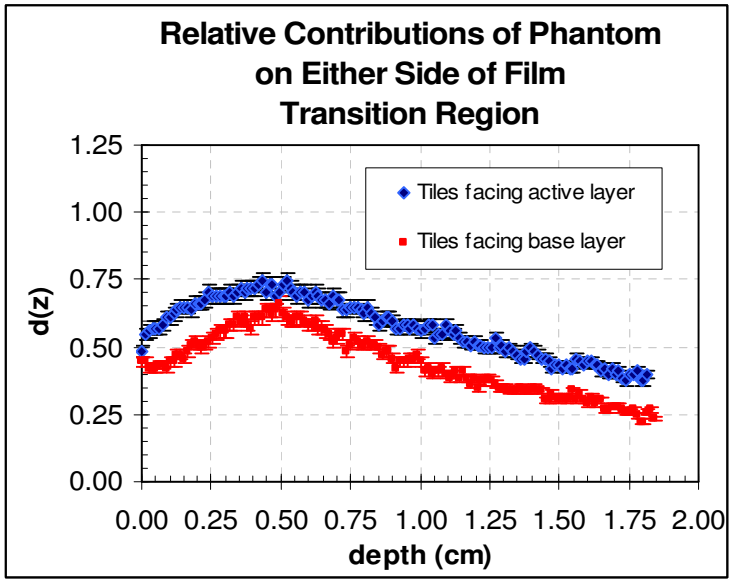

FIGURE 5.85. Relative contribution from each side of film in transition region (measured)

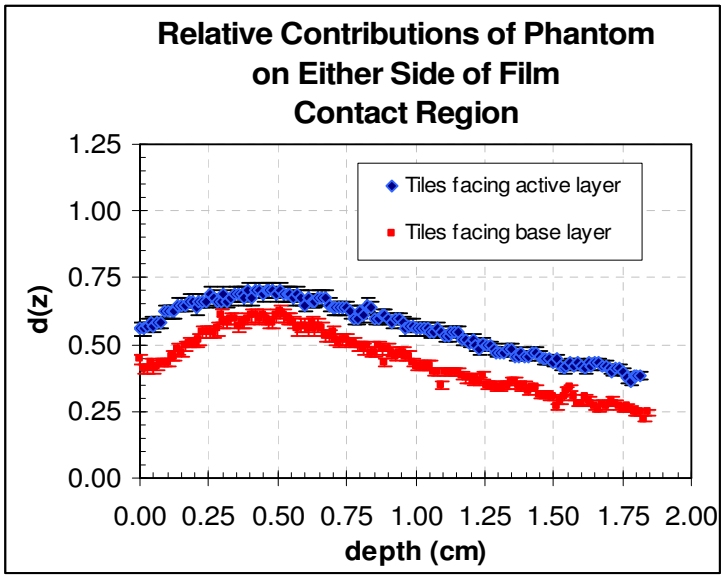

FIGURE 5.86. Relative contribution from each side of film in contact region (measured)

What *is* conclusive is that the prediction regarding behaviour due to film orientation fails here. The Monte-Carlo calculation clearly *under*estimates the effect of film orientation qualitatively as well as quantitatively.

CHAPTER VI

SUMMARY, CONCLUSIONS AND FUTURE WORK

Monte-Carlo calculations produce similar dose distributions as those produced by direct measurement. However average discrepancies are on the order of 25% over the entire phantom and can reach 75% in some specific areas (section 5.1.3). Therefore, the dose determined by using the MC results and a measurement of the electron fluence is not sufficiently accurate for determining the average absorbed dose when planning treatment of objects with layered complex shapes. These errors do not appear to be artifacts caused by the condensation of track histories, since employing more exact histories does not reduce the magnitude of error (section 5.3.2).

More serious is the issue of peak to average dose ratio. For densely packed leaves, where the air gaps are on the order of 1mm in depth, hot spots can exceed 200% of the mean dose value (section 5.4.1). For items requiring a dose uniformity of ± 10% or less, the feasibility of effective electron irradiation is cast into serious doubt, at least in the case of leafy or layered vegetables, which may suffer significant degradation (loss of quality) at doses only slightly above that required for effective pasteurization.

Monte Carlo analysis will provide a reasonable *qualitative* picture of the dose distribution, but such a picture is not sufficiently accurate in a *quantitative* sense. Caveats with respect to using current Monte Carlo methods to determine dose are as follows.

- Air gaps immediately adjacent to the plant material will produce large discrepancies between calculation and measurement. (section 5.2.1) This has

serious implications for dosimetry of thin layered objects such leafy vegetables as spinach. Smaller channels are observed to have greater discrepancy between calculation and measurement (section 5.4.1). This means that dosimetry will be less accurate for densely packed items.

- Monte-Carlo simulations do not appear to adequately model all of the scattering components in an object with a repeating structure (e.g. onion or leafy vegetable).(section 5.2.4)

- Primary differences between calculated and measured dose occur in the entrance region ($z < \frac{1}{3}R_{poly}$) along the boundary of the air gaps, with maximum percent difference reaching 75%.(section 5.2.5).

- Boundary effects produce the most error where the beam is parallel to the interface (section 5.3.1).

- Decreasing the number of interactions (through condensed track histories) did not increase the discrepancies between measurement and calculation. Conversely, increasing the number of interactions did not reduce the discrepancies between measurement and calculation. (section 5.3.2)

Possible Future Work:

- Irradiation of randomly oriented “leaves” of radiochromic film, in order to better assess dose uniformity in the case of leafy vegetables. Accurate Monte Carlo calculations do not currently appear to be feasible.

- Modeling and irradiation of phantoms with higher and lower LET radiation to determine how the number of calculation errors may relate to the LET.

REFERENCES

1 J. Han, C. Gomes, M.E. Castell-Perez, R.G. Moreira, & P. da Silva, Quality of Packaged Romaine Lettuce Hearts Exposed to Low-dose Electron Beam Irradiation. *Lebensmittel-Wissenschaft und-Technologie/Food Science and Technology*. **37(7)** 705±715 (2004).

2 J. Kim, R.G. Rivadeneira, M.E. Castell-Perez, & R.G. Moreira, Development And Validation of a Methodology For Dose Calculation In Electron Beam Irradiation Of Complex-Shaped Foods. *Journal of Food Engineering*, **74**, 359±369 (2006).

3 R. Rivadeneira, R. Moreira, J. Kim, & M.E. Castell-Perez. Dose Mapping of Complex-Shaped Foods Using Electron-Beam Accelerators. *Food Control*, **18**, 1223±1234, (2007).

4 G. Brescia, R.G. Moreira,, L. Braby, & M.E. Castell-Perez, Monte Carlo simulation and dose distribution of low energy electron irradiation of an apple. *Journal of Food Engineering,* **60(1)***,* pp. 31±39, (2003).

5 F. Attix, *Introduction to Radiological Physics and Radiation Dosimetry*. (Wiley-Interscience, New York NY, p.198, (1986).

6 F. Attix, *Introduction to Radiological Physics and Radiation Dosimetry*. (Wiley-Interscience, New York NY, pp. 167±172, (1986).

7 F. Attix, *Introduction to Radiological Physics and Radiation Dosimetry*. (Wiley-Interscience, New York NY, p. 199, (1986).

8 A. Nahum, Overview of Photon and Electron Monte Carlo Method, in *Monte Carlo Transport of Electrons and Photons* (T.M Jenkins et al. Editors), Plenum, New York NY, pp. 10±13 (1987).

9 I Kawrakow, & A Bielajew, On the Condensed History Technique for Electron Transport, *Ionizing Radiation Standards*, NRCC, Ottawa ONT, pp 3±5 (1998).

10 M. J. Berger, Monte Carlo Calculation of the Penetration and Diffusion of Fast Charged Particles, in *Methods in Computational Physics Vol 1* (B Adler, S Fernbach, M Rotenberg Editors), Academic Press Inc., Burlington, MA, pp.135±215. (1972)

11 A. F. Bielajew, Electron Step Size Artifacts and PRESTA, in *Monte Carlo Transport of Electrons and Photons* (T.M Jenkins et. al. Editor), Plenum, New York NY, pp. 113±137 (1987).

12 A. F. Bielajew, Electron Step Size Artifacts and PRESTA, in *Monte Carlo Transport of Electrons and Photons* (T.M Jenkins et. al. Editor), Plenum, New York NY, pp. 113±137 (1987)

13 ISPCorp, GAFCHROMIC® HD810 Radiochromic Dosimetry Film and D-200 Pre-Formatted Dosimeters for High Energy Photons. Configuration, Specification, and Performance Data. *product spec sheet*, International Specialty Products, Wayne NJ, http://www.ispcorp.com/products/dosimetry/content/gafchromic/, p.5. (2007)

14 ISPCorp, GAFCHROMIC® HD810 Radiochromic Dosimetry Film and D-200 Pre-Formatted Dosimeters for High Energy Photons. Configuration, Specification, and Performance Data. *product spec sheet*, International Specialty Products, Wayne NJ, http://www.ispcorp.com/products/dosimetry/content/gafchromic/, p. 7 (2007)

15 ISPCorp, GAFCHROMIC® HD810 Radiochromic Dosimetry Film and D-200 Pre-Formatted Dosimeters for High Energy Photons. Configuration, Specification, and Performance Data. *product spec sheet*, International Specialty Products, Wayne NJ, http://www.ispcorp.com/products/dosimetry/content/gafchromic/, p. 1 (2007)

16 H.Alva, H Mercado-Uribe, M Rodriguez-Villafuente, M. E. Brandan. The use of a Reflective Scanner to Study Radiochromic Film Response. *Physics in Medicine and Biology*, **47**, 2925±2933 (2002).

17 B. Walters, I Kawrakow, DOSXYZnrc User's Manual. *Ionizing Radiation Standards*, NRCC, Ottawa ONT, p 36 (2005).

18 A. F. Bielajew, Electron Step Size Artifacts and PRESTA, in *Monte Carlo Transport of Electrons and Photons* (T.M Jenkins et. al. Editor), Springer, pp. 113±137 (1999).

19 F. Attix, *Introduction to Radiological Physics and Radiation Dosimetry*. (Wiley-Interscience, New York NY, p.232, (1986).

20 F. Attix, *Introduction to Radiological Physics and Radiation Dosimetry*. (Wiley-Interscience, New York NY, p.232, (1986).

21 F. Attix, *Introduction to Radiological Physics and Radiation Dosimetry*. (Wiley-Interscience, New York NY, p.232, (1986).

22 F. Attix, *Introduction to Radiological Physics and Radiation Dosimetry*. (Wiley-Interscience, New York NY, p.233, (1986).

23 A. E. Nahum, Simulation of Dosimeter Response and Interface effects, in *Monte Carlo Transport of Electrons and Photons* (T.M Jenkins et. al. Editor), Plenum, New York NY, pp. 529±530 (1987).

24 A. F. Bielajew, Electron Step Size Artifacts and PRESTA, in *Monte Carlo Transport of Electrons and Photons* (T.M Jenkins et. al. Editor), Plenum, New York NY, pp. 113±137 (1987).

25 ESTAR computational data, obtained from National Institute for Standards and Technology (NIST) WWW site, http://physics.nist.gov/PhysRefData/Star/Text/ESTAR.html, Accessed and retrieved circa May 2006.

26 ESTAR computational data, obtained from National Institute for Standards and Technology (NIST) WWW site, http://physics.nist.gov/PhysRefData/Star/Text/ESTAR.html, Accessed and retrieved circa May 2006.

APPENDIX A

CALIBRATION OF DOSIMETRY MEDIA

In order to calibrate the Radiochromic film, we must know the dose being delivered by the electron accelerator. Beam output is monitored by a transmission ion chamber (TIC), which is located at the beamline exit (Figure A.1).

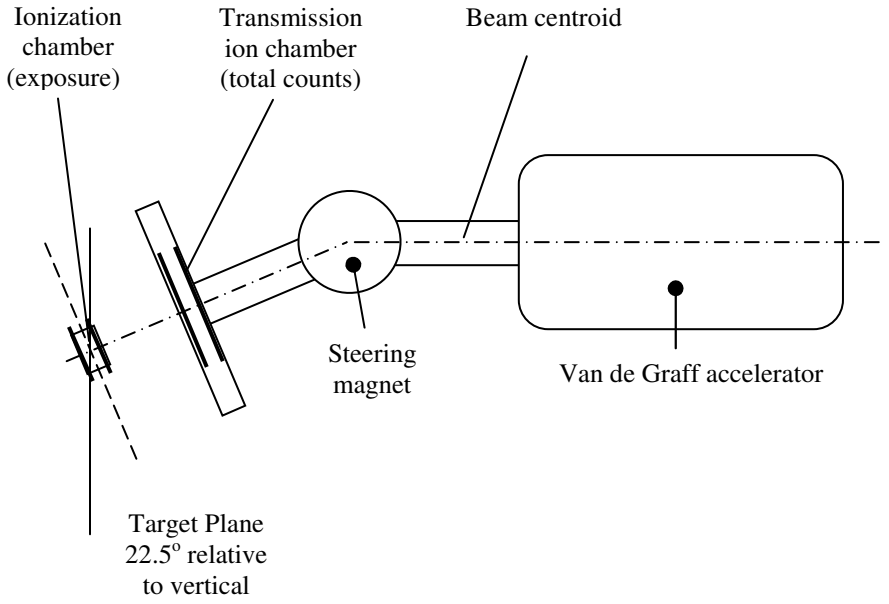

FIGURE A.1. 10 MeV Electron beam configuration for calibration of Radiochromic film.

TABLE A.1
Calibration of Transmission Ion Chamber (TIC)

	Target Plane	
TIC Value (counts)	exposure (R)	Dose (Gy)
0	0	0.00
2435	529	4.64
7566	1761	15.44
5282	1193	10.46
9981	2395	21.00
10430	2517	22.07
16400	4251	37.28

To calibrate the TIC, a small ionization chamber is placed in the target plane. By making several runs with varying exposure times (Table A.1), the exposure in Roentgens is determined as a function of TIC charge (Figure A.2). The exposure in R is then converted to Dose in Grays (Gy).

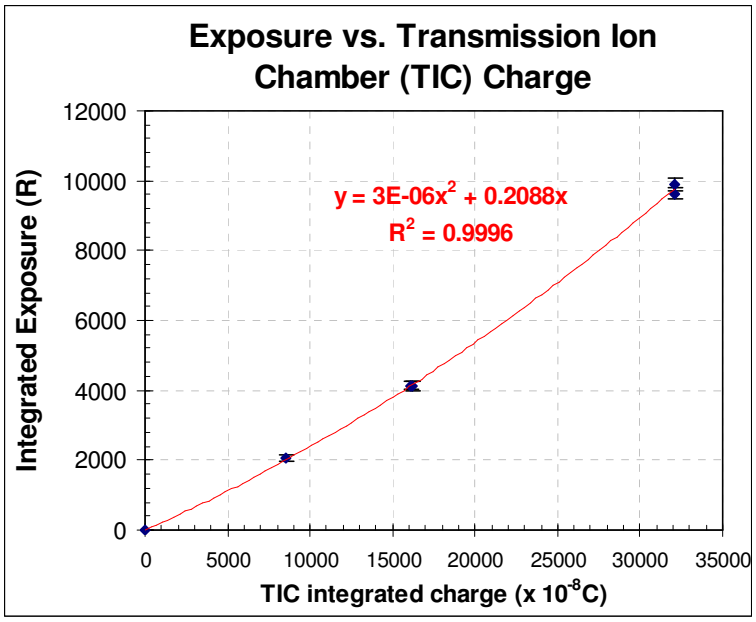

FIGURE A.2. Determining exposure a function of TIC charge

When the radiochromic film is exposed to ionizing radiation, it loses its transparency in direct proportion to the absorbed dose. The reduction in transparency is referred to as optical density and is quantified as:

$$\text{Optical Density} = \text{O.D.} = -\log_{10} T \tag{A.1}$$

where T is the *transmittivity*, or ratio between transmitted intensity to incident intensity:

$$T = I_{out}/I_{in} \tag{A.2}$$

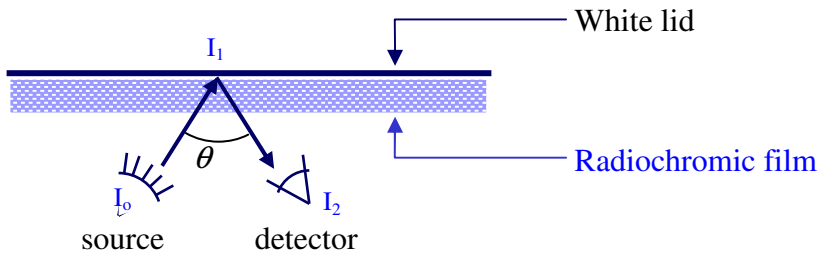

FIGURE A3. Reading of Radiochromic film via flatbed scanner

The film is read via flatbed scanner (Figure A.2) where the light from the scanner element is reflected from the white cover passed through the film before reaching the detector. Since the light passes through the film twice between the light source and detector, the transmittivity is expressed as:

$$I_1/I_o \times I_2/I_1 = I_2/I_o = T_1 \times T_2 \qquad \text{(A.3)}$$

$\theta \approx 0$, so $T_1 \approx T_2$, and $T_1 \times T_2 = T^2$. Substituting and rearranging yields:

$$T = (I_2/I_o)^{1/2} \qquad \text{(A.4)}$$

Taking the negative log of the transmittivity yields the optical density:

$$\text{O. D.} = -\log_{10}(I_2/I_1)^{1/2} \qquad \text{(A.5)}$$

In 24-bit mode, the red value is 255 for unfiltered white light. Letting I represent the observed intensity I_2 we now have the formula for optical density:

$$\text{O. D.} = -\log_{10}(I/255)^{1/2} \qquad \text{(A.6)}$$

or:

$$\text{O. D.} = \log_{10}(255/I)^{1/2} \qquad \text{(A.7)}$$

The Radiochromic film was calibrated by exposing the film to known doses, measuring the intensity and converting to optical density. The O.D. was plotted as a function of dose (Table A.2) and a linear fit was applied (Figure A.4).

Table A.2.
Calibration of radiochromic film

	Film response			
Dose (Gy)	Intensity Value (red light)	Std Dev.	OD	σ
0.00	243.61	1.65	0.00992	0.00147
4.64	232.09	1.09	0.02044	0.00102
15.44	212.59	1.96	0.03950	0.00199
10.46	219.89	1.24	0.03217	0.00122
21.00	201.49	1.79	0.05114	0.00192
22.07	200.78	1.80	0.05191	0.00194
37.28	177.37	2.93	0.07883	0.00356

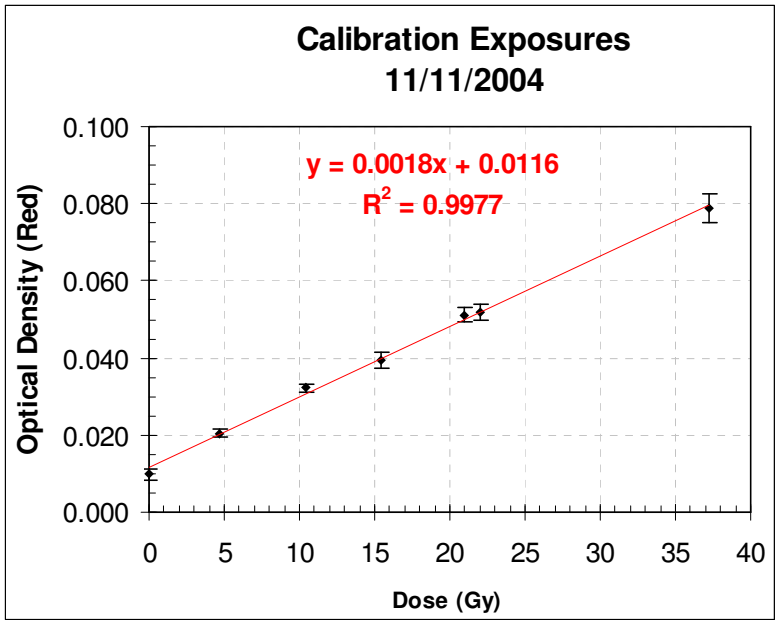

FIGURE A.4. Plot of OD vs. Dose

The least squares method provided a good fit with R^2 very close to unity. With x = Dose and y = OD, the equation in figure A.4 becomes:

$$OD = 0.0018\ Gy^{-1} * D + 0.0116 \qquad (A.8)$$

Taking the inverse of this equation yields the expression for dose as a function of O.D.:

$$\text{Dose} = (\text{OD} - 0.0116)/0.0018 \text{ Gy}^{-1} \quad \text{(A.9)}$$

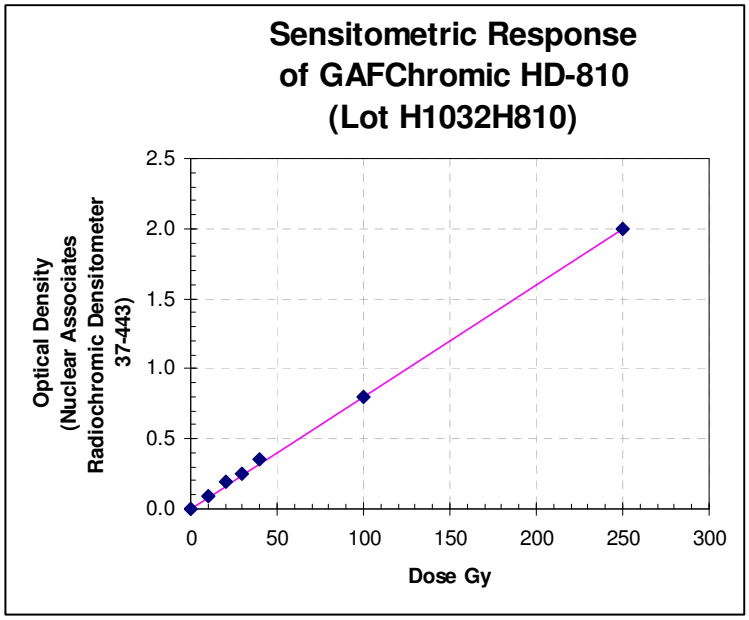

FIGURE A.5: OD vs. Dose as provided by manufacturer spec. (*1*)

1 ISPCorp, GAFCHROMIC® HD810 Radiochromic Dosimetry Film and D-200 Pre-Formatted Dosimeters for High Energy Photons. Configuration, Specification, and Performance Data. *product spec sheet* P.3.

APPENDIX B

REPEATABLE GEOMETRY SETUP FOR TARGET IRRADIATION

To produce accurate measurement of target doses, one must have a repeatable geometry of target irradiation. The target holder was cut from 0.25" (0.64 cm) acrylic, assembled to form a pocket 0.75" × 0.75" × 0.21" (1.91 cm × 1.91 cm × 0.53 cm). The target holder is mounted on a base, with the front face at an angle of 22.5° to vertical (Figure B.1).

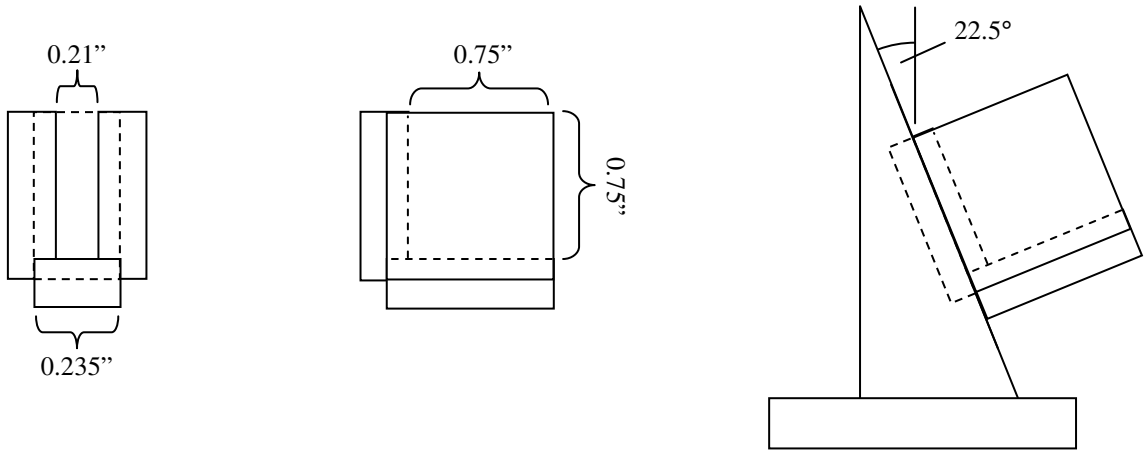

FIGURE B.1. Target holder with dimensions.

For each shot, the target was assembled and placed into the target from the front, so as not to disturb the alignment of the tiles (Figure B.2). The fully assembled targets are shown in Figure B.3

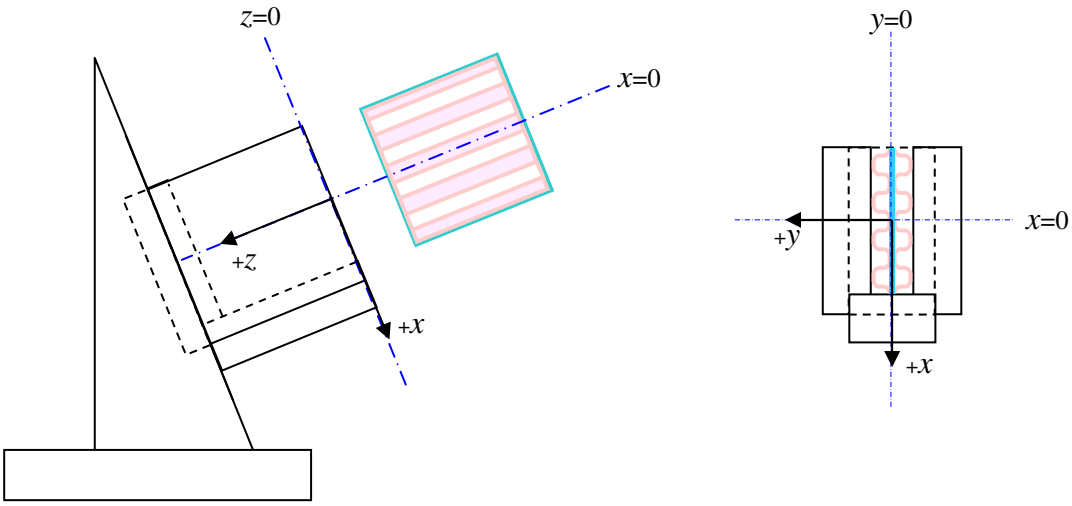

FIGURE B.2. Target holder showing placement of target and co-ordinate system.

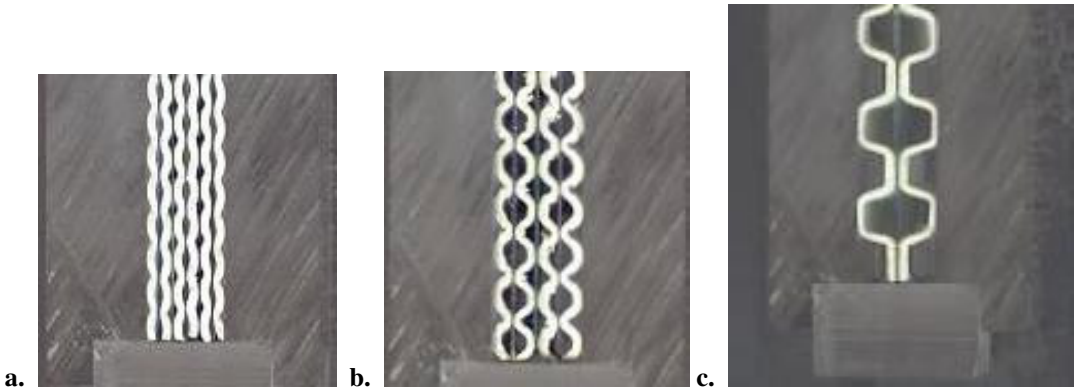

FIGURE B.3. Assembled targets, **a.** 1mm phantom **b.** 2mm phantom **c.** 5.5mm phantom

The assembled target and holder were placed on a horizontal platform such that the center of the phantom coincided with the beam axis (Figure B-4). The target holder was held in position on the platform by a u-shaped bracket (Figure B-5).

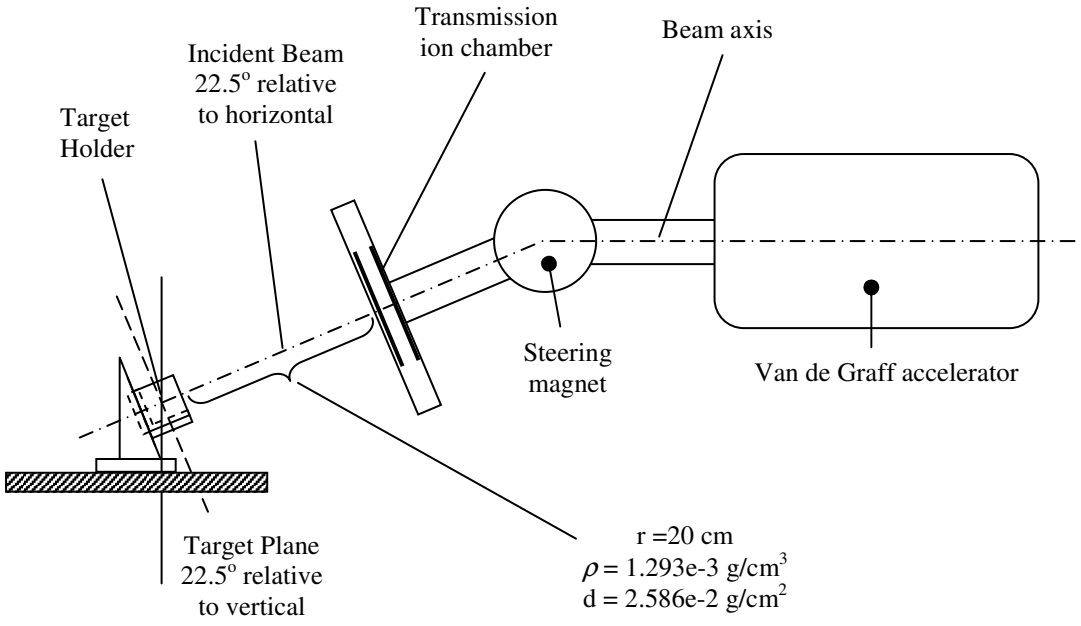

FIGURE B.4. Electron beam configuration for irradiation of phantom.

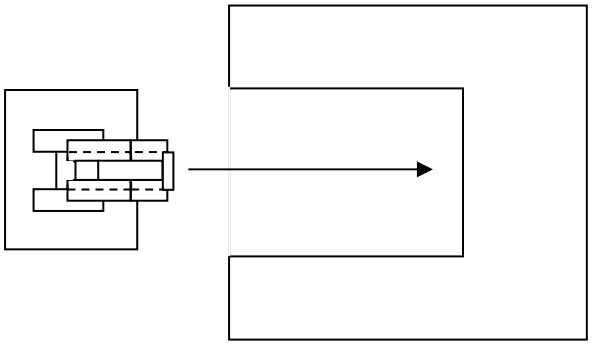

FIGURE B.5. Detail of target holder stop.

APPENDIX C

VARIATION OF MONTE-CARLO PARAMETERS FOR 5.5 MM PHANTOM

SMAX

Figures C.1, C.2 and C.3 show the effects of SMAX on the dose distributions in the channel, transition, and contact regions of the 5.5 mm phantom, respectively. While there are slight differences in the calculated values for SMAX ranging from 0.05 to 5 cm, none are statistically significant.

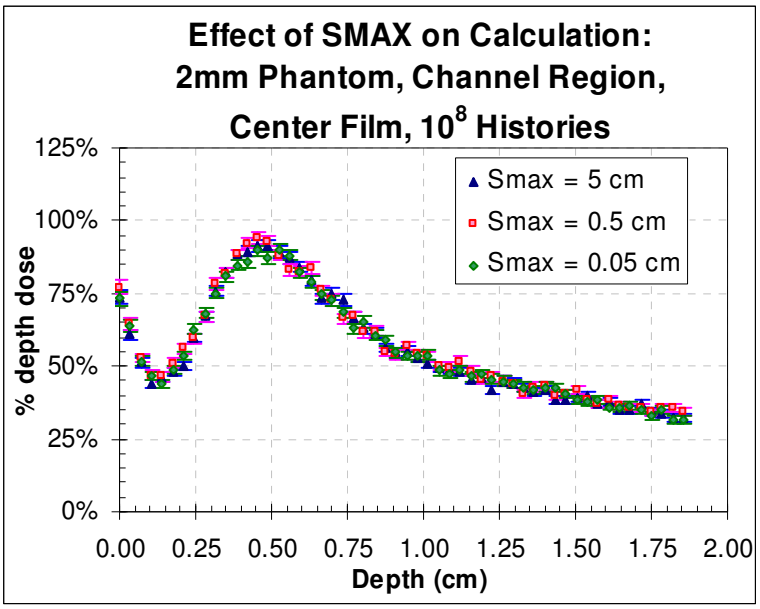

FIGURE C.1. Effect of SMAX on dose in channel region of 5.5 mm phantom.

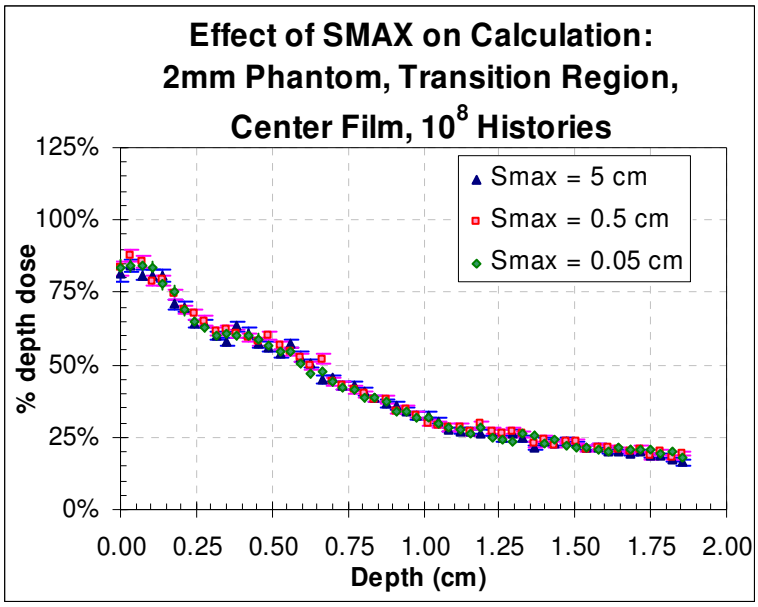

FIGURE C.2. Effect of SMAX on dose in transition region of 5.5 mm phantom.

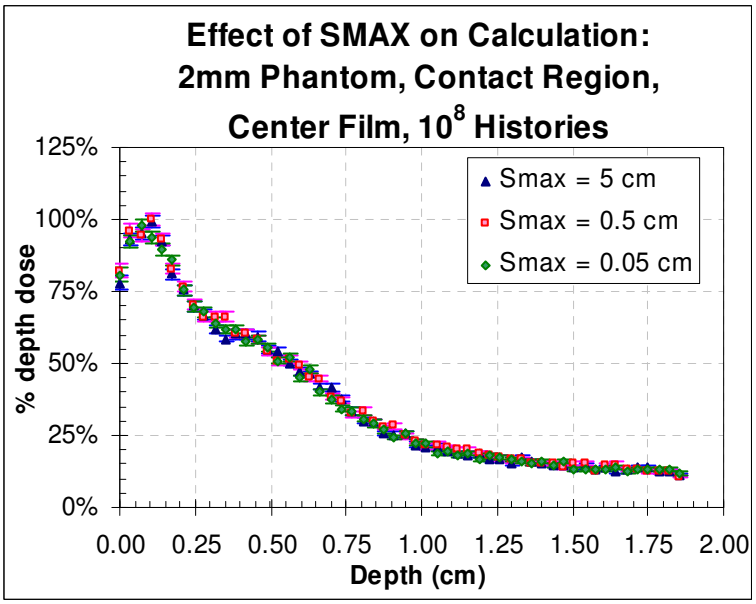

FIGURE C.3. Effect of SMAX on dose in contact region of 5.5 mm phantom.

ESTEPE

For the initial calculations, ESTEPE was set at 0.1. This means that the maximum fractional energy loss per step was 10% of the incident value. The default value for calculations is 0.25. Figures C.4, C.5 and C.6 show depth dose plots for ESTEPE values of 0.1, 0.25, and 0.5, for each of the three regions of interesting the 5.5 mm pitch phantom. While there was some observable difference between the three ESTEPE values, it was small and amounted only to statistical noise.

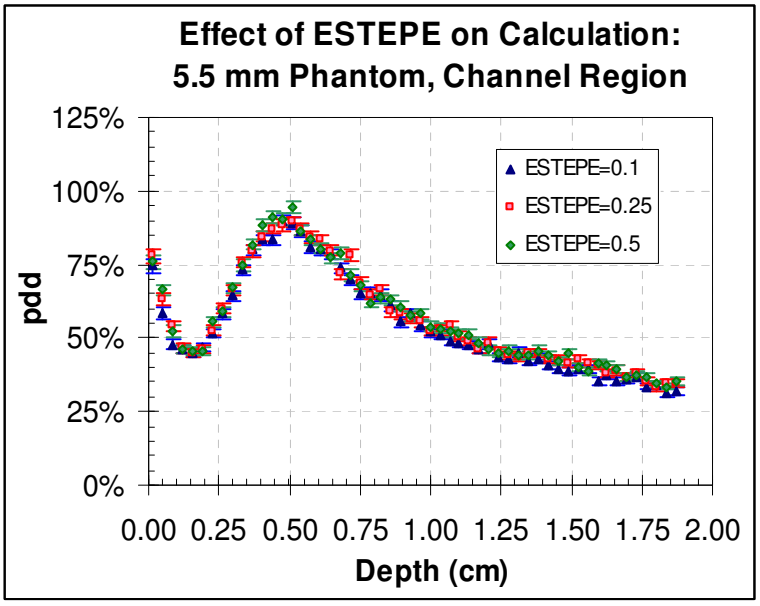

FIGURE C.4. Effect of ESTEPE on dose in channel region of 5.5 mm phantom.

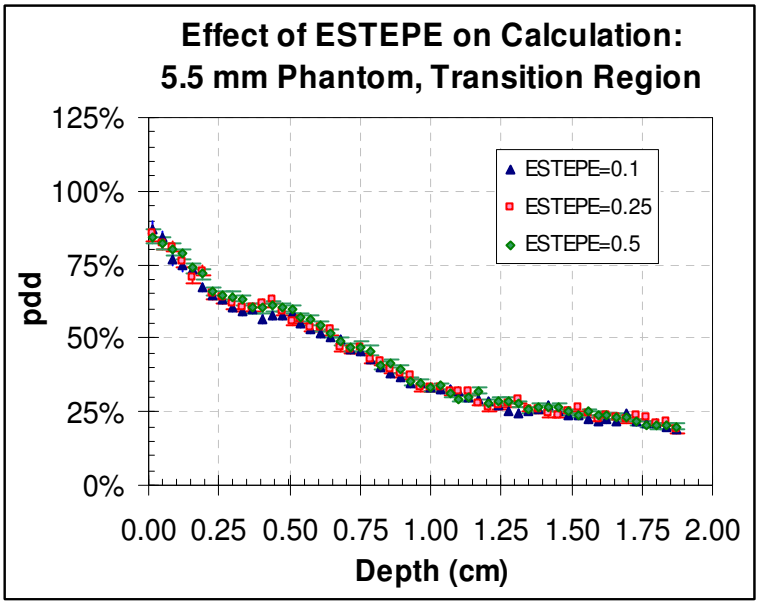

FIGURE C.5. Effect of ESTEPE on dose in transition region of 5.5 mm phantom

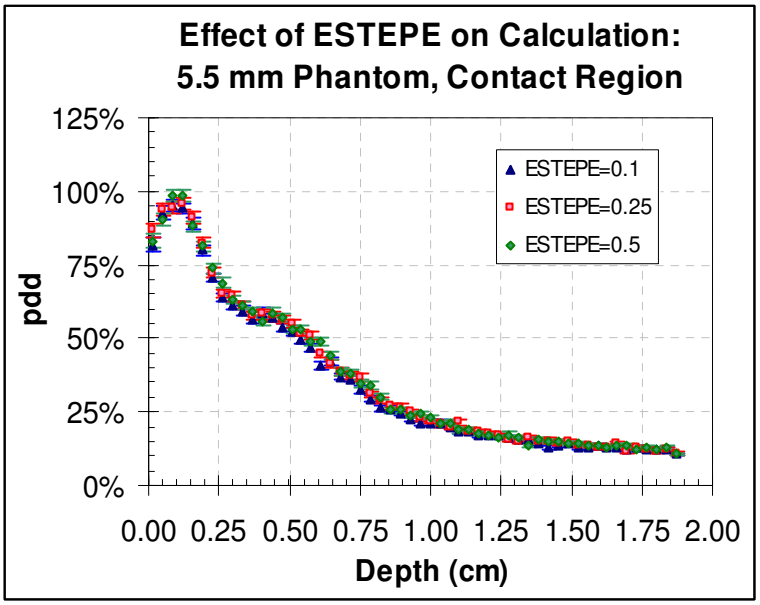

FIGURE C.6. Effect of ESTEPE on dose in contact region of 5.5 mm phantom

ECUT

Figures C.7, C.8, and C.9 show the depth dose curves for the channel, transition and contact regions for the 2 mm pitch phantom. Varying ECUT from 0.01 to 0.67 MeV has no effect whatsoever on the calculation.

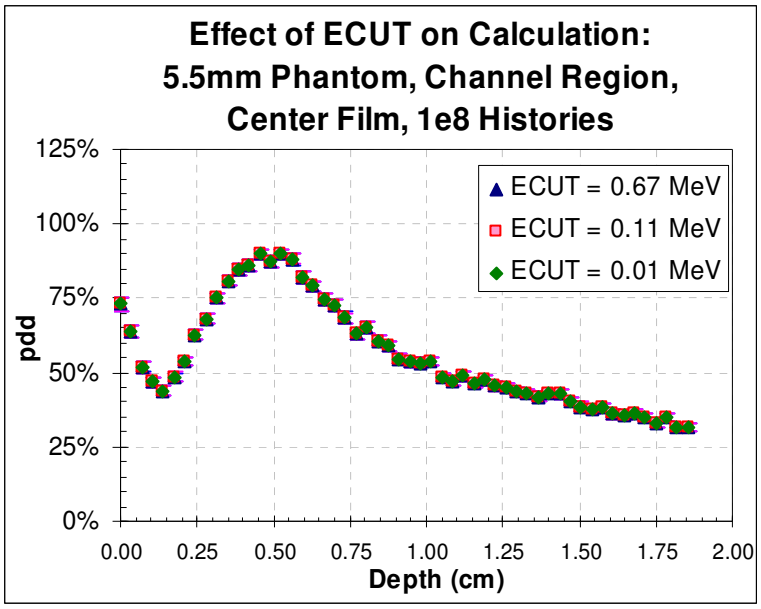

FIGURE C.7. Effect of ECUT on dose in channel region of 5.5 mm phantom

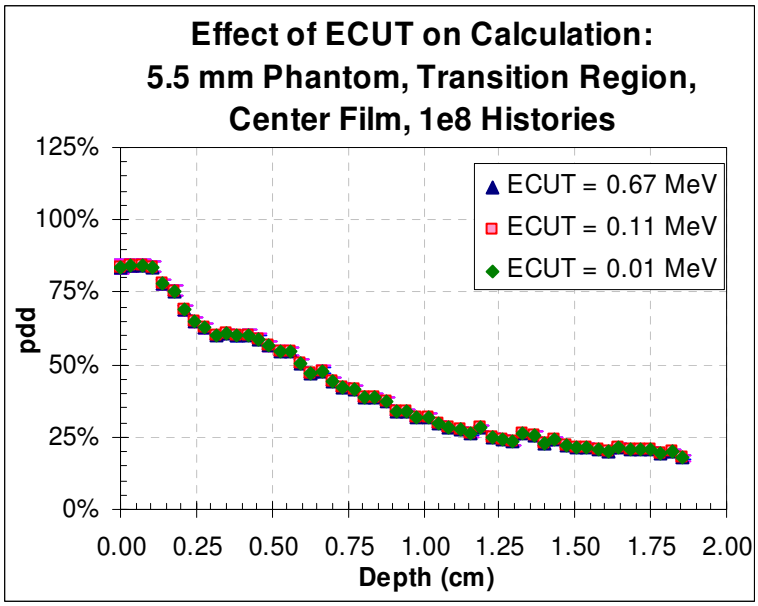

FIGURE C.8. Effect of ECUT on dose in transition region of 5.5 mm phantom

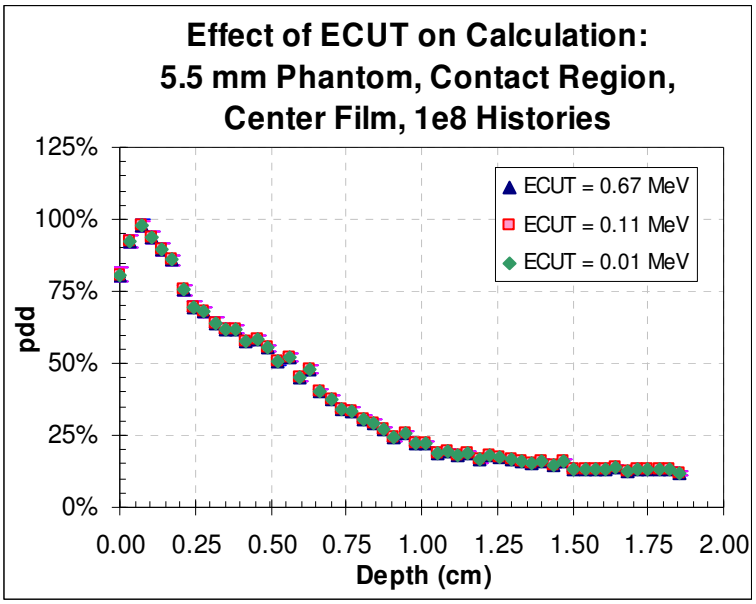

FIGURE C.9. Effect of ECUT on dose in contact region of 5.5 mm phantom

VITA

Teresa Elizabeth Tutt

Education:

B.S., Rensselaer Polytechnic Institute 1994

M.S., Massachusetts Institute of Technology 2000

Ph.D.; Texas A&M University 2007

Permanent contact address:

Department of Nuclear Engineering
Texas A&M University
3133 TAMU
College Station, TX 77843-3133